CFD Study of Dense Effluent Discharges in Deep and Shallow Waters

by

Hossein Kheirkhah Gildeh

Thesis submitted to the University of Ottawa

In partial fulfillment of the requirements

for the Ph.D. degree in Civil Engineering

Department of Civil Engineering

Faculty of Engineering

University of Ottawa

Thesis Committee in the COVID-19 Pandemic World! From top and left to right: Prof. Ousmane Seidou (University of Ottawa), Hossein Kheirkhah Gildeh, Prof. Hamidreza Shirkhani (University of Ottawa), Prof. Jules-Ange Infante (University of Ottawa), Prof. Majid Mohammadian (University of Ottawa, Thesis Advisor), Prof. Bruce MacVicar (University of Waterloo), Prof. Ioan Nistor (University of Ottawa, Thesis Advisor), Prof. Iluju Kiringa (University of Ottawa, Defense Chairperson).

Abstract

Liquid wastes discharged from industrial outfalls have been researched for many years in the past. Majority of past studies, initiated in 1960s, were experimental studies mainly focused on basics of discharges such as key geometrical properties. Eventually, more robust experimental studies were performed to measure the mixing properties of effluent discharges with various jet configurations and ambient water conditions. Discharges could be as a means of submerged diffusers or surface channels and receiving water could vary from a homogenous calm ambient to a very complex stratified turbulent cross flow ambient. Depending on the bathymetric and economic situation around an outfall project, submerged discharges are preferred designs for most of ocean outfalls. It is the reason that majority of past studies have evaluated the mixing characteristics of submerged jets. Since early 1990s, the numerical modelling has emerged to support complex fluid mechanic problems. Later in 1990s and early in 2000s, the use of computational fluid dynamic (CFD) tools emerged in predicting the jet properties for the effluent discharges. Since then different numerical models have been developed for different applications. Similar to experimental studies, most of numerical studies have been focused on the submerged dense jet discharges. The current study intends to stay focused on the numerical modelling of such jets too; however, to cover the gaps in the literature. To achieve this, a thorough literature review was performed on the past CFD studies of over past 20 years to better understand what was done and what the gaps are. The results of this thorough review revealed that although there has been a great progress in the CFD studies in the field of effluent discharges, there are some applications that have not been investigated before, yet. It was found that there are some discharge inclinations that were not studied numerically before. Four discharge angles of 60°,75°, 80° and 85° were selected in this study, as previous studies mostly focused on 30° and 45°. The higher inclinations are more suitable for deep water outfalls where terminal rise height of the jet does not attach to the ambient water surface. The numerical model OpenFOAM was used in this study which is based on the Finite Volume Method (FVM) applying LRR turbulence model closure. LRR turbulence models was proved to be a capable choice for effluent discharge modelling. The second gap identified in the comprehensive literature review completed was the submerged dense effluent discharge into shallow water with surface attachment (for both

inclined and vertical discharges). There was no previous numerical study of such jets identified. Three different regimes were identified: full submergence, plume contact and centerline impingement regimes (i.e. FSR, PCR and CIR). Key geometrical and dilution properties of these jets at surface contact (Xs, Ss) and return point (Xr, Sr) were extracted numerically and compared to those available from experiments. Two discharge angles (30° and 45°) were investigated based on the available experimental data. Five Reynolds-averaged Navier-Stokes (RANS) turbulence models were examined in this study: realizable k-ε and k-ω SST models (known as two-equation turbulence models), v2f (four equations to model anisotropic behavior) and LRR and SSG turbulence models (known as Reynolds stress models - six equations to model anisotropic behavior). Vertical dense effluent discharges are popular in the design of outfall systems. Vertical jets provide the opportunity to be efficient for a range of ambient currents, where the jet will be pushed away not to fall on itself. This research work investigates worst case scenario in terms of mixing and dilution of such jets: vertical dense effluent discharges with no ambient current and in shallow water where jet impacts the surface. This scenario provides a conservative design criteria for such outfall systems. The numerical modelling of such jets has not been studied before and this research work provides novel, though preliminary, insights in simulations of vertical dense effluent discharges in shallow waters. Turbulent vertical discharges with Froude numbers ranging from 9 to 24 were simulated using a Reynolds stress model (RSM), based on the results from inclined dense discharges to characterize the geometrical (i.e., maximum discharge rise Z_m and lateral spread R_{sp}) and dilution μ_{min} properties of such jets. Three flow regimes were reproduced numerically, based on the experimental data: deep, intermediate and impinging flow regimes.

To the memory of my beloved father.

به یاد پدر عزیزم.

Acknowledgements

I owe this to my life-lasting coaches, my parents, Sakineh and Mohammadreza. I do not know how to thank you!

I am very lucky in life to have my beloved wife Hengameh by my side. Her support and encouragement to pursue my studies were enormous. Thank you for your patience and encouraging me to continuously better myself.

I am grateful to my siblings for their moral and emotional supports in my life.

This work would have not been possible without guidance and support from my amazing advisors, Prof. Majid Mohammadian and Prof. Ioan Nistor. Thank you very much for your continuous supports and providing me with many opportunities.

I also like to thank my thesis evaluation committee: Prof. Seidou, Prof. Infante, Prof. Shirkhani and Prof. MacVicar for their insightful comments.

I would like to thank all my colleagues at Golder Associates Ltd., Barr Engineering Co., and UOttawa for many things that I have learnt from them in past several years.

Special thanks to my friend, mentor and coach Mr. Gaven Tang from Golder Associates Ltd. whom I learnt a lot from and went on amazing camping trips with!

Table of Contents

List of Figures

List of Tables

List of Abbreviations

2D: Two-dimensional

3D: Three-dimensional

ADV: Acoustic Doppler Velocimeter

CFL: Courant-Friedrichs-Lewy

CIR: Centerline Impingement Regime

CFD: Computational Fluid Dynamics

CPU: Central Processing Unit

DIC: Diagonal Incomplete Cholesky

DILU: Diagonal Incomplete LU

DKSM: Dynamic Kinetic Energy Sub-grid-scale Model

DNS: Direct Numerical Simulation

DSLM: Dynamic Smagorinsky-Lily Model

EU: European Union

FSR: Full Submergence Regime

FVM: Finite Volume Methods

GA: Genetic Algorithm

GCI: Grid Convergence Index

GDH: Gradient Diffusion Hypothesis

GGDH: General Gradient Diffusion Hypothesis

GPU: Graphical Processing Unit

IMZ: Initial Mixing Zone

LES: Large Eddy Simulations

LEVM: Linear Eddy Viscosity Model

LIF: Laser-Induced Fluorescence

LNG: Liquefied Natural Gas

LRR: Launder-Reece-Rodi

ME: Mean Error

MSF: Multi-Stage Flash

OpenFOAM: Open-source Field Operation And Manipulation

PBiCG: Preconditioned Biconjugate Gradient

PCG: Preconditional Conjugate Gradient

PCR: Plume Contact Regime

PDE: Partial Differential Equation

PISO: Pressure-Implicit with Splitting of Operators

PIV: Particle Image Velocimetry

PLIF: Planar Laser Induced Fluorescent

RANS: Reynolds-averaged Navier-Stokes

RMSE: Root Mean Square Error

RO: Reverse Osmosis

RSM: Reynolds Stress Model

RSTM: Reynolds Stress Turbulence Model

SGDH: Standard Boussinesq Gradient Diffusion Hypothesis

SGS: Smagorinsky Sub-grid Scale

SSG: Speziale, Sarkar and Gatski

TVH: Turbulent Viscosity Hypothesis

US-EPA: United States Environmental Protection Agency

VOF: Volume of Fluid

V-LES: Very-Large Eddy Simulation

List of Symbols

b: velocity 1/e width

b_c: nominal width of vertical mean concentration distribution where $C_M = e^{-1}C_{Mc}$

B_{gc}: Jet concentration 1/e width

B_0: Jet buoyancy flux

C: concentration relative to ambient concentration

C_a: Ambient water concentration

C_m: Jet centerline maximum concentration

C_{Mc}: mean concentration at jet axis

C_{RMS}: RMS value of concentration fluctuations

C_0: Jet exit concentration

D or d: Nozzle diameter or diffusion coefficient

F_{rd}: Densimetric Froude number

F_0: densimetric Froude number at source

G: Swirl number

g: Gravitational acceleration

g'_0: Reduced gravitational acceleration

H: water depth above nozzle level

H_a: Ambient water depth

k: Turbulent kinetic energy

k_{eff}: Heat transfer coefficient

L: Cling length

L_M: Jet momentum-length scale

L_Q: Jet source-length scale

Lv: distance along the jet centerline

L_s: length scale to normalize jet height [m]

M_0: Jet kinematic momentum flux

P: Fluid pressure

Pr: Prandtl number

Pr_t: Turbulent Prandtl number

q_j: turbulent scalar flux

Q_0: Jet discharge volume flux

r: radial distance

Re: Reynolds number

Ri: Richardson number

R_{sp}: jet lateral spread rate

S: Dilution

s: Jet stream-wise distance

S_i: centreline (minimum) dilution at region where the jet returns at source elevation

S_m: Jet centerline peak dilution

S_r: Jet dilution at return point

S_s: minimum dilution at the water surface

S_t: centreline (minimum) dilution at terminal height

t: Time

T: Jet temperature at any location

T_a: Ambient water temperature

T_0: Jet exit temperature

U_m: Jet velocity component in the x-direction

U_{m0}: Jet centerline maximum velocity

U_0: Jet exit velocity

u: Mean velocity component in the x-direction

u_o: Inlet velocities of the offset jet

u_w: Inlet velocities of the wall jet

v: Mean velocity component in the y-direction

V_m: maximum vertical velocity at a cross section

V_r: Velocity ratio

w: Mean velocity component in the z-direction

X: horizontal axis of the coordinate system

x_i: Horizontal location of impact

x_m: Jet centerline peak horizontal location

x_r: Jet return point

X_y: horizontal distance from jet exit to location of terminal rise height

Y: vertical axis of coordinate system

Y_f: final terminal height of rise (refers to outer jet boundary)

Y_i: initial terminal height of rise

y_m: jet centerline peak vertical location

$y_{m/2}$: Jet velocity-half-height (the height of $U_m=U_{m0}/2$)

y_t: Terminal rise height

Z_m = discharge maximum rise [m]

α: Jet entrainment constant

Γ: scalar diffusivity

Γ_t: turbulent dispersity

δ_{ij}: Kronecker delta

ε: Turbulent dissipation rate

θ: Angle of discharge

μ: fluid viscosity

μ_t: Turbulent viscosity

ρa: Ambient water density

$\rho 0$: Jet exit density

$\Delta\varrho$ = density difference

τ_{ij}: Reynolds stresses

υ: Kinematic viscosity

υ_t: Turbulent kinematic viscosity

υ_{eff}: Effective kinematic viscosity

1 Introduction and Study Objectives

1.1 Introduction

Discharges of industrial effluents into coastal and estuarine waters and the emissions of incinerated urban waste into the atmosphere provide two examples of environmental flows in which water and air quality, respectively, are determined by the behavior and structure of the particle-laden, turbulent, dense/buoyant jets generated by discharges. Industrial power plants discharge residual byproducts into the water bodies (Lattemann and Hoepner, 2008), mostly as submerged jets due to their higher effectiveness.

Moreover, rising populations, shortages of clean and potable water, and advancements in desalination plant technology have increased rapidly in the last decades. In arid and semi-arid countries, desalination plants are actively considered as the best alternative to respond to the high demand for drinkable water. Desalination plants remove the dissolved minerals from coastal water bodies and produce effluents with a high salt concentration, called brines, that may have an elevated temperature too, especially for the Multi-Stage Flash (MSF) desalination plants. Disposal of these brines, which have higher density than the receiving water, causes many environmental impacts, especially in the near field of outfall systems, which is the natural habitat of marine species and fish cultures (e.g. Hashim and Hajjaj, 2005; Lattemann and Hoepner, 2008). Some areas like the Red Sea, Persian Gulf and generally low energy areas with shallow waters are very sensitive to effluent discharges.

Effluent discharge systems of the industrial power plants require to be designed properly in order to minimize the environmental impacts and costs. They also must satisfy the environmental criteria and standards (e.g. US-EPA and EU regulations). Nevertheless, ocean outfall systems are mostly not optimized either regarding environmental impacts or the practical needs. In some cases, the regulations also lack the clear guidelines for ambient water or effluent standards (Jirka, 2004).

The density differences between the effluent and ambient water, represented by the buoyancy flux, make various flow and mixing characteristics of the discharge. In the case of the dense jets, especially brine from Reverse Osmosis (RO) desalination plants, the flow has the tendency to fall as negatively buoyant plume. On the other hand, the buoyant jets (e.g.

effluents from MSF desalination plants) have lower density than ambient water which causes the plume to rise.

The mixing process is divided into two physical regions, where different physical mechanisms predominate. In the first region that is named *near-field*, the mixing is intense; it results mainly from turbulence generated by the initial buoyancy and momentum of the discharge and their interactions with the ambient flow. Beyond this region, the self-induced turbulence will be decayed and mixing just results from ambient oceanic turbulence. In this region which is named *far-field*, dilution increases at a much slower rate than in the near-field (Figure 1.1 and Figure 1.2). The mixing characteristics of only near-field are studied in this thesis.

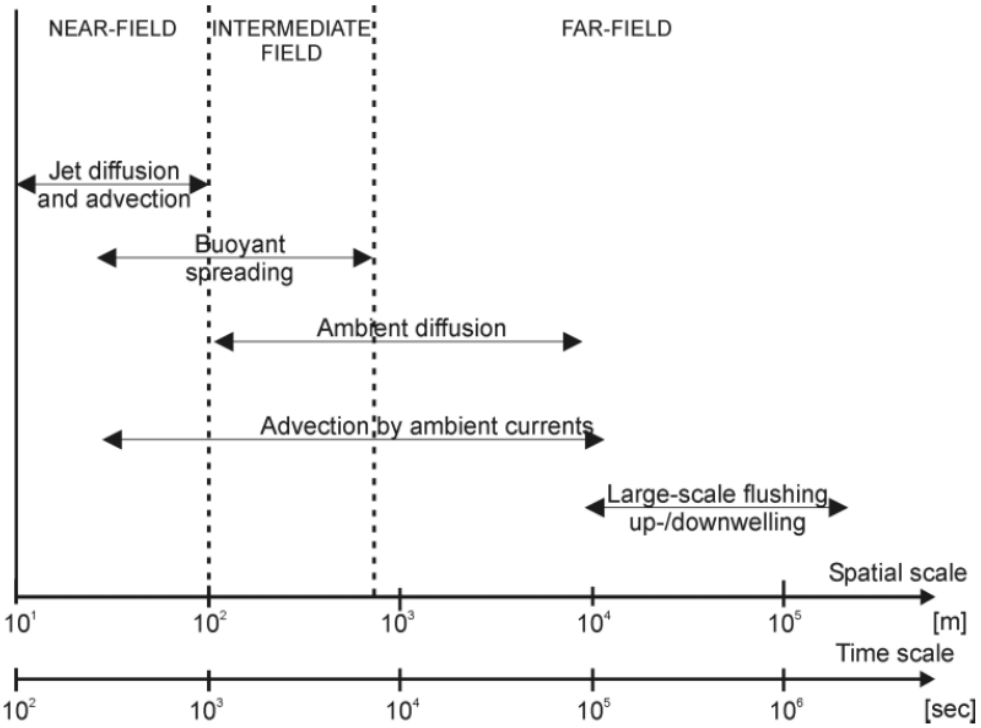

Figure 1.1: Spatial and temporal scales in near-field and far-field mixing process (Source: Jirka et al., 1976).

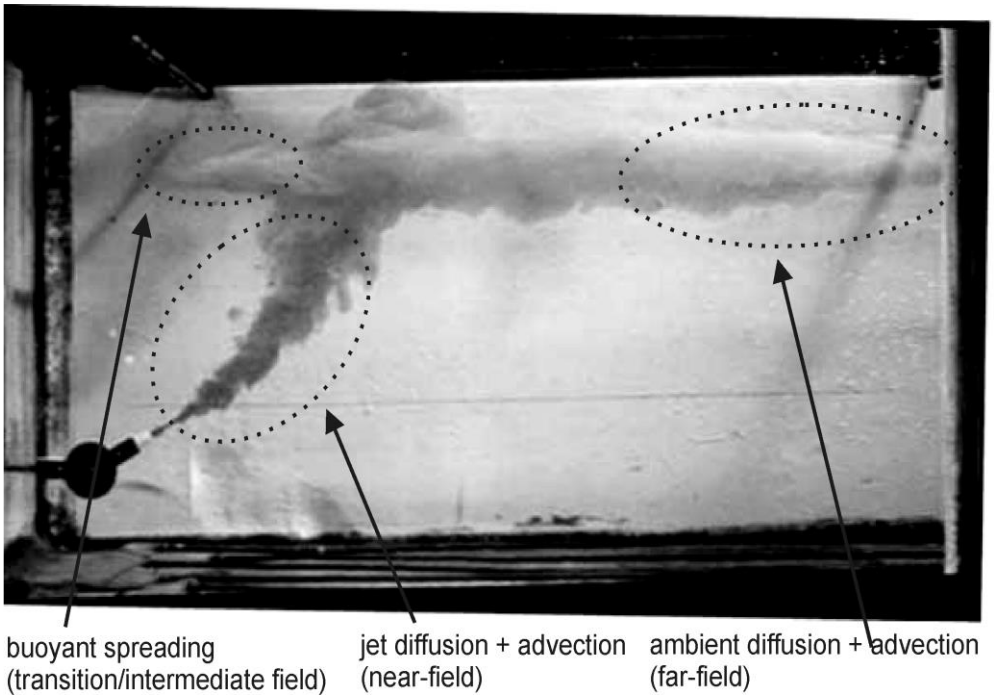

Figure 1.2: Three major domains in positively buoyant jet of a submerged discharge (Source: Jirka et al., 1976).

Discharge outfalls must be designed to minimize environmental impacts and costs while being in compliance with regulatory criteria. The first step before working on the discharge outfall design is to decrease the concentrations of the waste source by some measures within the industrial plant (e.g. decreasing the additive usage, enhancing plant efficiently, pre-treatment technologies, etc.). The second step is the application of improved mixing technologies like submerged diffuser(s), placed in less sensitive regions (offshore, deep waters).

Bleninger et al. (2009) characterized the common effluent discharge and receiving water properties as outlined in the following sections.

1.1.1 Discharge Characteristics

The discharge structure: such as the type of the discharge structure (open channel, submerged/elevated pipe, etc.), the site of the discharge structure (at the bank, in the water body, in the bay, close to break waters or groynes, etc.), the dimensions of the discharge structure (channel cross-section, pipe diameter, multiport installation, etc.), the orientation of the discharge structure (discharge angles relative to prevalent currents or dominant geographical/bathymetrical features).

The effluent: such as the type (municipal/industrial wastewater, combined overflow, drainage water, cooling water, desalination plant effluent), the physical properties (temperature, salinity, viscosity, etc.), the fluxes (volume and momentum flux resulting from flow rate and discharge velocities), the chemical/biological properties (substance/bacteria concentrations, etc.) and the loads (yearly substance loads discharged).

1.1.2 Receiving Water Characteristics

The local conditions near the discharge site: such as the type of water body (river, lake, etc.), the physical properties (temperature, salinity, density, velocities, etc.), the meteorological/hydrological conditions (flow, velocity and water level variations, density variations, reversing/non-reversing flows, etc.) and the topography (meandering river, coastal, bay, etc.).

The regional conditions for the whole water body or for a part of that: such as the proximity to other influencing cases (other discharges, morphological changes, dams, etc.), the proximity to sensitive aquatic ecosystems (mangrove forests, salt marshes, coral reefs, or low energy intertidal areas and shallow coasts) and the general flushing characteristics (residence times, exchange times).

The main problem arises due to the strongly limited mixing behavior in the receiving waters, which is significantly influenced by the effluent density, which is dominated by the varying effluent salinity and temperature. One efficient measure is discharge technologies aiming for enhanced effluent dispersion in the receiving environment and adequate discharge area to avoid pollutant accumulation, to protect sensitive regions and to utilize natural purification processes. Submerged diffuser outfalls such as efficient mixing devices installed at locations with high transport and purification capacities are capable to reduce environmental impacts significantly.

1.2 Research Objectives and Significance

The main objective of this study is to improve understanding of the mixing properties of dense discharge effluent in the receiving waters that have not been previously investigated. These are discharge with inclinations between 60° and 90° and discharge in shallow water with surface attachment (Figure 1.3).

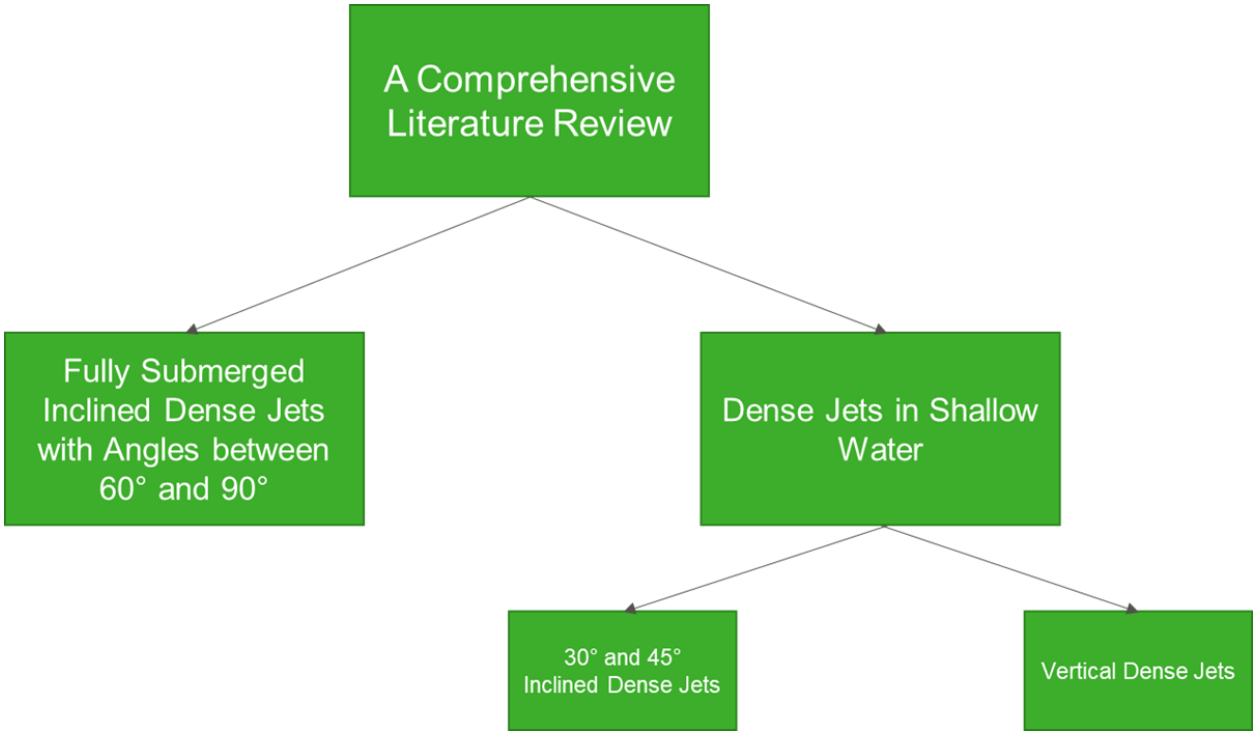

Figure 1.3: Research objective diagram.

A comprehensive literature review was performed to carefully identify the research objectives. The following questions were asked, and this study did its best to address them.

1. Have all jet configurations been studied in effluent discharges into stagnant waters? If not, how are they different to the past configurations that have been studied so far in terms of the jet trajectory and kinematic?

2. What would happen if effluent is discharged into shallow stagnant ambient where there is not enough water column to contain the entire plume?

3. What regimes could be identified in the shallow water discharge application and what are the velocity and concentration characteristics in each?

4. What Reynolds-averaged Navier-Stokes (RANS) turbulence models are effective in the effluent mixing studies in deep and shallow waters?

The significance of the current study in terms of coming up with the study objective was a thorough literature review on the past numerical studies performed on the effluent discharges. This helped with identifying the correct gaps and scoping the research properly.

1.3 Novelty and Contributions of the Study

Several novel elements are proposed and investigated in the current study, as outlined below.

Comprehensive review of CFD studies in the effluent discharge modelling: since early 1990s numerical modelling of effluent discharges initiated, and it has continued since then. However, there was no systematic review of the past studies available up to date. The current study based the main research outlines and objectives on a critical review of past studies in the field. This would also be a benchmark for the other researchers in the field to better align their future work and identify the gaps better.

Modelling of less studied discharge angles: most of the past CFD studies have focused on the common discharge angles of 30°, 45°, 60° and 90°. However, there are cases (Papakonstantis et al., 2011a and 2011b) where discharge angles between 60° and 90° could be designed for effluent discharges. There are limited experimental data available on these angles and there is no detailed CFD study completed for such jets. This study investigated the discharge characteristics of such jets in details. Since these are fully submerged discharges, the turbulence model (i.e. LRR model here) recommended by others (e.g. Gildeh et al., 2015 and 2016) were used to close the Navier-Stokes equations.

Modelling of effluent discharge in shallow waters with surface impingement: to the best knowledge of the research team, there is no prior published research on the effluent discharge modelling in the shallow water where jet outer boundary or centerline impacts the water surface. It is noteworthy that these jets are plausible in practice and understanding of velocity and concentration evolution at the surface attachment area is very critical, especially for design purposes.

Application of new turbulence models: RANS turbulence models were proven to be good models in studying the effluent discharge mixing for various discharge and receiving water conditions (e.g. Gildeh et al., 2015; Yan and Mohammadian, 2017). This study used the best performed RANS turbulence models from past studies and applied two new turbulence models: v2f model, which is a four-equation turbulence model with capabilities to model anisotropic behaviors and SSG model with is a Reynolds stress model (RSM). As past studies showed, the choice of turbulence model is quite important in predicting the jet trajectory and

kinematic properties and thus examining new turbulence models will add to the knowledge of choosing a better model for this application (i.e. effluent discharge).

1.4 Thesis Outline

This thesis is organized as a sequence of technical papers, and as such is divided into six chapters. Following Chapter 1 (current chapter), a detailed literature review is presented in Chapter 2. Chapter 2 intends to provide a critical review on the past CFD (and not experimental) studies in effluent discharge problems as the focus of this thesis is numerical modelling of such jets and not an experimental study. The thorough literature review identified several gags that a few of them were the bases for the next steps of research. *This chapter was published in the Journal of Water*.

Effluent discharge in deep waters with inclinations of 60°, 75°, 80° and 85° were modelled in OpenFOAM using LRR turbulence model and are presented in Chapter 3. The higher inclinations are more suitable for deep water outfalls where terminal rise height of the jet does not attach to the ambient water surface. Such jets, especially 60° jets, are used frequently to discharge industrial effluents. Two different densimetric Froude numbers were simulated for each discharge angle and important geometrical characteristics of the jet trajectory are investigated, i.e., the initial terminal rise height reached by the jet at flow initiation, the final terminal rise height at the steady state, and the point where the jet returns to the nozzle height. *This chapter was published as a book chapter in the Water Engineering Modelling and Mathematic Tools (Elsevier)*.

Effluent discharge in shallow waters with surface attachment for the jet with inclinations of 30° and 45° were modelled in OpenFOAM using various turbulence models and are presented in Chapter 4. Five RANS turbulence models were examined in this study: realizable k-ε and k-ω SST models (known as two-equation turbulence models), v2f (four equations to model anisotropic behavior) and LRR and SSG turbulence models (known as Reynolds stress models - six equations to model anisotropic behavior). Three mixing regimes introduced in Jiang et al. (2014) were reproduced numerically for both discharge angles applying various turbulence models: full submergence, plume contact and centerline impingement regimes (i.e. FSR, PCR and CIR). Key geometrical and dilution properties of these jets at surface contact (X_s, S_s) and return point (X_r, S_r) were extracted numerically and compared to those available

from experiments. *This chapter was published in the Journal of Environmental Fluid Mechanics (Springer).*

Vertical dense effluent discharges are popular in the design of outfall systems. Vertical jets provide the opportunity to be efficient for a range of ambient currents, where the jet will be pushed away not to fall on itself. Chapter 5 focuses on the worst case scenario in terms of mixing and dilution of such jets: vertical dense effluent discharges with no ambient current and in shallow water where jet impacts the surface. This scenario provides a conservative design criteria for such outfall systems. The numerical modelling of such jets has not been studied before and this chapter provides novel, though preliminary, insights in simulations of vertical dense effluent discharges in shallow waters. Turbulent vertical discharges with Froude numbers ranging from 9 to 24 were simulated using a volume of fluid (VOF) model in OpenFOAM. A Reynolds stress model (RSM), based on the results from Chapter 4 was applied to characterize the geometrical (i.e., maximum discharge rise Z_m and lateral spread R_{sp}) and dilution μ_{min} properties of such jets. Three flow regimes were reproduced numerically, based on the experimental data: deep, intermediate and impinging flow regimes. *This chapter has been submitted to the Canadian Journal of Civil Engineering (CJCE) and is currently under review.*

Lastly, Chapter 6 presents the concluding remarks from different chapters and recommendations for further studies.

1.5 List of Publications (form the PhD study)

1. Kheirkhah Gildeh, H., Mohammadian, A., Nistor, I. (2021). "Vertical Dense Effluent Discharge Modelling in Shallow Waters", *Submitted to the Water and Environment Journal*.

2. Kheirkhah Gildeh, H., Mohammadian, A., Nistor, I. (2021). "Inclined Dense Effluent Discharge Modelling in Shallow Waters", *Environ. Fluid Mech. 21, 955–98,* https://doi.org/10.1007/s10652-021-09805-6.

3. Kheirkhah Gildeh, H., Mohammadian, A., Nistor, I. (2021). "Mixing of Inclined Dense Jets: A Numerical Modelling", *Water Engineering Modelling and Mathematic Tools, Elsevier,* https://doi.org/10.1016/B978-0-12-820644-7.00023-2.

4. Mohammadian, A., Kheirkhah Gildeh, H., Nistor, I. (2020). "CFD Modeling of Effluent Discharges: A Review of Past Numerical Studies", *Water, 12,856,* https://doi.org/10.3390/w12030856.

References

Bleninger T, Niepelt A, Jirka GH (2009) Desalination plant discharge calculator. Paper BD 180 for EDS Congress, Baden, Germany

Gildeh, H.K.; Mohammadian, A.; Nistor, I.; Qiblawey, H. Numerical modeling of 30° and 45° inclined dense turbulent jets in stationary ambient, Environ. Fluid Mech. 2015, 15, 537–562.

Gildeh, H.K.; Mohammadian, A.; Nistor, I.; Qiblawey, H.; Yan, X. CFD modeling and analysis of the behavior of 30° and 45° inclined dense jets—New numerical insights. J. Appl. Water Eng. Res. 2016, 4, 112–127.

Hashim A, Hajjaj M (2005) Impact of desalination plants fluid effluents on the integrity of seawater, with the Arabian Gulf in perspective. Desalination 182: 373-393

Jirka GH, Abraham G, Harleman DRF (1976) An assessment of techniques for hydrothermal prediction. Department of Civil Engineering, MIT for U.S. Nuclear Regulatory Commission, Cambridge

Jirka GH (2004) Integral model for turbulent buoyant jets in unbounded stratified flows, Part 1: The single round jet. Environ. Fluid Mech. 4 (2004)1–56

Lattemann S, Hoepner T (2008) Environmental impact and impact assessment of seawater desalination. Desalination 220:1-15

Papakonstantis, I.L., Christodoulou, G.C., and Papanicolaou, P.N. 2011a. Inclined negatively buoyant jets 1: geometrical characteristics, Journal of Hydraulic Research, 49: 3-12.

Papakonstantis, I.L., Christodoulou, G.C., and Papanicolaou, P.N. 2011b. Inclined negatively buoyant jets 2: concentration measurements, Journal of Hydraulic Research, 49: 13-22.

Yan, X.; Mohammadian, A. Numerical Modeling of Vertical Buoyant Jets Subjected to Lateral Confinement. J. Hydraul. Eng. 2017, 143, 04017016.

2 CFD Modeling of Effluent Discharges: A Review of Past Numerical Studies[1]

Abstract: Effluent discharge mixing and dispersion have been studied for many decades. Studies began with experimental investigations of geometrical and concentration characteristics of the jets in the near-field zone. More robust experiments were performed using Laser-Induced Fluorescence (LIF) and Particle Image Velocimetry (PIV) systems starting in the 20th century, which led to more accurate measurement and analysis of jet behavior. The advancement of computing systems over the past two decades has led to the development of various numerical methods, which have been implemented in Computational Fluid Dynamics (CFD) codes to predict fluid motion and characteristics. Numerical modeling of mixing and dispersion is increasingly preferred over laboratory experiments of effluent discharges in both academia and industry. More computational resources and efficient numerical schemes have helped increase the popularity of using CFD models in jet and plume modeling. Numerous models have been developed over time, each with different capabilities to facilitate the investigation of all aspects of effluent discharges. Among these, Reynolds-averaged Navier-Stokes (RANS) and Large Eddy Simulations (LES) are at present the most popular CFD models employing effluent discharge modeling. This paper reviews state-of-the-art numerical modeling studies for different types and configurations of discharges, including positively and negatively buoyant discharges, which have mostly been completed over the past two decades. The numerical results of these studies are summarized and critically discussed in this review. Various aspects related to the impact of turbulence models, such as k-ε and Launder-Reece-Rodi (LRR) models, are reviewed herein. RANS and LES models are reviewed, and implications for the simulation of jet and plume mixing are discussed to develop a reference for future researchers performing numerical investigations on jet mixing and dispersion.

Keywords: effluent discharge; CFD; numerical modeling; mixing; OpenFOAM; dilution; review; inclined dense jet

---

[1] This chapter of the study has been published as: Mohammadian, A., Kheirkhah Gildeh, H., Nistor, I. (2020). "CFD Modeling of Effluent Discharges: A Review of Past Numerical Studies", Water, 12,856, https://doi.org/10.3390/w12030856.

2.1 Introduction

Increasing population and industrial growth have meant a global increase in effluent discharge in water bodies. Industries located near shore that discharge significant volumes of thermal and saline effluent include desalination plants, mining operations, water treatment plants, and nuclear power plants.

The direct discharge of wastewater into lakes, rivers, and seas can increase turbidity and change the ambient temperature [1]. Salinity is also a major public and scientific concern [2]. Coastal waters receive concentrated salt brine as discharge from seawater desalination plants (Figure 2.1), chemical waste from biofouling (e.g., chlorine), and fertilizers. The water bodies that receive the industrial discharge are often very sensitive environments [3,4], and the design of the discharge facility to disperse effluent and reduce the concentration of effluents may help protect the receiving water body.

Figure 2.1. Surface discharge of the Al-Ghubrah desalination plant, the largest such facility in Oman (Source: H.H. Al-Barwani).

Ref. [5] noted that certain coastal ecological zones are particularly vulnerable to effluent discharges, including salt marshes, mangrove forests, coral reefs, and other low-energy intertidal areas. The Persian Gulf and the Red Sea are particularly sensitive to effluent due to their low hydro-dynamism.

Local fisheries, tourism industries, and other economic consequences are affected by the health of coastal environments. The mixing and dispersion qualities of jets were first noted in the 1950s. Length-scale and integral models were among the first numerical studies on jet and

effluent mixing; however, these models are only briefly described here, as the focus of this paper is to review CFD studies on jet mixing.

Length-scale models use relationships calibrated based on experimental data to forecast the steady-state behavior of the effluent discharge. These models use non-dimensional numbers to categorize discharge regimes (see Section 2.1 for details) and are fast to process. However, they are sensitive to user error and Monte Carlo testing, and thus an experienced user may be required to interpret the data when the result is near the boundary of two regimes, as small changes induce large differences in these models [6]. As well, these models are often inaccurate when used on different parameters than those for which they were validated [7]. NRFIELD [8–10] and CORMIX [11] are two commonly used length-scale models.

Jet integral models, according to [6], solve mass and momentum conservation equations based on the assumptions that the velocity profiles of jets have no radial variation, and that the jet profile is axisymmetric and Gaussian. In the 1950s and 1960s, first-order jet integral models were proposed by [12,13] based on the jet entrainment closure approach and by [14,15] based on the jet diffusion approach. Refs. [16–18] developed second-order jet integral models. Visual Plumes [19] and CORMIX (CorJet, based on the integral model [18]) are two popular mixing tools based on jet integral models.

According to [6], the integral models are less reliable when there is any of the following: (i) the discharge's initial momentum and buoyancy acting in opposite directions, resulting in instabilities on the edge, as observed in the inner half (lower half) of inclined dense jets [20,21]; (ii) noticeable interaction between the mean flow and the jet, (iii) an unsteady mean ambient flow; (iv) a great effect due to horizontal or lateral boundaries [18]; (v) an unstable near-field area, with a re-entrainment of concentrated effluent into jet [11]; or, (vi) a large re-entrainment of concentrated effluent from mid- and far-fields into the near-field jet due to tidal cycles [22].

Jet flow modeling by the CFD tools is not perfect, but it is an improvement over the parameter-based jet integral and length scale models. Issues that remain with CFD tools include the following: (i) accuracy, (ii) stability, (iii) computational time, (iv) complicated codes that require expert knowledge to use them efficiently and accurately, and (v) simulations that need calibrating and validating.

Turbulent length-scale models are often resolved with a turbulence model to parameterize unresolved mixing and dispersion scales. One should apply turbulence models with caution, as they sometimes provide stable but unrealistic solutions, such as when they are applied to physical scenarios for which they have not been validated.

When using a CFD model, it can be a challenge to create and resolve the mesh and to define appropriate boundary conditions (e.g., intensity and the turbulence dissipation rate). A high mesh resolution is often needed for a stable solution, even when the turbulence model is a good match. This means that CFD modeling is numerically expensive. Even with current computing systems, accurate CFD models for near-field dispersion and mixing might need simulation times of several days or weeks. This is much more expensive compared to the parametric-based models that can produce results on the order of minutes and seconds [6]. There is a balance between model stability, numerical diffusion, mass and momentum conservation, boundedness, and computational cost. These choices can significantly influence the estimation of modeled concentration.

However, once built, calibrated, and validated, CFD models can produce high-resolution three-dimensional images of jet mixing and dynamics. CFD models are free from some of the assumptions that restrict integral models. Since CFD models do not require the assumption of a steady-state condition or self-similarity in the jet profile, they can include a variety of external effects such as the presence of surface waves and encompass a wide range of boundary conditions to allow users to directly simulate the boundary interaction.

CFD modeling of jet discharges has been approached in a variety of ways, including both hydrostatic and non-hydrostatic approaches to the Reynolds-averaged Navier-Stokes (RANS) and the Large Eddy Simulations (LES) models. Both models have functioned well over the past decade to simulate effluent discharges [23–27]. RANS models are based on a time-averaging method and result in a time-averaged mean velocity field, which is averaged over a longer time period than the time constant of the velocity fluctuations and results in a constant mean velocity without nuance for time-dependent variations. LES is based on filtering instead of averaging. A filter size is identified, and flow scales equal to or larger than this size are calculated exactly, and scales smaller than the filter size will be modeled. The smaller the filter size, the more concise the calculated time variation resolution of the velocity vectors. RANS models are more numerically efficient than LES models, while providing

enough detail for engineering applications. Thus, they have become the most prevalent CFD models used for the design of outfall systems.

The Direct Numerical Simulation (DNS) method is less applicable to engineering problems, functioning more as a research tool. It is CPU-intensive, as it attempts to resolve Navier-Stokes equations with no approximation of the turbulence and requires a very fine numerical resolution to capture all the turbulence details. It basically resolves entire turbulence scales temporally and spatially. Mesh systems should be very fine to resolve all the spatial scales [28].

The hydrostatic pressure assumption in CFD models has been widely used to model shallow water systems in which the horizontal length scale of the problem is much larger than the vertical length scale. Ref. [29] stated that brine discharges from a desalination plant in the near field is a case in which the non-hydrostatic pressure approach should be adopted as the eddy viscosity and the acceleration terms in the momentum equation are comparable to that of the gravitational acceleration term for the vertical velocity component.

Table 2.1 (after [7]) summarizes the existing modeling packages (commonly used in the industry) for the simulation of jet and plume mixing.

Table 2.1. Existing modeling packages for simulation of jet and plume mixing.

Models	Mathematical Approaches for Jet/Plume Mixing	Availability	Major Functionalities and Capabilities
CORMIX [11]	Empirical solutions; Eulerian jet integral method	Commercial model	Prediction of jet and (or) plume geometry and dilution in the near field; single or multiple jets
VISJET	Lagrangian jet integral method	Commercial model	
Visual PLUMES	Empirical solutions; Eulerian and Lagrangian jet integral methods	Free package	
NRFIELD	Empirical solutions	Free package	Prediction of jet and (or) plume geometry and dilution in the near field of multiport diffusers
Sophisticated Multidisciplinary Models			
OpenFOAM	FVM; RWPT method	Free package	Predictions of ocean hydrodynamics; pollutant fate and transport in the near and far fields; water quality; sediment processes
MIKE21/3	FVM; RWPT method	Commercial package	
Delft3D	FDM; RWPT method	Free package	
ANSYS CFX	FVM; RWPT method	Commercial package	
ANSYS Fluent	FVM; RWPT method	Commercial package	
FLOW-3D	FDM; RWPT method	Commercial package	
TELEMAC-2D/3D	FEM; RWPT method	Free package	
EFDC–Hydro	FDM; RWPT method	Free package	Predictions of ocean hydrodynamics; Pollutant dispersion in the far field; Near-field processes using the embedded jet model JETLAG; Suspended sediment transport
HydroQual–ECOMSED	FDM; RWPT method	Free package	Predictions of ocean hydrodynamics; Pollutant fate and transport in the far field; Sediment processes

Notes: FVM: Finite Volume Method, FDM: Finite Difference Method, RWPT: Random Walk Particle Tracking.

The objectives of this review paper are to (i) provide an overview of the theoretical advancements on jet mixing modeling, (ii) review the current state-of-the-art research on CFD modeling of jets and plumes, (iii) investigate the most common turbulence models used in the jet mixing modeling, and (iv) indicate areas of research needs. These objectives are accomplished by completing a thorough literature review, discussing research gaps, and outlining the methodological solutions to address current and future research needs.

This paper is organized in the following order: Section 2 presents the numerical details of jet studies, including dimensional analysis, that govern numerical equations. Section 3 reviews numerical studies on inclined dense jets. Numerical studies of vertical jets, horizontal jets, and surface discharges are reviewed in Sections 4, 5, and 6, respectively. The discharge port configuration is discussed in Section 7. Finally, the conclusions complete the study.

2.2 Jet Studies: Details of Numerical Analysis

Most CFD codes for numerical jet studies employ the following theories.

2.2.1 Dimensional Analysis

This section introduces the dimensional analysis and fluid governing equations used in the numerical analysis of effluent discharges.

Figure 2.2 shows a sketch of an inclined dense jet with negative buoyancy in stagnant ambient water. The effluent discharges with an initial jet velocity U_0, jet density ρ_0, jet nozzle diameter D, angle θ to the horizontal, and ambient water density ρ_a (with $\rho_0 > \rho_a$). As it is discharged, the jet reaches a maximum or terminal rise height, y_t, and then falls due to the negative buoyancy, mixing with the ambient water. The jet lands on the seabed and then it spreads horizontally as a density current.

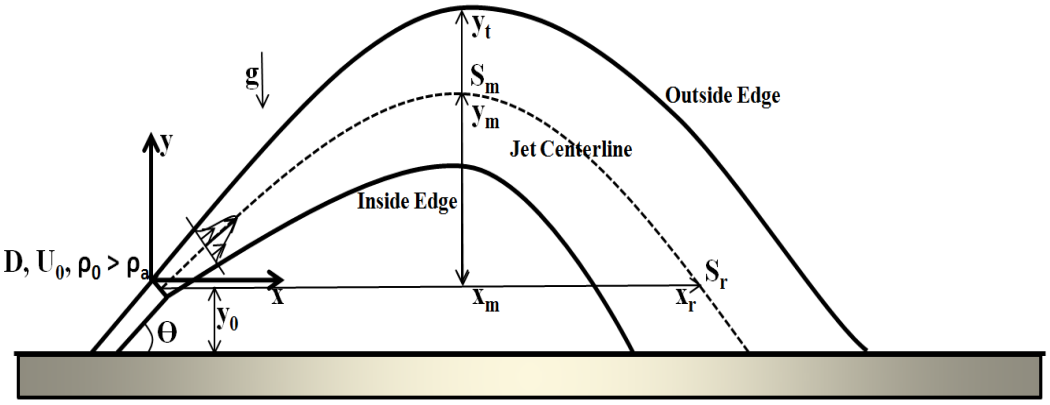

Figure 2.2. A schematic view of an inclined dense jet with negative buoyancy in stagnant ambient water.

The dispersion of concentration relies on both ambient and jet characteristics, including U_0, D, and θ, described above, plus the initial density difference $\Delta\rho_0 = \rho_0 - \rho_a$, the jet discharge concentration, C_0, the turbulence intensity of the jet, I_{TJ}, and the ambient water depth H_a. The jet densimetric Froude number (Fr_d) is a key parameter for dense jet analysis. Fr_d is the ratio

of inertia to buoyancy, and it is calculated with the reduced gravitational acceleration (g_0') as follows:

$$Fr_d = \frac{U_0}{\sqrt{g_0' D}} \tag{2.1}$$

$$g_0' = \left(\frac{\Delta\rho_0}{\rho_a}\right) g \tag{2.2}$$

Inclined negatively buoyant jets are described in the equations that follow, using the buoyancy flux (B_0), the jet discharge volume flux (Q_0), and the kinematic momentum flux (M_0):

$$Q_0 = U_0 \pi \frac{D^2}{4} \tag{2.3}$$

$$B_0 = Q_0 g_0' \tag{2.4}$$

$$M_0 = U_0^2 \pi \frac{D^2}{4}. \tag{2.5}$$

A characteristic length, such as the maximum terminal rise height (y_t), for a jet may be written with the momentum and source length scales (L_M and L_Q), using dimensional analysis as follows:

$$\frac{y_t}{L_M} = f\left(\frac{L_M}{L_Q}, \theta\right) \tag{2.6}$$

The return point dilution, S_r, and centerline peak dilution, S_m, can be expressed as:

$$\frac{S_r \text{ or } S_m}{Fr_d} = f(Fr_d, \theta) \tag{2.7}$$

2.2.2 CFD Governing Equations

The time-averaged Navier-Stokes equations, as follows, govern the CFD mechanisms.

The continuity equation governs the conservation of mass:

$$\frac{\partial u}{\partial x} + \frac{\partial v}{\partial y} + \frac{\partial w}{\partial z} = 0 \tag{2.8}$$

Momentum is also conserved, as shown in the following equations:

$$\frac{\partial u}{\partial t} + u\frac{\partial u}{\partial x} + v\frac{\partial u}{\partial y} + w\frac{\partial u}{\partial z} = -\frac{1}{\rho}\frac{\partial P}{\partial x} + \frac{\partial}{\partial x}\left(v_{eff}\left(\frac{\partial u}{\partial x}\right)\right) + \frac{\partial}{\partial y}\left(v_{eff}\left(\frac{\partial u}{\partial y}\right)\right) + \frac{\partial}{\partial z}\left(v_{eff}\left(\frac{\partial u}{\partial z}\right)\right) \tag{2.9}$$

$$\frac{\partial v}{\partial t}+u\frac{\partial v}{\partial x}+v\frac{\partial v}{\partial y}+w\frac{\partial v}{\partial z} = -\frac{1}{\rho}\frac{\partial P}{\partial y}+\frac{\partial}{\partial x}\left(\upsilon_{eff}\left(\frac{\partial v}{\partial x}\right)\right)+\frac{\partial}{\partial y}\left(\upsilon_{eff}\left(\frac{\partial v}{\partial y}\right)\right)+\frac{\partial}{\partial z}\left(\upsilon_{eff}\left(\frac{\partial v}{\partial z}\right)\right) - g\frac{\rho-\rho_0}{\rho} \quad (2.10)$$

$$\frac{\partial w}{\partial t}+u\frac{\partial w}{\partial x}+v\frac{\partial w}{\partial y}+w\frac{\partial w}{\partial z} = -\frac{1}{\rho}\frac{\partial P}{\partial z}+\frac{\partial}{\partial x}\left(\upsilon_{eff}\left(\frac{\partial w}{\partial x}\right)\right)+\frac{\partial}{\partial y}\left(\upsilon_{eff}\left(\frac{\partial w}{\partial y}\right)\right)+\frac{\partial}{\partial z}\left(\upsilon_{eff}\left(\frac{\partial w}{\partial z}\right)\right) \quad (2.11)$$

where t is time; u, v, and w are the mean velocity components in the x, y, and z directions, respectively; υ_{eff} is effective kinematic viscosity ($\upsilon_{eff} = \upsilon_t + \upsilon$); υ_t is turbulent kinematic viscosity; P is fluid pressure; g is gravitational acceleration; ρ is fluid density; and ρ_0 is the reference fluid density.

Dividing by density (ρ) and adding the term of buoyancy to the vertical momentum equation accounts for variable density effects. Then, the seawater equation of the state is used to calculate the density for both the jet and the ambient water [30].

The advection-diffusion equations are used to model the concentration and temperature changes over time.

$$\frac{\partial C}{\partial t}+u\frac{\partial C}{\partial x}+v\frac{\partial C}{\partial y}+w\frac{\partial C}{\partial z} = d\left(\frac{\partial^2 C}{\partial x^2}+\frac{\partial^2 C}{\partial y^2}+\frac{\partial^2 C}{\partial z^2}\right) \quad (2.12)$$

$$\frac{\partial T}{\partial t}+u\frac{\partial T}{\partial \mathrm{x}}+\mathrm{v}\frac{\partial \mathrm{T}}{\partial \mathrm{y}}+\mathrm{w}\frac{\partial \mathrm{T}}{\partial \mathrm{z}} = k_{\mathrm{eff}}\left(\frac{\partial^2 \mathrm{T}}{\partial \mathrm{x}^2}+\frac{\partial^2 \mathrm{T}}{\partial \mathrm{y}^2}+\frac{\partial^2 \mathrm{T}}{\partial \mathrm{z}^2}\right) \quad (2.13)$$

$$k_{eff} = \frac{\upsilon_t}{Prt}+\frac{\upsilon}{Pr} \quad (2.14)$$

where T is the fluid temperature, C is the fluid concentration (salinity), d is the diffusion coefficient, k_{eff} is the heat transfer coefficient, Pr is the Prandtl number, and Pr_t is the turbulent Prandtl number.

2.3 Discharge through Inclined Dense Jets

An inclined jet is discharged at an angle of 0° to 90° from the horizontal and may be positively or negatively buoyant. Most of the inclined jets used in engineering applications are negatively buoyant jets, which are also known as inclined dense jets. Most high-density discharge outfalls are designed as inclined jets due to their proven near-field dilution rate and efficiency.

Many new Computational Fluid Dynamics (CFD) techniques were developed in the 1970s, but detailed and reliable experimental data were difficult to come by. In the 1990s, Particle Image Velocimetry (PIV) and Laser-Induced Fluorescence (LIF) experimental techniques provided more reliable data, and these studies became benchmarks for CFD model validation. [31] and others performed some numerical studies on jet mixing in the 1990s, but [32] were the first to fully apply CFD tools to estimate the effluent discharge jet flow behavior. Vafeiadou simulated dense effluent discharges at 45°, 60°, 70°, 80°, and 90° inclinations, by using the ANSYS CFX with a mesh of 400,000 elements and adopting the k-ω Shear Stress Transport (SST) turbulence model. Comparing Vafeiadou's results with experimental data by [33,34], it appeared that their numerical results agreed, supporting the further use of such numerical models to estimate the characteristics of dense effluent discharges. Vafeiadou's study pioneered the use of CFD for the mixing of effluent discharges into water bodies.

Ref. [35] also used ANSYS CFX and applied the standard k-ε turbulence model for the RANS equations closure. Experimental data of dense effluent discharges were simulated by the k-ε turbulence model using both a standard and adjusted turbulent Schmidt number of S_{ct} = 0.9. Both of these simulations with the k-ε turbulence model were more accurate than the integral models and the analytical solutions. In the experimental studies, the buoyancy-induced instabilities were observed on the lower (inner) half of the jet. However, in the study of [35], the k-ε simulations (both the standard and the calibrated) underpredicted the spread of the jet and the integrated centerline dilution at the top rise of the jet, because they overestimated the influence of the stabilizing density gradients. This study only achieved qualitative comparisons and did not arrive at any conclusions about which model performed the best.

Ref. [24] used OpenFOAM to explore the numerical modeling of 30° and 45° inclined dense jets in calm ambient water conditions. OpenFOAM has a solid structure of various solvers, including a wide range of turbulence models that could be used to the jet mixing and dispersion analysis. This study focused on how the choice of the turbulence model can affect the jet trajectory and predicted dilution and the importance of turbulence closure in the Navier-Stokes equations. They applied five RANS turbulence models to investigate the accuracy of the CFD predictions: the Launder-Reece-Rodi (LRR) Reynolds stress model, the Launder-Gibson Reynolds stress model, the RNG k-ε linear eddy viscosity model, the

realizable k-ε linear eddy viscosity model, and a non-linear k-ε eddy viscosity model. A summary of these turbulence models is discussed in [36].

Ref. [24] discretized the temporal term with a first-order implicit Euler scheme. The standard finite volume method with a Gaussian integration was used to discretize the advection-diffusion terms. The preconditional conjugate gradient (PCG) scheme was used to solve the pressure field, and the preconditioned biconjugate gradient (PBiCG) scheme was used for the other fields: U, T, C, k, ε and ω. This study focused on analyzing the inclined dense discharge, including the jet trajectories, jet terminal rise height, jet centerline peak, jet centerline, and jet horizontal return point (i.e., impact point). The modeled values for velocity and concentration profiles were compared to experimental data. The effects of the increased jet velocities of the high Froude numbers observed in field applications were investigated with a sensitivity analysis. Ref. [24] found that of the turbulence models tested in their study, the realizable k-ε and LRR models were more accurate than the other three tested. Tables 2.2 and 2.3 (after [24]) summarize the results for these two models (only presented 30° jets for the sake of brevity).

The geometry, concentration, and velocity fields in the near field of effluent discharges can be characterized when the jet flow pattern is understood. Figure 2.3 presents the normalized concentration maps (C/C_0, where C is the computed concentration and C_0 is the discharge concentration) and the dilution isolines for inclinations of 30° and 45°; realizable k-ε and LRR turbulence models were used for each case.

Effluent discharge trajectory is an important factor in the design of ocean outfall systems. Discharge trajectory would basically identify the flow path that a jet would travel through until it impacts the bed. A dilution equation (Equation (2.15); C_a is ambient concentration) was used to calculate the dilution values for plotting in Figure 2.3. The discharge trajectory and flow growth are also illustrated in Figure 2.3 as the jets travel downstream with clear differences between the two turbulence models. LRR is an anisotropic turbulence model and performs more reliably for calculating the shear forces on jet edges and providing more realistic predictions. Tables 2.2 and 2.3 summarize the discharge trajectory and flow growth compared to other turbulence models.

$$S = (C_0 - C_a)/(C - C_a) \tag{2.15}$$

Table 2.2. Comparison of numerical and experimental coefficients for the 30° inclined jets (Source: [24]). LIF: Laser-Induced Fluorescence, LRR: Launder-Reece-Rodi.

Parameter	Proportionality Coefficient	[24]		[21]		[20]			[37]	[38]	[39]
		Realizable k-ε	LRR	$0.10 \leq y_0/L_m \leq 0.15$	$y_0/L_m > 0.15$	LA data	LIF data	Theory			
Terminal rise height	$\frac{Y_t}{L_M}$	1.13	1.13	1.13	–	1.14	1.34	1.08	1.49	1.15	1.22
Horizontal location of return point	$\frac{X_r}{L_M}$	3.40	3.34	3.06	3.19	3.34	3.66	3.14	3.51	3.22	3.70
Return point dilution	$\frac{S_r}{Fr}$	1.27	1.31	1.18	1.45	–	–	–	1.90	–	–
Vertical location of centerline peak	$\frac{Y_m}{L_M}$	0.71	0.69	0.70	–	0.59	0.70	0.66	–	0.84	–
Horizontal location of centerline peak	$\frac{X_m}{L_M}$	2.05	1.97	1.81	1.64	1.86	1.97	1.81	–	2.07	–
Centerline peak dilution	$\frac{S_m}{Fr}$	0.65	0.63	0.62	0.66	–	–	–	–	–	0.36

Table 2.3. Evaluation of performance of two turbulence models (realizable k-ε and LRR models) for 30° inclined jet (Source: [24]).

Parameter	Proportionality Coefficient	[24]		Average of Experiments	Absolute Difference (%)	
		Realizable k-ε	LRR		Realizable k-ε	LRR
Terminal rise height	$\frac{Y_t}{L_M}$	1.13	1.13	1.22	8.09	8.09
Horizontal location of return point	$\frac{X_r}{L_M}$	3.40	3.34	3.37	1.04	0.75
Return point dilution	$\frac{S_r}{Fr}$	1.27	1.31	1.51	18.90	15.27
Vertical location of centerline peak	$\frac{Y_m}{L_M}$	0.71	0.69	0.70	1.91	0.97
Horizontal location of centerline peak	$\frac{X_m}{L_M}$	2.05	1.97	1.86	10.22	5.91
Centerline peak dilution	$\frac{S_m}{Fr}$	0.65	0.63	0.55	18.90	15.24

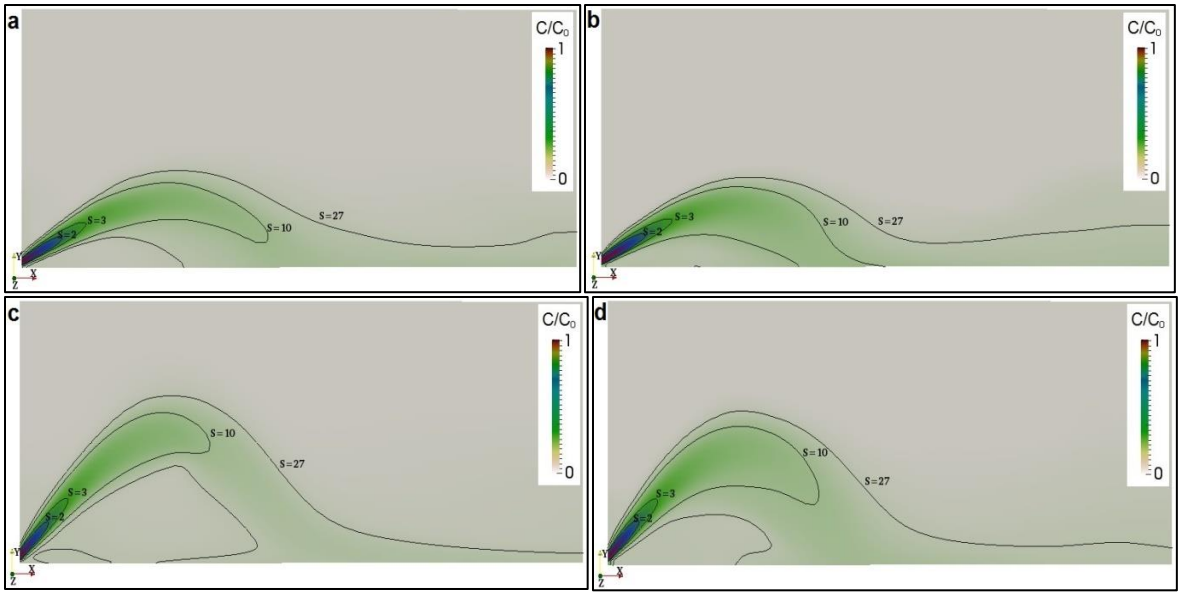

Figure 2.3. Mixing regimes for 30° and 45° inclined dense jets. (a) 30°, realizable k-ε; (b) 30°, LRR; (c) 45°, realizable k-ε; (d) 45°, LRR (Source: [25]).

The jet centerline often follows the maximum cross-sectional velocity or concentration along the flow path perpendicular to the discharge trajectory. The best way to extract the centerline is to start at the nozzle and create a velocity vector map. Ref. [40] noted that the maximum concentration and velocity profiles almost coincide, but the maximum concentration profile usually decreases more quickly than the velocity. The momentum and the buoyancy-induced instabilities also affect the trajectories of the inclined dense discharges. While the discharge rises close to the nozzle, negative buoyancy forces affect the upward momentum and decrease it until they dominate the concentration transport (somewhere after the discharge rise peak) and the maximum concentration profile sinks down toward the bed faster than the velocity maximum profile. The centerline results in [24] were extracted following the maximum cross-sectional velocity similar to [40].

Ref. [25] used the buoyancy modified standard k-ε model and the two best performing models in [24] (realizable k-ε and LRR) for inclined dense jets. They modified the standard k-ε turbulence scheme to include the standard Boussinesq gradient diffusion hypothesis (SGDH) and the general gradient diffusion hypothesis (GGDH). The governing equations for the k-ε turbulence model that includes the buoyancy term are as follows:

$$\frac{\partial k}{\partial t} + u_i\left(\frac{\partial k}{\partial x_i}\right) = \frac{\partial}{\partial x_i}\left(\frac{\nu_t}{\sigma_k}\frac{\partial k}{\partial x_i}\right) + P + G - \varepsilon \tag{2.16}$$

$$\frac{\partial \varepsilon}{\partial t} + u_i\left(\frac{\partial \varepsilon}{\partial x_i}\right) = \frac{\partial}{\partial x_i}\left(\frac{\nu_t}{\sigma_\varepsilon}\frac{\partial \varepsilon}{\partial x_i}\right) + C_{1\varepsilon}\frac{\varepsilon}{k}(1 - C_{3\varepsilon})(P + G) + C_{2\varepsilon}\frac{\varepsilon^2}{k} \tag{2.17}$$

where the shear production term P and the buoyancy production term G in the k-ε turbulence model in Equation (16) are calculated as follows:

$$P = \nu_t\left(\frac{\partial u_i}{\partial x_i} + \frac{\partial u_j}{\partial x_i}\right)\frac{\partial u_i}{\partial x_j} \tag{2.18}$$

$$G = \frac{\overline{\rho' u_i'}}{\bar{\rho}^2}\left(\frac{\partial P}{\partial x_i} + \rho g_i\right) \tag{2.19}$$

The way the term $\overline{\rho' u_i'}$ in Equation (19) is solved defines the SGDH and GGDH methods. The corresponding equations for SGDH and GGDH are as follows, respectively.

$$\overline{\rho' u_i'} = \frac{-\upsilon_t}{Pr_t}\frac{\partial \bar{\rho}}{\partial x_j} \tag{2.20}$$

$$\overline{\rho' u_i'} = \frac{-3}{2}\frac{C_\mu}{Pr_t}\frac{k}{\varepsilon}\left(\overline{u_i' u_j'}\frac{\partial \bar{\rho}}{\partial x_i}\right) = \frac{-3}{2}\frac{\nu_t}{Pr_t\,\rho^2\,k}\left(\overline{u_i' u_j'}\frac{\partial \bar{\rho}}{\partial x_i}\right) \tag{2.21}$$

The modified SGDH and GGDH k-ε turbulence models were used in OpenFOAM to explore the influence of the buoyancy term, using turbulence coefficients C_μ = 0.09, $C_{1\varepsilon}$ = 1.44, $C_{2\varepsilon}$ = 1.92, and a calibrated coefficient, $C_{3\varepsilon}$ for sensitivity tests with $C_{3\varepsilon}$ = 0.9, 0.6, and 0.4.

Figure 2.4 shows numerical and experimental results for a 45° inclined dense jet on the central plane. The standard k-ε results are relatively close to the data by experiments, both with and without modifications (Figure 4a). Adding the buoyancy term to the turbulence model causes the jet to spread more along the inner (lower) half of jet, where stronger buoyancy-induced forces would be experienced. When the buoyancy effects are set to be stronger (i.e., with a smaller $C_{3\varepsilon}$), the discharge growth rate is larger, and the numerical results align more closely to the data by experiments (not presented in this paper). The SGDH and GGDH methods showed similar results when the computed and experimental discharge trajectories were compared. This could be attributed to the small difference in density between the discharge and the receiving water (smaller than 1%). The buoyancy effect on the effluent discharge mixing characteristics should be

investigated further, especially for larger density differences between the discharge and ambient water (larger than 1% in this study) as well as $C_{3\varepsilon}$ calibration for mixing applications.

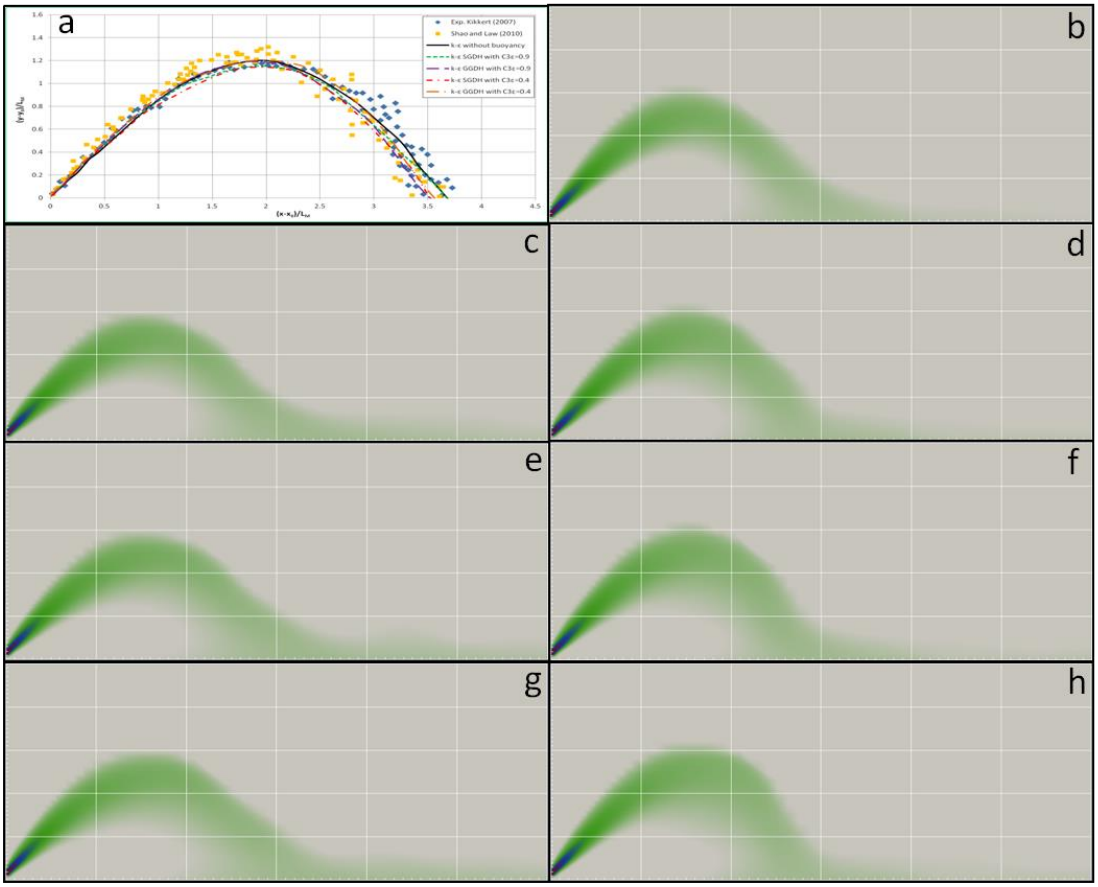

Figure 2.4. Overall discharge trajectory for 45° inclined dense jets (Source: [25]). (a) Centerline comparison (modeled vs. experiments); (b) standard k-ε; (c) modified k-ε with SGDH, $C_{3\varepsilon}$ = 0.9; (d) modified k-ε with GGDH, $C_{3\varepsilon}$ = 0.9; (e) modified k-ε with standard Boussinesq gradient diffusion hypothesis (SGDH), $C_{3\varepsilon}$ = 0.6; (f) modified k-ε with general gradient diffusion hypothesis (GGDH), $C_{3\varepsilon}$ = 0.6; (g) modified k-ε with SGDH, $C_{3\varepsilon}$ = 0.4; (h) modified k-ε with GGDH, $C_{3\varepsilon}$ = 0.4.

Ref. [25] further studied the concentration and velocity effects on the dispersion properties and the discharge growth rate for the 30° and 45° inclinations (Figure 2.5). The figure presents the normalized cross-sectional concentrations for the 30° and 45° discharges using the realizable k-ε and LRR turbulence models. The realizable k-ε model predicts a narrower jet width than the LRR model does. The jets predicted by Linear Eddy Viscosity Models (LEVMs) are usually thinner than the ones predicted using the Reynolds Stress Models (RSMs), due to the assumption of isotropic turbulence in the LEVMs. The improved behavior of the LRR model could be due to stress anisotropy.

LEVMs are less expensive numerical models than the RSMs. There are reasons that justify extra terms in the RSMs over the two-equation models such as k-ε for the mixing application. To begin with, Reynolds stresses are affected by the pressure strain term through both the turbulent fluctuations (which is related to the gradient in mean velocity) and to the turbulence–turbulence interaction (eddies effects in the fluctuation of pressure), which do not relate directly to the mean flow changes. The first process is called rapid pressure, and the second is known as slow pressure.

This affects the energy redistribution between stress components, which is important in estimating the degree of the stresses' anisotropy. Inclined dense discharges disperse according to the interaction of eddies. Therefore, both the rapid pressure and slow pressure terms may be important. It is possible that the reason the LRR model works well is that it includes both the slow and rapid pressure terms.

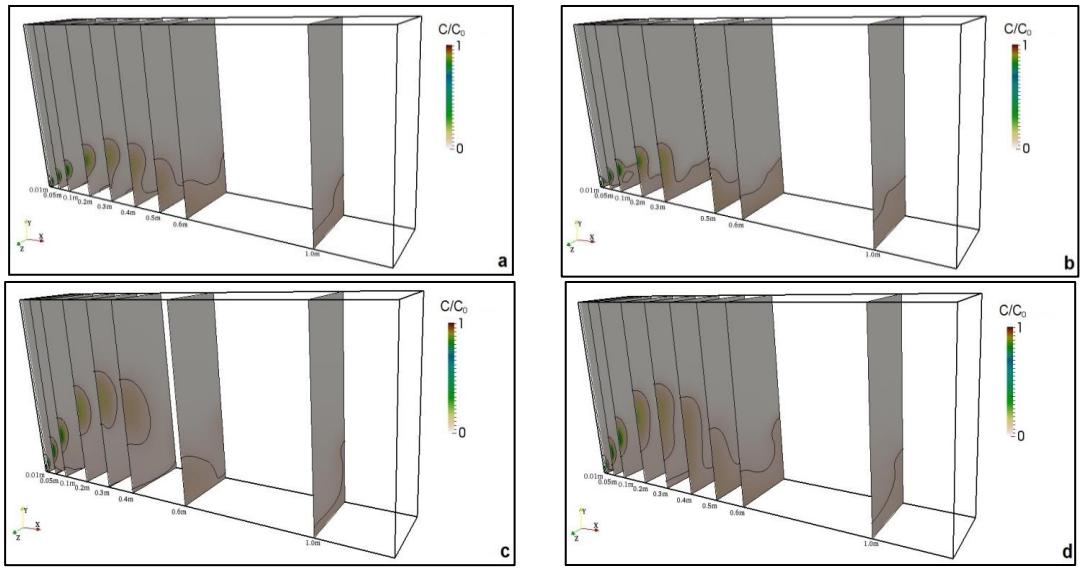

Figure 2.5. Discharge growth width at various cross-sections: the contour lines represent S = C_0/C = 1 (Source: [25]). (a) 30°, realizable k-ε; (b) 30°, LRR; (c) 45°, realizable k-ε; (d) 45°, LRR.

OpenFOAM was used to simulate 45° inclined discharges using the LES method and the Smagorinsky and Dynamic Smagorinsky sub-grid scale (SGS) by [26]. This resulted in numerical predictions including geometrical characteristics, the jet trajectory, jet spread, and eddy structures. Eddy sizes in the LES method are based on the grid spacing. In LES models, large eddies are simulated directly by computing the Navier-Stokes equations, but small eddies are simulated using, for instance, Boussinesq hypothesis assumptions. The simulations were run

with the twoLiquidMixingFoam solver in OpenFOAM. Most of the parameters in Table 2.2 were used to compare [26]'s study results with other experimental and numerical studies. Eddy structures and turbulence characteristics were computed utilizing the experimental data of [41–43] for comparison. The coherent structure of the inclined dense discharge plays an important role in the development of flow in the jet and can help elucidate the mixing properties and the intensity of turbulence.

LES seemed to underestimate the turbulence intensity in the area of buoyancy-induced instabilities (i.e., lower half of the jet), as reported by [26]. For turbulent flows, the effect of the small scales on the simulated resolved scales are accounted for with an SGS approach. To complete the closure, for the Smagorinsky model, the parameter (C_s) in the eddy viscosity, $\upsilon_t = \rho(C_s \triangle)^2 S_{ij}$, where Δ is the LES filter size and S_{ij} is the strain rate tensor, needs to be specified. The accuracy in choosing this parameter is directly related to the kinetic energy dissipation.

In 1991, [44] made an important addition to turbulence theory and modeling when they proposed a model for the dynamic determination of C_s. Rather than obtaining the minimal coefficient from predetermined expressions, the model analyzed large-scale turbulences during the numerical simulation to deduce them. This dynamic model approach was proved to be more applicable in the cases with complex interactions.

Ref. [6] predicted the mixing and dispersion of inclined dense discharges in stagnant surroundings by developing a three-dimensional CFD model that uses the CFD tool named Fluidity [45]. Fluidity uses a range of control volumes and finite element discretization to solve the 3D Navier-Stokes equations using unstructured mesh; it is capable of including Coriolis effects, density variations, turbulence models, tidal forcing, and associated buoyancy forces. Fluidity includes an anisotropic adaptive mesh capability that controls the solution accuracy locally throughout the model domain. The standard k-ε and V-LES (very-large eddy simulation) models in the dense jet simulations were used to close the Navier-Stokes equations. Although they only studied the 60° jet for the centerline rise height, impact point, and its dilution, and though their study was preliminary and not detailed in terms of model validation and comparisons, it seems that their model underpredicted the terminal rise height, the distance from the nozzle to the impact point, and the minimum dilution at impact point compared to the

experimental data. This could be due to little water entrainment toward the jet centerline; therefore, the simulated jet is not as diluted as it should be. This could be attributed to the mesh used in their preliminary study.

Ref. [27] built upon their previous study [26] to include the tail of the return point density current analysis with the LES model in OpenFOAM. The standard k-ε RANS turbulence model was run to compare the results to the LES model, and the 45° and 60° inclinations were selected. The jet spreading layer thickness was defined as the lateral distance where the concentration would reach 5% of the maximum concentration at the jet centerline. The 60° jet spreading layer results were compared to those from experiments by [37]. Similar to the study of [26], the eddy structures and concentration profiles were plotted along the jet trajectory, and the results showed that LES was well able to predict the return point location and the coordinates of the centerline peak. However, their model underestimated the dilution at the return point by approximately 20% compared to data collected by previous experiments. This could be due to the mesh resolution that was adopted in this study, as they argued. Comparing to the experimental data, LES was able to reproduce the concentration density in the density current region, while k-ε results could not do that. It was observed that for both geometrical and flow/dilution characteristics, k-ε results were generally lower in values compared to the LES results.

Ref. [46] built on the work of [26,27] by studying the effect of swirls at the outfall nozzles. Experimentally, they found that the addition of swirls at the nozzles lowered the terminal rise height of inclined dense discharges and increased the dilution rate at the return point. This could potentially affect the outfall design for coastal waters. Their numerical study is the first of its kind for the CFD modeling of swirls in effluent discharges. Similar to [27], two approaches were taken in consideration for this study: (i) LES using the dynamic Smagorinsky sub-grid approach and (ii) RANS using the standard k-ε turbulence model. In the case with swirls at the nozzle, RANS had a better performance than LES when the results were compared to the experimental data, which could be due to the reduction in turbulence anisotropy and more axisymmetric distribution of turbulence. On the other hand, in the case of no swirls at the nozzle, LES performance was superior, as it could account for the anisotropy in a more accurate manner. When the swirls number (maximum tangential velocity divided by the discharge velocity at the nozzle) was larger

than 0.33, it was observed that both RANS and LES models underestimated the dilution of discharge.

2.3.1 Discussion on Differences in RANS and LES Models for Effluent Mixing Problems

RANS and LES models are very popular models in the modeling of effluent discharges in ambient waters, as reviewed in the studies above. Navier-Stokes equations were described before in Equations (8) to (11). Reynolds decomposition involves splitting any instantaneous quantity in mean and fluctuating components by time averaging for both velocity and momentum equations. RANS equations resemble basic governing equations, except for the turbulent momentum and density fluxes, which results from the Reynolds decomposition and averaging. Six unknown terms of the Reynolds stress tensor and three unknown terms of the density flux term imply that the number of unknowns is larger than the available equations. Therefore, it leads to an undetermined system of equations commonly referred to as the closure problem. To resolve this severe shortcoming, several hypotheses and methods are prescribed. The turbulent viscosity and gradient-diffusion hypotheses are the most widely used concepts to deal with the closure problem. The turbulent viscosity hypothesis (TVH) assumes that the deviatoric Reynolds stress is proportional to the mean shear strain rate as [47]:

$$-\left(\overline{u_i' u_j'}\right) + \frac{2}{3} k \delta_{ij} = -v_t \left(\frac{\partial \overline{U}_i}{\partial x_j} + \frac{\partial \overline{U}_j}{\partial x_i}\right) = 2 v_t \overline{S_{ij}} \tag{2.22}$$

where $k = \left(\frac{1}{2}\right) u_i'^2 = 0.5(u'^2 + v'^2 + w'^2)$ is the turbulent kinetic energy and v_t is the turbulent eddy viscosity. The gradient-diffusion hypothesis (GDH) assumes that the turbulent density (scalar) flux is aligned with the mean density (scalar) gradient as [47]:

$$-\left(\overline{\rho' u_j'}\right) = -\kappa_t \left(\frac{\partial \rho}{\partial x_j}\right) \tag{2.23}$$

where κ_t is a positive scalar that is named the turbulent eddy diffusivity. These hypotheses resolve the closure problem by decreasing the number of unknowns, but they still require a correct proposition for the turbulent viscosity and diffusivity.

Different closure schemes are introduced widely to define the turbulent viscosity (v_t). Regarding how to solve for v_t, in terms of additional equations, these closure schemes are

classified as zero-equation, one-equation or two-equation models. Zero-equation or algebraic models do not require additional partial differential equations (PDEs) for transport equations and provide a prediction of the turbulent viscosity (υ_t) directly from the mean flow variables. One-equation models involve the use of one additional transport equation (usually turbulent kinetic energy) and assess the turbulent viscosity (υ_t) based on the estimated turbulent quantity. Two-equation RANS closure schemes such as the standard k-ε model make use of two more transport equations for turbulence quantities to define the turbulent viscosity (υ_t). However, to provide closure for the turbulent flux term in the density transport equation, most turbulence schemes make use of a turbulent Prandtl number (Pr_t) instead of defining the turbulent diffusivity (κ_t) explicitly. The turbulent Prandtl number is defined as:

$$Pr_t = \frac{\upsilon_t}{\kappa_t} \tag{2.24}$$

Due to averaging, the accuracy of RANS models is always a concern in mixing problems, and the development of more robust numerical schemes is an ongoing effort. On the other hand, LES models are now getting more attention, especially with the advancement in computational resources. LES models would resolve the unsteady nature of large eddies and use turbulence models for small-scale eddies. To handle this, LES uses a filtering technique to split the velocity field into mean (U) and residual (u') values. The filter size can either be determined implicitly by the numerical domain grid size or by introducing filter functions [48]. The LES equations for a 3D unsteady-state flow using Boussinesq approximation can be written as follows:

$$\frac{\partial(U_i)}{\partial t} + \frac{\partial(U_i U_j)}{\partial x_i} = -\frac{1}{\rho_0}\frac{\partial(p)}{\partial x_i} + \upsilon\frac{\partial^2(U_i)}{\partial x_i \partial x_j} - g\frac{(\rho)}{\rho_0}\delta_{i3} - \frac{\partial \tau_{ij}^{SGS}}{\partial x_i} \tag{2.25}$$

The filtered density transport equation is:

$$\frac{\partial(p)}{\partial t} + \frac{\partial(\rho U_j)}{\partial x_i} = \kappa_m \frac{\partial^2(p)}{\partial x_i \partial x_j} - \frac{\partial \chi_j^{SGS}}{\partial x_j} \tag{2.26}$$

In Equations (25) and (26), τ_{ij}^{SGS} and χ_j^{SGS} are the SGS tensor and sub-grid scale flux vector respectively and are defined as:

$$\tau_{ij}^{SGS} = \left(U_i U_j\right) - (U_i)(U_j) \tag{2.27}$$

$$\chi_j^{SGS} = (\rho U_j) - (\rho)(U_j) \tag{2.28}$$

With the existence of residuals, similar to RANS models, LES suffers from the closure problem and requires SGS models to resolve closure. The accuracy of LES is related to the efficiency of SGS models used to define the SGS motions. The simplest and most well-known closure method is introduced by [49]. A linear turbulent viscosity (υ_t) is used to model the residual motions as:

$$\tau_{ij}^{SGS} = -2\upsilon_t(S_{ij}) \tag{2.29}$$

The computational studies on the mixing of effluent (review of previous studies in this paper) in the near-field region showed that, especially for LES models, the influence of small changes in the discharge momentum (i.e., inflow momentum) can result in large variations in the concentration field [50]. As seen in previous studies, for effluent mixing problems, RANS models perform relatively well in replicating the geometrical and flow properties of effluent discharges and thus need more exploration in terms of the sensitivity of these models to various input parameters. RANS models are very popular in mixing applications between researchers and professionals, as it has a low CPU demand and is still an appropriate methodology. There are some applications such as the mixing of toxic agents that the models should go beyond the estimate of mean concentration and should resolve smaller scales of the fluid motions. In these cases, LES models are a suitable approach, and they have been an approved method based on studies in the past few years.

2.4 Vertical Jets

Vertical discharges have traditionally been preferred over inclined jets when there are horizontal confinements, and they are usually more suitable for deep waters where there is enough height in the water column to diffuse the concentration. This section reviews the previous CFD studies completed on vertical jets. Unlike inclined dense discharges, this section includes both positively and negatively buoyant jets. Vertical jet modeling is attractive for researchers due to its simplicity and practicality.

Ref. [51] modeled a confined turbulent buoyant discharge using [52]'s realizable k-ε model and modified it to account for turbulence due to buoyancy. They also validated the numerical

model with an experimental study, which included the jet temperature, axial velocities, radial velocity, dynamic pressure, centerline velocity, mass, and momentum fluxes. This study is limited because it only performs 2D modeling of the 3D experiment. Numerically, they compared the realizable k-ε model with other k-ε models (standard k-ε, RNG k-ε, and k-ω) for temperature propagation in the jet. The realizable k-ε model performed the best among all models, especially closer to the nozzle, and it satisfies some constraints in the Reynolds' stresses, which make it more suitable for this specific physics of flow. Ref. [24] made a similar recommendation but for inclined dense discharges. They expressed an essential coefficient of the realizable k-ε model, C_μ, as a function of mean flow and turbulence properties, instead of assuming that it was a constant as in the standard model. This expression (i.e., realizability) satisfies certain constrains on the Reynolds stresses, which makes this model stronger compared to the other k-ε models for mixing problems.

Ref. [53] also studied vertical dense discharges, with both experimental and numerical investigations. A single round outfall was modeled experimentally and numerically. Several numerical simulations were completed with the ANSYS Fluent CFD package, and the numerical results were compared to the experimental data. They considered a homogeneous ambient water with no current and reported the geometrical and concentration properties of the discharge along its trajectory. A wide range of conditions was covered by studying various combinations of port diameters and concentrations of effluent salinities. Their experimental results were compared to the experimental data in the literature. However, this study only compared the numerical results with previous semi-empirical formulas, so it lacks comparison to a good experimental dataset, even to their own data. The numerical model also identified a penetration depth and the existence of multiple peaks for the brine concentration.

Ref. [54] investigated laterally confined vertical buoyant jets with the OpenFOAM model. They modified the standard k-ε turbulence model with the GGDH buoyancy approach and linked the Prandtl and turbulent Prandtl numbers to the Froude number. They verified the model using experimental results from [55] and extracted normalized concentration Gaussian profiles along the jet centerline, perpendicular to the trajectory. Ref. [56] calculated the free jet concentration and comparing this to the modeled confined jet concentration in this study shows

that using the same Froude number gives a higher dilution at a certain point along the jet centerline in confined jets. The study had the following results:

- An assumption was made that improves the determinacy and aids in the calibration of CFD modeling, which is: the Prandtl number Pr and turbulent Prandtl number Pt_r would be related to the densimetric Froude number Fr_d:

$$Pt_r = Pr = (0.032Fr_d + 0.89) - 1 \tag{2.30}$$

- The influence of water surface is smaller than the influence of confinement, although the distribution of concentration along a cross-section in a confined discharge could be impacted by boundaries.
- A conclusion was made to enable engineers and researchers to quickly estimate the evolution of a laterally confined vertical buoyant discharge, which is that the rate of discharge concentration growth is almost equal to $b_{gc}/s = 0.0938$, where b_{gc} is the concentration $1/e$ width (e is the Napier's constant) and that is where the jet concentration reaches to $1/e$ of the centerline maximum concentration.

Ref. [57] used the OpenFOAM model to simulate the mixing properties of vertical buoyant jets discharged from multiport diffusers. Four turbulence models were investigated: standard k-ε, RNG k-ε, k-ω, and SST k-ω. By comparing cross-sectional variations of mean axial velocities at different elevations, they observed that the RNG k-ε model performed the best of the four models. By varying the ratio of the port spacing over the port diameter, they demonstrated that the port spacing affects the dilution characteristics of the jets (i.e., the concentration decreases with increasing port spacing). This study found that when the merging point is located above the nozzle, the centerline concentration drops to approximately 20% of the initial concentration, and the port spacing effect becomes less important. Therefore, a logarithmic term was added to derive a new empirical formula, which includes the port spacing effect to describe the centerline dilution:

$$\frac{C_m}{C_0} = \alpha\left(\frac{y}{d_p}\right)^{\beta} - \gamma \ln\left(\frac{p_s}{d_p}\right) \tag{2.31}$$

where d_p is the port diameter, p_s is the port spacing, and α, β, and γ are regression coefficients.

2.5 Horizontal Jets

There are two categories of horizontal jets: offset jets and wall jets. Wall jets are attached to a solid boundary (usually at the bottom), and offset jets are elevated away from the bottom and experience no effects from the wall. This section covers numerical studies on both types to date.

Ref. [58] simulated horizontal buoyant wall jets in three dimensions by applying a realizable k-ε model to analyze results for temperature dilution, centerline trajectory, and cling length at various sections, as well as jet velocity. They compared their results to those of [59,60]. A linear relationship was found for the cling length as a function of the densimetric Froude number: $L/D=3.2Fr_d$. An exponential relationship was found for the jet centerline velocity.

The conclusions from [58] included the following. (i) Temperature dilution is related to the nozzle diameter D, the distance of the jet trajectory to the nozzle x, and the densimetric Froude number Fr_d. The temperature dilution in the wall jet region decays according to Equation (32). (ii) The central surface velocity profiles resemble that of a turbulent wall jet and generally agree with the classical curve of wall jets. (iii) The velocity profile shows strong similarity in the vertical plane beyond an $x > 5D$ distance from the nozzle, fitting to a Gaussian shape. (iv) The centerline velocity decay is related to the densimetric Froude number Fr_d and the nozzle diameter D and fits Equation (33), where U_0 is the velocity at the source and U_{m0} is the centerline maximum velocity.

$$S = 0.0725x/D + 0.85 \tag{2.32}$$

$$U_0/U_{m0} = 0.65x/(DFr_d^{0.5}) + 0.3 \tag{2.33}$$

Ref. [61] used the LES model to study, for the first time, the interaction between a parallel offset jet and a plane wall jet; the large eddies were simulated directly, and the small eddies were obtained with the Dynamic Kinetic energy Sub-grid-scale Model (DKSM) and the Dynamic Smagorinsky-Lily Model (DSLM). In predicting the turbulent intensity and the mean stream-wise velocity, the agreement was good between the numerical results and the experimental data, especially for DKSM.

Ref. [61] also analyzed some aspects of the turbulence mechanism, such as the function of correlation, the velocity Probability Density Function (PDF), and the coherent structures. In some locations, the mean stream-wise velocity profiles were similar a certain distance after merging

two jets. Near the jet exit, the velocities along the centerline of the two jets were negative. The stream-wise velocities and turbulent intensity both became positive and rapidly increased to the maximum after a stagnation point, and then they gradually decreased downstream; this shows that the interaction of jets is dominant near the exit. Finally, tracer characteristics were used to demonstrate the dilution by the dual jet. The constant concentration was maintained in both the stream-wise and wall normal directions close to the exit because of the interaction between the two jets and the presence of the wall. After the two jets merge completely, the concentrations (C/C_0) are distributed in the wall normal direction parabolically, while the maximum value decreases along the stream-wise direction linearly. The concentration (C/C_m) profiles were similar in the region with a steady C_0 value.

Horizontal wall jets (Figure 2.6) were examined by [23], using a finite-volume model (FVM) and several turbulence models. Their study aimed to discover whether the RANS models were suitable for predicting the velocity and concentration properties of wall jets. They also aimed to identify the best performing turbulence model. The jets were modeled with OpenFOAM, and those turbulence models were compared to those from the numerical studies of [58,59] (Fr_d = 11.61 to 42.33). The linear (standard k-ε, RNG k-ε, realizable k-ε and SST k-ω) and Reynolds stress (Launder-Gibson and LRR) turbulence models were tested in their study. This was the first study for wall jet modeling that compared several turbulence models.

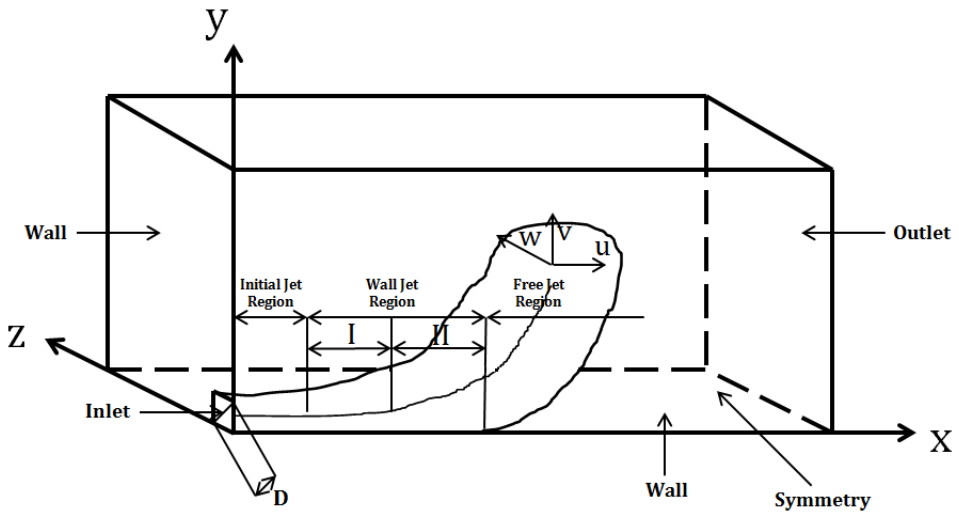

Figure 2.6. Schematic view of the model by [23].

As the fluid leaves the nozzle in a wall jet attached to the horizontal wall and discharging effluent into a water body, water entrains the jet from all directions except for the wall region. Therefore, there is a higher pressure exerted on the top of the jet than on the wall, and the jet stays on the wall up to the point where the suction pressure from above reduces, and the buoyancy force exceeds the pressure difference. There are four regions for wall buoyant jets: (i) Initial Jet Region: from the inlet to the point where the velocity profile is equal to the maximum initial velocity, and nearly uniform; (ii) Wall Jet Region I: from the end of the Initial Jet Region to the point where the jet centerline departs from the horizontal and starts rising; (iii) Wall Jet Region II: from the end of Wall Jet Region I to the point where the outer layer of the jet rises up off the floor; and (iv) Free Jet Region: starts after the Wall Jet Region. These regions are shown in Figure 2.6.

The cling length for thermal wall jets is the distance from the nozzle to the location where the floor temperature reaches $(T - T_a)/(T_0 - T_a) = 3\%$ [58]. Figure 2.7 shows the numerical cling length results from [23] compared to the experimental data and numerical results of [58].

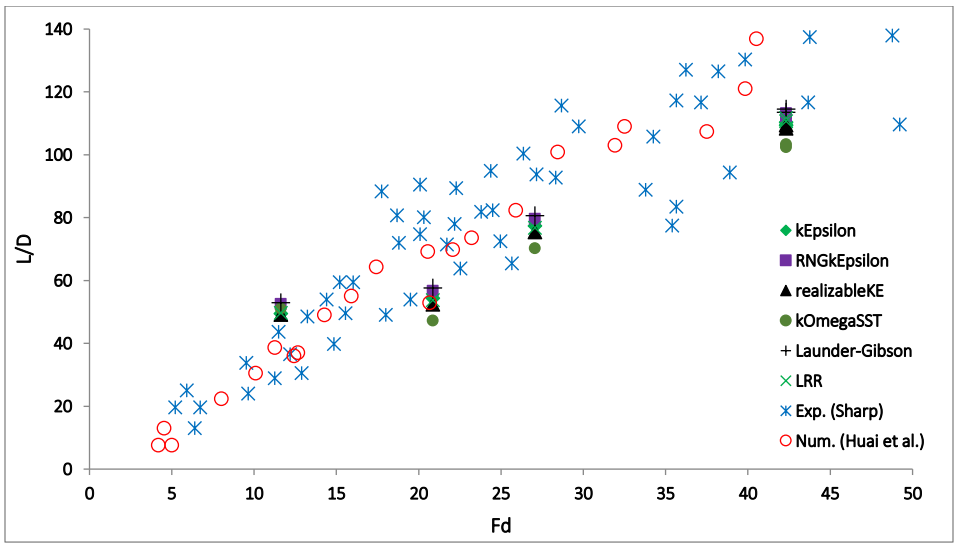

Figure 2.7. Cling length comparison of numerical vs. experimental results (Source: [23]).

The results agreed with both the other researchers' numerical data and the experimental data. For larger Froude numbers, the cling length values reported by [59] were smaller than those from [58], though they align well with the numerical results obtained by [23]. Table 2.4 shows the relationships between L/D and Fr_d for each turbulence model evaluated in [23].

Table 2.4. Cling length relationship for the various turbulence models of Gildeh et al. (2014a).

Turbulence Model	Standard k-ε	RNG k-ε	Realizable k-ε	SST k-ω	Launder-Gibson	LRR	Experiment [62]
Cling Length	$L/D =$ $2.68Fr_d$	$L/D =$ $2.76Fr_d$	$L/D =$ $2.65Fr_d$	$L/D =$ $2.50Fr_d$	$L/D =$ $2.79Fr_d$	$L/D =$ $2.70Fr_d$	$L/D = 3.2Fr_d$

All of the turbulence models estimated a smaller L/D than the experimental data. RNG k-ε has the closest cling length value to the experimental result, and SST k-ω has the smallest.

Predicting jet trajectories is a key factor in the outfall design to predict the path that a jet travels from the exit point until it reaches the surface. This is particularly critical in locations where the receiving water is not deep enough to dilute the effluent completely. Figure 2.8 shows trajectories from several studies, including that of [23]. It seems that the trajectory results from the family of k-ε turbulence models are much more accurate than the SST k-ω model.

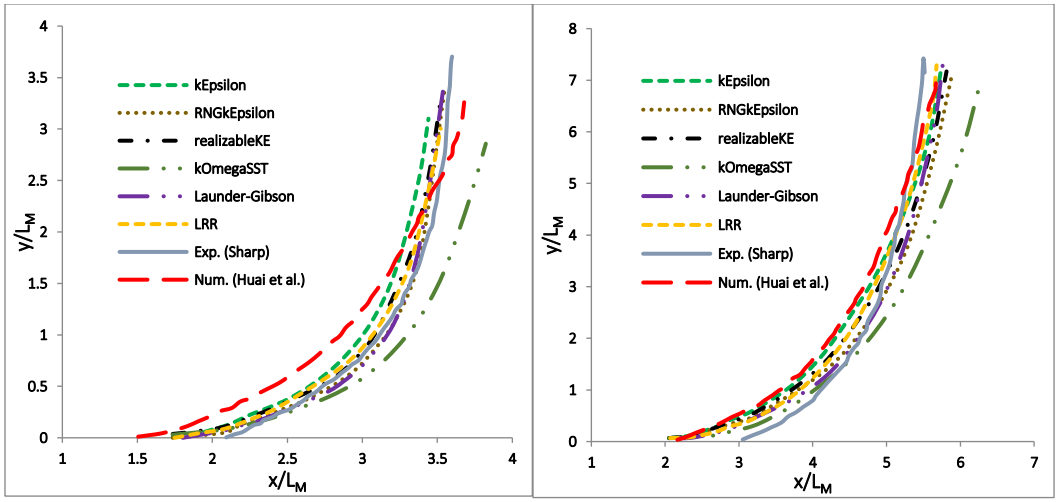

Figure 2.8. Centerline trajectory. (a) Fr_d: approximately 12; (b) Fr_d: approximately 20 (Source: [23]).

Ref. [23] obtained detailed results on stream-wise velocity profiles (Figure 2.9). The stream-wise (x-y) velocity profiles of the buoyant wall jet centerline were extracted from various simulations. The velocity field results were obtained for different jet cross-sections along the x-direction (various values of x/D) at the symmetry plane. In Figure 2.9, the variables are as follows: U_m is the x-direction velocity (along y at the central plane), U_{m0} is the maximum of U_m, with the ordinate of y, and $y_{m/2}$ is the velocity-half-height, which is the height where $U_m=U_{m0}/2$. All profiles

for stream-wise velocity are self-similar and in good agreement with the data by [63], as plotted in Figure 2.9. Ref. [60]'s equation, which is suitable for 2D wall jets, is also plotted along with other data for comparison. Ref. [60]'s equation reads:

$$\frac{U_m}{U_{m0}} = 1.48\left(\frac{y}{y_{m/2}}\right)^{1/7}\left[1 - erf\left(0.68\frac{y}{y_{m/2}}\right)\right] \quad (2.34)$$

Profiles of various values of x/D showed a good similarity as seen in Figure 2.9. Buoyancy-induced instabilities justify the larger deviations in the farther x/D locations as they mostly happen at higher elevations (i.e., $y/y_{m/2} > 1$) where the momentum forces dissipate, and buoyancy forces get stronger. The literature often reports the velocity self-similarity profiles at the central plane for both experimental and numerical studies, although usually without presenting results for the offset measurement from the centerline.

Experimental data for offset velocity profiles were first reported by [63] for two offset sections, $z/D = 1.818$ and $z/D = 3.636$. The current study compared numerical results with [63] as well as [60]'s equation, as shown in Figure 2.10, in which $y_{m/2}$ is the local length scale and U_{ms} is the maximum velocity for the offset sections. As seen in the figure, the numerical results (current study) for $z/D = 3.636$ do not agree well with Verhoff's curve in the area close to the nozzle ($x/D = 5$ and $x/D = 10$). This is primarily due to the development of the jet in the tank width (Figure 2.11). As z/D increases, the jet may not develop at the values along the width of the tank yet, and thus the scatters show less self-similarity.

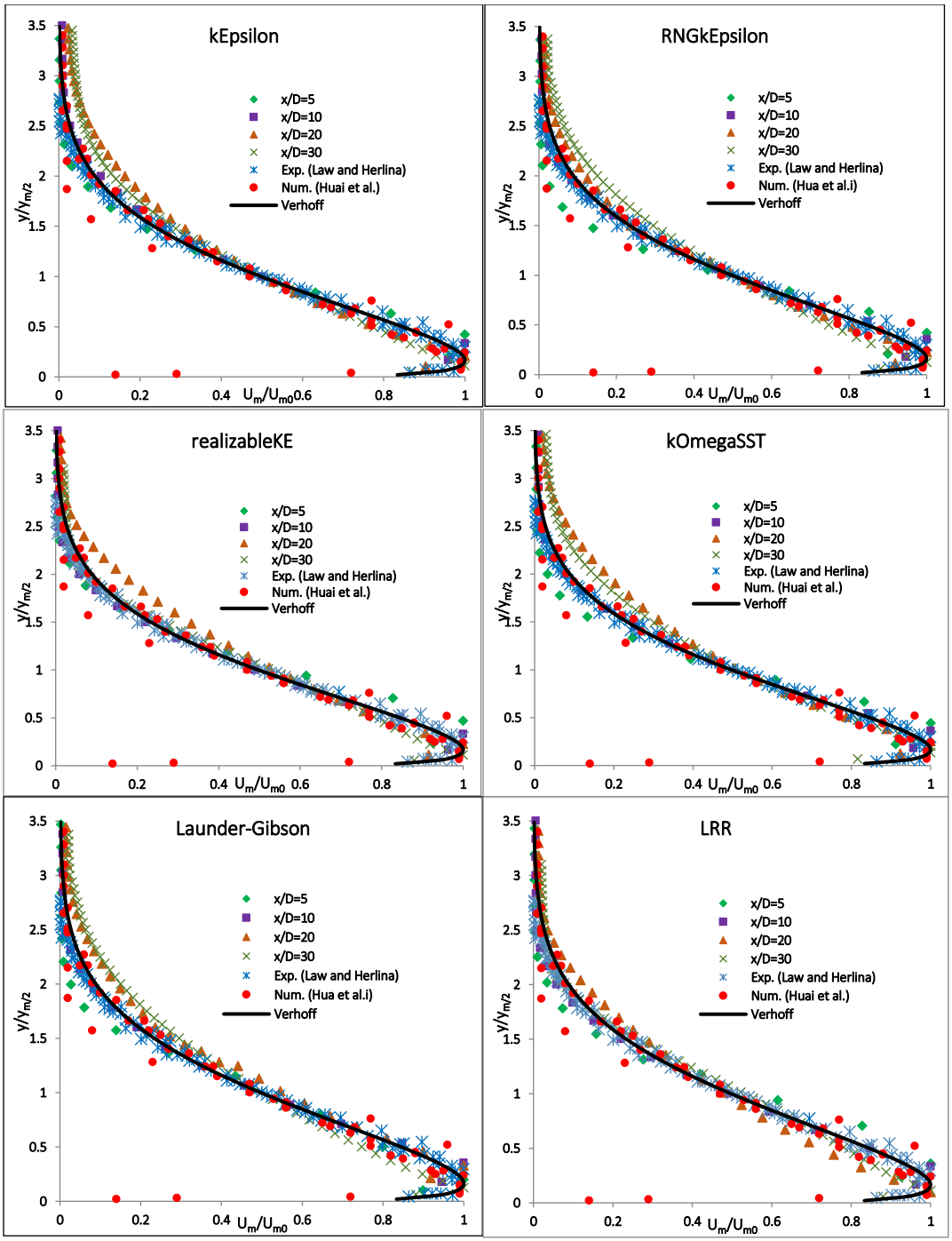

Figure 2.9. Self-similarity of stream-wise velocity profiles for various turbulence models (Source: [23]).

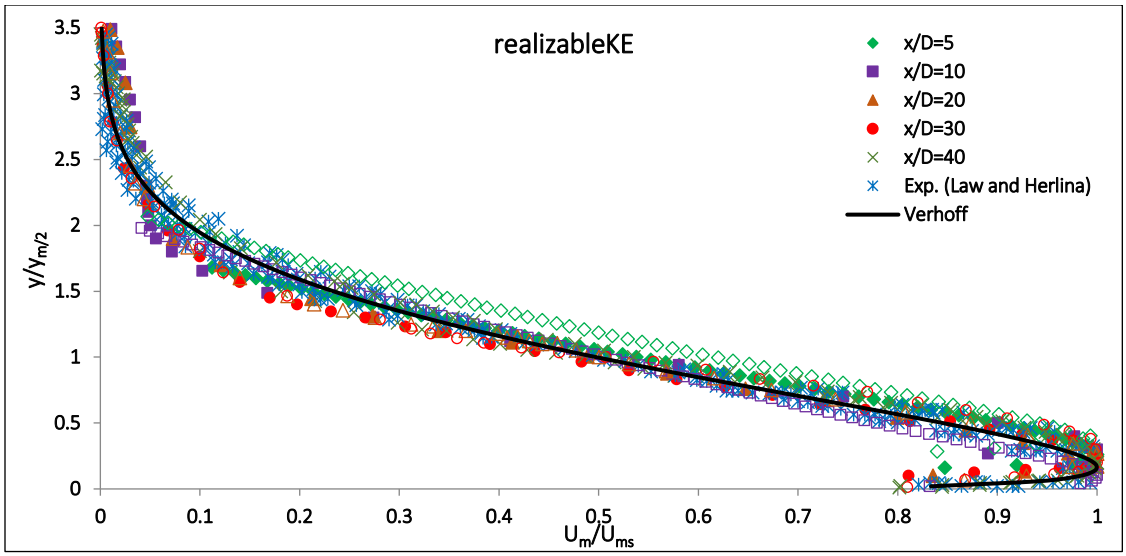

Figure 2.10. Velocity at offset sections z/D = 1.818 and 3.636. Solid fill scatters are for z/D = 1.818 and the no-fill scatters are for z/D = 3.636 at the x/D values on the plot.

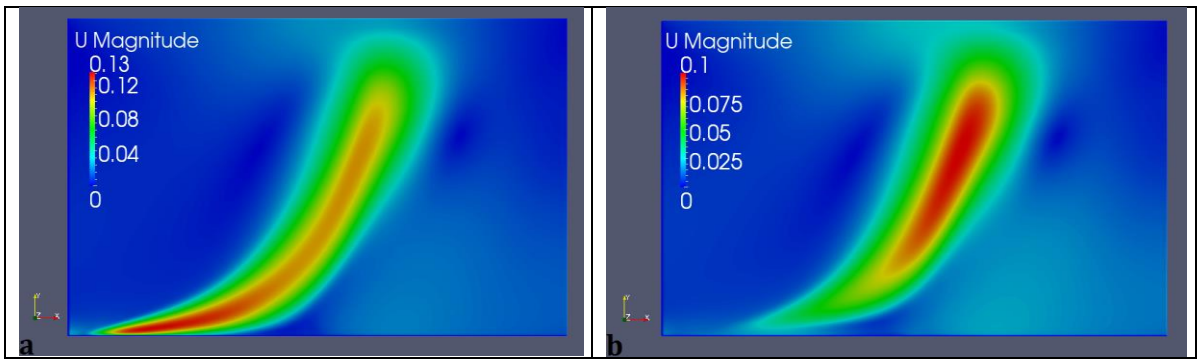

Figure 2.11. Velocity contour plots at two offset sections. (a) z/D = 1.818, (b) z/D = 3.636.

The current study investigated the temperature results from [23] further. The dilution contours for temperature at the plane of symmetry (z = 0) are plotted for realizable k-ε in Figure 2.12 for dilution rates of 12, 15, 20, 30, and 60. The innermost contour line reads a dilution of S = 12, and the outermost contour line corresponds to dilution of S = 60. Dilution would obviously increase with distance from the nozzle, and it depends on both discharge and receiving water properties (such as discharge diameter D, densimetric Froude number F_{rd}, and ambient water depth H_a, etc.). It was observed that the effect of distance (the path that the jet travels through) on the dilution factor was larger than the effect of the Froude number at the nozzle.

Temperature profiles (self-similar profiles) would behave the same (i.e., Gaussian shape) for various Froude numbers. Figure 2.13 presents the temperature Gaussian distribution at different

cross-sections for three different cases (i.e., three different Froude numbers), while bulked together. As shown, the temperature profiles, similar to the velocity profiles, seem to be independent of the Froude number.

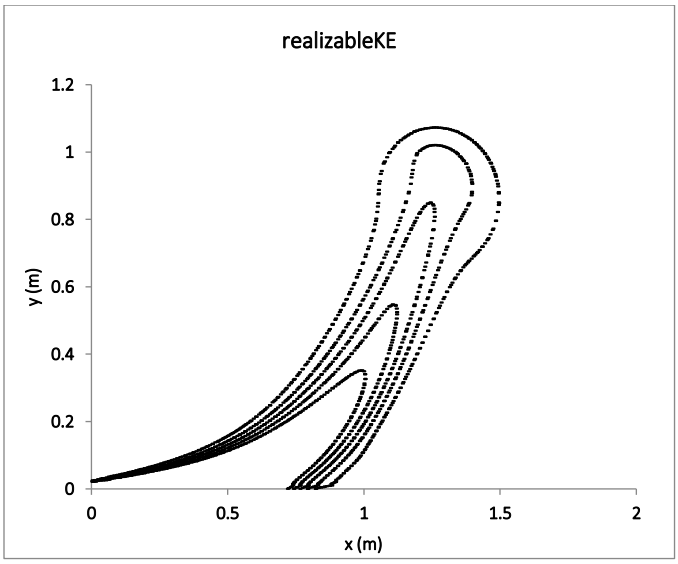

Figure 2.12. Temperature dilution contours at the plane of symmetry. Dilution rates are 12, 15, 20, 30, and 60 (realizable k-ε turbulence model).

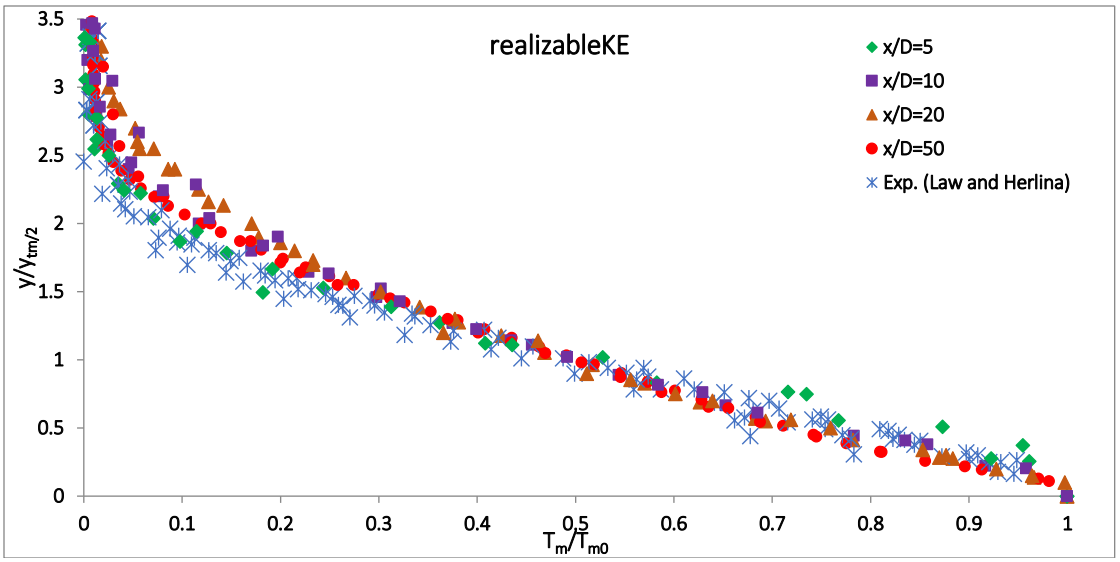

Figure 2.13. Stream-wise self-similarity temperature profiles for three cases at various cross-sections.

Ref. [64] used a sigma SGS eddy viscosity model to perform an LES model of turbulent horizontal buoyant and non-buoyant jets with several Reynolds (*Re*) and Richardson (*Ri*) numbers in stratified ambient water. Then, the effects of varying *Ri* (to characterize density differences) and *Re* (to characterize injection momentum) was studied. Turbulent production and

dissipation rates were found to be asymmetric in the mid-vertical plane but symmetric in the horizontal plane. Ref. [64]'s results on jet centerline velocity decay, mean velocity self-similarity, radial spread, and turbulent fluctuations were in good agreement with previous experimental results. Using the results from their LES model and looking at the instantaneous velocities in the jet studies, they realized that the jet close to the nozzle would behave the same as the developed jet farther from the discharge point in the stratified ambient water. They also identified the stable and unstable stratification regions and how the turbulent vortex rings and *Ri* are related to them.

Circular, square, and rectangular nozzles were considered in [65]'s CFD study of the effects of nozzle geometry on turbulent offset jet development in the near-field region. Turbulence models that were studied include the standard k-ε model [66], the realizable k-ε model [67], the Launder-Sharma k-ε model [68], and the Yang–Shih k-ε model [69]. The Yang–Shih k-ε turbulence model came out on top for predicting the jet properties in a comparison of these turbulence models (with a *Re* number of approximately 8,500) with previous experimental studies. Square-shaped offset jets seem to spread more in the wall normal and lateral directions and result in more efficient mixing with the surrounding fluid than circular offset jets. However, the maximum shear stress on the adjacent wall in the case of the square-shaped nozzle was slightly higher than that in the circular nozzle case.

Ref. [70] studied turbulent circular wall jets both experimentally and by the LES model; then, they compared those results with the numerical results from two RANS models: the standard k-ε and standard k-ω models, with enhanced wall functions. Then, [70] tested the grid convergence by the Grid Convergence Index (GCI), with low-resolution (0.9 million) followed by high-resolution (3.1 million) cells and ending with both the velocity and concentration properties of the jets. Ref. [70]'s results showed that LES is better than both RANS models for reproducing the scalar mixing and kinematic characteristics. Their LES results generally agreed better with the experimental data, although they did underpredict the span-wise velocity profiles away from the jet centerline. Vorticity distribution and turbulence intensities (u'/U, with u' being the root-mean-square of turbulent velocity fluctuations and U being the mean velocity) were also extracted and compared to the past experimental data, which showed a better agreement of the LES model rather than RANS models. In the region far from the centerline, the span-wise turbulence

intensity was observed to decrease faster, which was likely due to the inadequacy of the Smagorinsky SGS model for low-turbulence intensity situations in those regions. In the plane of symmetry, the *y*-direction (lateral—perpendicular to the plane of symmetry) vorticity, caused by wall presence, dominated the vorticity distribution. In the horizontal plane, the primary contributor was observed to be the *z*-direction (vertical—perpendicular to the horizontal plane) vorticity due to the jet-flow shear layer in the ambient water.

In the most recent study, [71] studied the offset buoyant jets with various properties for the discharges and ambient water, experimentally and numerically. Discharges were set to be both thermal and non-thermal, but positively buoyant all the time. The ambient water was stagnant, and they used a PIV system to collect the experimental data. All comparative experiments were conducted with the same densimetric Froude numbers (F_{rd}, ranging from 9.9 to 29.8) and density differences ($\Delta\rho$, ranging from 5.1 to 17.41). Three RANS turbulence models were adopted for their numerical study: standard k-ε, realizable k-ε, and buoyancy-modified k-ε. They concluded that the realizable k-ε model was more successful in predicting the discharge trajectories. The main finding of this study was that while using different combinations of parameters in discharge (salinity versus temperature) for keeping the same properties of the jet (the same values of F_{rd} and same $\Delta\rho$), the trajectory and mixing characteristics of the jets would be different in the same ambient water. Therefore, it is important not to only look at the relative buoyancy between discharge and ambient water, but also the properties of discharge such as salinity and temperature, which could be very important in the overall mixing efficiency of the jets.

2.6 Surface Discharges

Surface discharges of effluent into water bodies are less common due to lower mixing efficiency with the ambient water (i.e., the top portion of the jet/plume does not get ambient water entrainment especially close to the nozzle where the momentum effect is higher). This could be the reason that surface discharges have been less studied both experimentally and numerically. There is no CFD modeling of surface discharges to the best knowledge of the authors of this paper. The CORMIX3 empirical-based model was developed for surface discharge outfalls, which is not considered a CFD tool. This gap in the literature could be bridged with the following suggestions for both experimental and numerical modeling of surface discharges:

- Surface discharges using different channel geometries in calm ambient water
- Surface discharges using different channel geometries in co-flow ambient water
- Surface discharges using different channel geometries in cross-flow ambient water

2.7 Discharge Port Configuration

All of the cited publications above focused on the numerical modeling of single port outfalls. However, multiport diffusers are commonly used in ocean outfall designs due to their efficiency. The configuration of nozzles could be varied depending on the ambient condition and design considerations. Figure 2.14 shows five different configurations of multiport diffusers that are commonly used. Another emerging multiport diffuser configuration is the rosette outfall configuration, as shown in Figure 2.15. Similar to the surface discharges, multiport effluent discharges have been less studied, both experimentally and numerically.

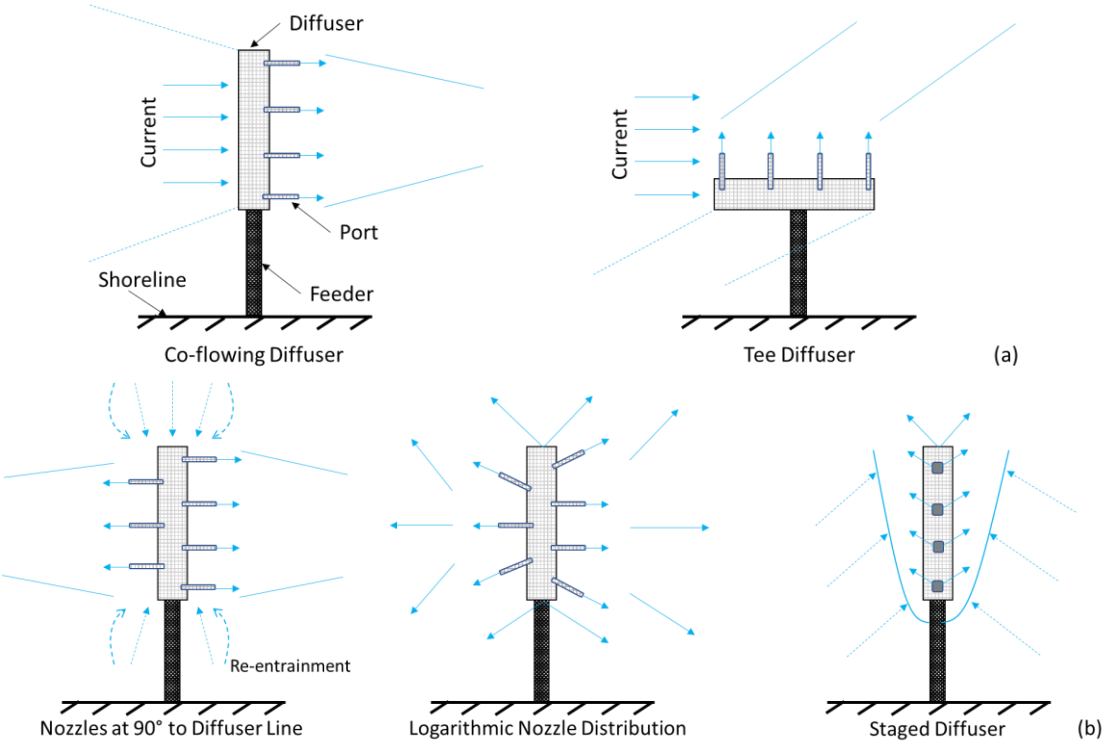

Figure 2.14. Multiport diffusers. (a) unidirectional diffusers with cross-flow, (b) alternating diffuser.

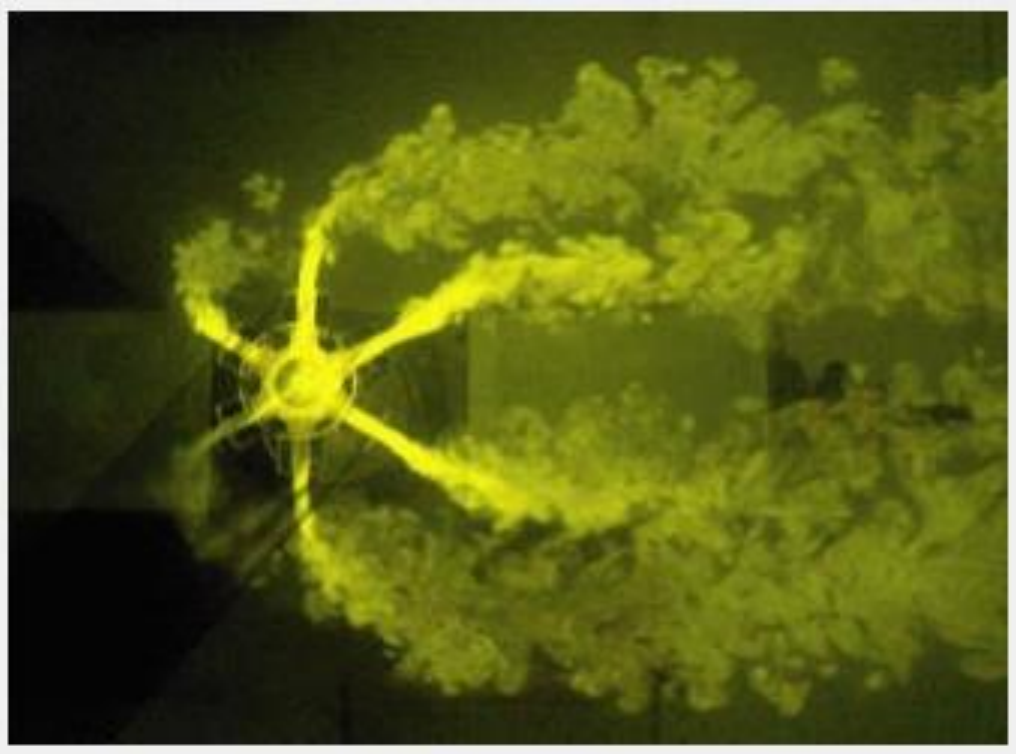

Figure 2.15. Rosette jet, top view (Source: Hong Kong University WATERMAN Educational Platform).

Ref. [72] studied a submerged multiport diffuser discharging thermal water into ambient water with co-flow conditions (similar configuration as shown in Figure 2.14a). They developed their own 3D model and used a numerical slot diffuser concept to implement the momentum discharge flux properly in the model. Thermal jet trajectory and temperature distribution along the trajectory were compared between their model and the experimental data. The qualitative comparison of the results showed a relatively good agreement between the numerical results and experimental data.

Very recently, [73] published a paper on 3D numerical simulations of rosette multiport diffusers using two RANS models: standard k-ε and RNG k-ε turbulence models. They used the popular OpenFOAM model for this study. They introduced an initial dilution region ($y < 5D$), and this is the region in which jets do not interact with each other after discharge and concentration is higher with a lower dilution rate. As the jets grow and travel toward the surface, their lateral widths increase, and they start interacting with each other. It was reported that for the regions around $y = 25D$, the concentration was reduced compared to the initial dilution region, and thus the dilution rate increased. As the jets traveled farther, their interaction with each other

increased (e.g., $y = 65D$). The RNG k-ε turbulence model performed better than the standard k-ε turbulence model when the numerical results were compared to the experimental data. As most of the terms in both turbulence models are the same (i.e., the same transport equations for k and ε), the difference in the results could be attributed to the improvements made in the RNG k-ε turbulence model as listed below:

- The RNG k-ε model accounts for the influence of the Reynolds number on the effective turbulence transport.
- The RNG k-ε model calculates the inverse effective Prandtl numbers, using a more advanced equation.
- The RNG k-ε model includes a new term in the ε transport equation that improves the calculation of the turbulent viscosity.

Ref. [73] also appreciated that the computational cost of using the RNG k-ε turbulence model is almost the same as that of standard k-ε turbulence model, while models such as LES and DNS will increase the computational cost dramatically.

Other than the above-mentioned studies, no CFD modeling study was found for the modeling of multiport diffusers. The main reason that the present available CFD models have not been applied to the modeling of multiport diffusers could be attributed to the difficulties in the mesh generation and stability of such models. However, it seems that with the work of [73], there will be more CFD modeling of such cases in the near future.

2.8 Critical Review and Future Research Needs

The above presented review and discussion outline the state-of-the-art knowledge on the CFD modeling of effluent discharge in the context of near-field mixing and dispersion. The cited literature above covers fundamental processes of discharge mixing modeling, which would help the efficient design of outfalls for engineering applications.

In advancing the numerical modeling of effluent discharges, special attention should be given to collecting reliable field data for real-sized projects in real project conditions. Coupling near-field and far-field models, which are the most practical in engineering projects, should be studied in more detail to investigate coupling techniques. Most of the CFD studies focused on fine-tuning small-scale parameters in the numerical schemes to calibrate their models, and little

attention was spent on the applicability of such models. This is specifically true when it comes to the practice of outfall designs, where wave and wind-induced currents have inevitable effects on jet mixing and dispersion in the near field. Now that the numerical models have shown an excellent performance in replicating the experimental cases, it is time to collect more field data to simulate the large-scale practical cases to further investigate the challenges in complex geometries, environmental forcing, and boundary conditions.

Additionally, there are a few jet configurations that have been studied less numerically or have not been studied at all. Although surface discharges are less popular due to poor dilution efficiency, there are several scenarios in which they are more suitable compared to inclined, submerged jets. Examples are available for the shallow places, or when the maintenance of submerged outfalls are more difficult compared to surface channels. Moreover, most of the previous numerical studies have focused on stagnant ambient water in their CFD models. More realistic ambient conditions with the presence of co-flow and cross-flow will advance the applicability of CFD models in effluent discharge problems. In reality, and especially for coastal outfalls, the discharge point is often laid on a steep bed, which will have a significant impact on the jet dispersion and run-out distance, especially beyond the impact point (i.e., when the density current on the bed is formed). Ref. [27] have studied the dilution characteristics of density currents built after the impact point of an inclined dense jet. However, their study was on a flat bed with no inclination. CFD models could be used to efficiently model these practical scenarios in more detail. The effect of bed roughness and vegetation could be critical for turbulent wall jets and/or density currents beyond the impact point.

Multiport and rosette diffusers could potentially increase the efficiency of the effluent discharges by increasing the number of jets discharging at the same time and multiplying the momentum-length scales before merging the jets. CFD modeling of complex multiport and rosette jet configurations would provide valuable insight into designing these jets in practice for professional engineers. Ambient stratification is another aspect that could be investigated using CFD models in more detail for both stagnant and non-stagnant ambient conditions.

2.9 Conclusions

Advances in computational resources and strength have led to an increase in CFD modeling of jet mixing and dispersion over the past two decades. Some jet configurations have received more attention than others due to various reasons. These reasons include but are not limited to easier compilation in numerical models, less complicated boundary conditions, simpler geometries for mesh generation, more practical efficiency in practice, and the availability of data. However, recent advances in experimental setups in jet studies (e.g., PIV and LIF systems), sampling techniques in field studies, and the availability of open-source CFD tools have opened the doors to more realistic CFD modeling in jet studies. Based on an extensive literature review of CFD modeling of effluent discharges in the near-field region, the following conclusions can be drawn:

- Numerically, the most studied effluent discharge configuration has been in inclined dense jets, due to their applicability in industry. Most studies focused on lab-size experiments to calibrate their models. Details on jet trajectories and dilution and velocity characteristics have been investigated and compared to experimental data. RANS and LES turbulence models are popular for such studies.
- Vertical jets are also popular in CFD studies, and the new trend in studying these jets involves considering the ambient conditions that may affect these jets such as lateral confinement and water shallowness, where the jet is attached to the top boundary. Cross-flow in vertical jets could have a significant influence in terms of the trajectory and dilution, both of which are getting more attention from researchers using CFD models.
- Horizontal jets could be either positively buoyant or negatively buoyant with attachment to the bed (i.e., wall jets) or elevated (i.e., offset jets). Single jets have been studied experimentally and numerically during the past years, and more attention is now given to interactions of multiple horizontal jets when they merge after a certain distance from the discharge point.
- Surface discharges have not been studied yet using a CFD approach, even though they are used in the industry and experimental data are available on such jets. This literature gap also exists for more complex jet configurations such as multiport and rosette diffusers.

- Previous studies have mainly focused on the stagnant ambient water due to the simplicity of internal and boundary conditions. However, to replicate real-life conditions more precisely, there is a need to move toward more complex ambient conditions to study the effects of wave, wind, co-flow and crossflow, density stratification, etc. on jet mixing and dispersion in CFD models.
- A wide range of turbulence models are available and have already been implemented in different CFD platforms that could be used for discharge mixing studies. Modifications of turbulence models, such as implementing the buoyancy terms, has been shown to be effective in improving the prediction of jet characteristics.

Mathematical Symbols

B_{gc}: Jet concentration *1/e* width
B_0: Jet buoyancy flux
C_a: Ambient water concentration
C_m: Jet centerline maximum concentration
C_0: Jet exit concentration
D or d: Nozzle diameter or diffusion coefficient
F_{rd}: Densimetric Froude number
G: Swirl number
g: Gravitational acceleration
g_0': Reduced gravitational acceleration
H_a: Ambient water depth
k: Turbulent kinetic energy
k_{eff}: Heat transfer coefficient
L: Cling length
L_M: Jet momentum-length scale
L_Q: Jet source-length scale
M_0: Jet kinematic momentum flux
P: Fluid pressure
Pr: Prandtl number
Pr_t: Turbulent Prandtl number
Q_0: Jet discharge volume flux
Re: Reynolds number
Ri: Richardson number
S: Dilution
s: Jet stream-wise distance
S_m: Jet centerline peak dilution
S_r: Jet dilution at return point
t: Time
T: Jet temperature at any location
T_a: Ambient water temperature
T_0: Jet exit temperature

U_m: Jet velocity component in the x-direction
U_{m0}: Jet centerline maximum velocity
U_0: Jet exit velocity
u: Mean velocity component in the x-direction
u_o: Inlet velocities of the offset jet
u_w: Inlet velocities of the wall jet
v: Mean velocity component in the y-direction
V_r: Velocity ratio
w: Mean velocity component in the z-direction
x_i: Horizontal location of impact
x_m: Jet centerline peak horizontal location
x_r: Jet return point
y_m: jet centerline peak vertical location
$y_{m/2}$: Jet velocity-half-height (the height of $U_m=U_{m0}/2$)
y_t: Terminal rise height

Greek Symbols

α: Jet entrainment constant
ε: Turbulent dissipation rate
θ: Angle of discharge
μ_t: Turbulent viscosity
ρa: Ambient water density
$\rho 0$: Jet exit density
υ: Kinematic viscosity
υ_t: Turbulent kinematic viscosity
υ_{eff}: Effective kinematic viscosity

References

1. Bleninger, T.; Jirka, G.H. Modelling and environmentally sound management of brine discharges from desalination plants. *Desalination* **2008**, *221*, 585–597.
2. Genthner, K. Research and Development in Desalination—Current Activities and Demand. Lecture Notes; DME Seminar: Berlin, Germany, 2005.
3. Bleninger, T.; Niepelt, A.; Jirka, G.H. Desalination plant discharge calculator. *Desalin. Water Treat.* **2010**, *13*, 156–173.
4. Lattemann, S.; Höpner, T. Environmental impact and impact assessment of seawater desalination. *Desalination* **2008**, *220*, 1–15.
5. Hopner, T.; Windelberg, J. Elements of environmental impact studies on costal desalination plants. *Desalination* **1996**, *108*, 11–18.
6. Robinson, D.; Wood, M.; Piggott, M.; Gorman, G. CFD modelling of marine discharge mixing and dispersion. *J. Appl. Water Eng. Res.* **2015**, *4*, 152–162.
7. Zhao, L.; Chen, Z.; Lee, K. Modelling the dispersion of wastewater discharges from offshore outfalls: A review. *Environ. Rev.* **2011**, *19*, 107–120.
8. Roberts, P.J.W.; Snyder, W.H.; Baumgartner, D.J. Ocean Outfalls. I: Submerged Wastefield Formation. *J. Hydraul. Eng.* **1989**, *115*, 1–25.
9. Roberts, P.J.W.; Snyder, W.H.; Baumgartner, D.J. Ocean Outfalls. II: Spatial Evolution of Submerged Wastefield. *J. Hydraul. Eng.* **1989**, *115*, 26–48.

10. Roberts, P.J.W.; Snyder, W.H.; Baumgartner, D.J. Ocean Outfalls. III: Effect of Diffuser Design on Submerged Wastefield. *J. Hydraul. Eng.* **1989**, *115*, 49–70.
11. Doneker, R.L.; Jirka, G.H. CORMIX User Manual: A Hydrodynamic Mixing Zone Model and Decision Support System for Pollutant Discharges into Surface Waters. EPA-823-K-07-001, 2007.
12. Morton, B.R.; Taylor, G.I.; Turner, J.S. Turbulent gravitational convection from maintained and instantaneous sources. *Proc. R. Soc. Lond. Ser. A Math. Phys. Sci.* **1956**, *234*, 1–23.
13. Fan, L.N. Turbulent Buoyant Jets into Stratified or Flowing Ambient Fluids. Ph.D. Thesis, California Institute of Technology, Pasadena, CA, USA, 1967.
14. Abraham, G. Jet Diffusion in Stagnant Ambient Fluid. Ph.D. Thesis, TU Delft, Delft, The Netherlands, 1963.
15. Turner, J.S. Buoyant Plumes and Thermals. *Annu. Rev. Fluid Mech.* **1969**, *1*, 29–44.
16. Wang, H.; Law, A.W.-K. Second-order integral model for a round turbulent buoyant jet. *J. Fluid Mech.* **2002**, *459*, 397–428.
17. Yannopoulos, P.C. An improved integral model for plane and round turbulent buoyant jets. *J. Fluid Mech.* **2006**, *547*, 267–296.
18. Jirka, G.H. Integral Model for Turbulent Buoyant Jets in Unbounded Stratified Flows. Part I: Single Round Jet. *Environ. Fluid Mech.* **2004**, *4*, 1–56.
19. Frick, W.E. Non-empirical closure of the plume equations. *Atmos. Environ.* **1984**, *18*, 653–662.
20. Kikkert, G.A.; Davidson, M.; Nokes, R.I. Inclined Negatively Buoyant Discharges. *J. Hydraul. Eng.* **2007**, *133*, 545–554.
21. Shao, D.; Law, A.W.K. Integral modelling of horizontal buoyant jets with asymmetrical cross sections. In Proceedings of the 7th International Symposium on Environmental Hydraulics; Singapore, 7–9 January, 2014.
22. Nash, J.D.; Jirka, G.H. Buoyant surface discharges into unsteady ambient flows. *Dyn. Atmos. Oceans* **1996**, *24*, 75–84.
23. Gildeh, H.K.; Mohammadian, A.; Nistor, I.; Qiblawey, H. Numerical Modeling of Turbulent Buoyant Wall Jets in Stationary Ambient Water. *J. Hydraul. Eng.* **2014**, *140*, 04014012.
24. Gildeh, H.K.; Mohammadian, A.; Nistor, I.; Qiblawey, H. Numerical modeling of 30° and 45° inclined dense turbulent jets in stationary ambient, Environ. *Fluid Mech.* **2015**, *15*, 537–562.
25. Gildeh, H.K.; Mohammadian, A.; Nistor, I.; Qiblawey, H.; Yan, X. CFD modeling and analysis of the behavior of 30° and 45° inclined dense jets—New numerical insights. *J. Appl. Water Eng. Res.* **2016**, *4*, 112–127.
26. Zhang, S.; Jiang, B.; Law, A.W.-K.; Zhao, B. Large eddy simulations of 45° inclined dense jets. *Environ. Fluid Mech.* **2016**, *16*, 101–121.
27. Zhang, S.; Law, A.W.K.; Jiang, M. Large eddy simulations of 45° and 60° inclined dense jets with bottom impact. *J. Hydro Environ. Res.* **2017**, *15*, 54–66.
28. Kolmogorov, A.N. The local structure of turbulence in incompressible viscous fluid for very large Reynolds number (in Russian). *Cr Acad. Sci. URSS* **1941**, *30*, 301–305.
29. Chen, X. A comparison of hydrostatic and nonhydrostatic pressure components in seiche oscillations. *Math. Comput. Model.* **2005**, *41*, 887–902.
30. Millero, F.J.; Poisson, A. International one-atmosphere equation of state of sea water. *J. Deep-Sea Res.* **1981**, *28*, 625–629.
31. Bemporad, G.A. Simulation of Round Buoyant Jet in Stratified Flowing Environment. *J. Hydraul. Eng.* **1994**, *120*, 529–543.
32. Vafeiadou, P.; Papakonstantis, I.; Christodoulou, G. Numerical simulation of inclined negatively buoyant jets. In Proceedings of the 9th International Conference on Environmental Science and Technology, Rhodes, Greece, 1–3 September 2005.

33. Bloomfield, L.J.; Kerr, R. Inclined turbulent fountains. *J. Fluid Mech.* **2002**, *451*, 283–294.
34. Roberts, P.J.W.; Ferrier, A.; Daviero, G. Mixing in Inclined Dense Jets. *J. Hydraul. Eng.* **1997**, *123*, 693–699.
35. Oliver, C.J.; Davidson, M.J.; Nokes, R.I. K-e Predictions of the initial mixing of desalination discharges. *Environ. Fuild Dyn.* **2008**, *8*, 617–625.
36. Gildeh, H.K. Numerical Modeling of Thermal/Saline Discharges in Coastal Waters. Master's Thesis, University of Ottawa, Ottawa, ON, Canada, 2013.
37. Nemlioglu, S.; Roberts, P.J. Experiments on Dense Jets Using Three-Dimensional Laser-Induced Fluorescence (3DLIF). In Proceedings of the 4th International Conference on Marine Waster Water Discharges & Coastal Environment (MWWD), Antalya, Turkey, 6–10 November 2006.
38. Cipollina, A.; Brucato, A.; Grisafi, F.; Nicosia, S. Bench scale investigation of inclined dense jets. *J. Hydraul. Eng*. **2005**, 131, 1017–1022.
39. Zeitoun, M.A.; McHilhenny, W.F.; Reid, R.O. Conceptual Designs of Outfall Systems for Desalination Plants; Research and Development Progress Report No. 550; Office of Saline Water, U.S. Department of the Interior: Washington, DC, USA, 1970.
40. Shao, D. Desalination Discharge in Shallow Coastal Waters. Ph.D. Thesis, Nanyang Technological University, Singapore, 2009.
41. Oliver, C.J.; Davidson, M.J.; Nokes, R.I. Behavior of Dense Discharges beyond the Return Point. *J. Hydraul. Eng.* **2013**, *139*, 1304–1308.
42. Papakonstantis, I.G.; Christodoulou, G.C.; Papanicolaou, P. Inclined negatively buoyant jets 1: Geometrical characteristics. *J. Hydraul. Res.* **2011**, *49*, 3–12.
43. Papakonstantis, I.G.; Christodoulou, G.C.; Papanicolaou, P. Inclined negatively buoyant jets 2: Concentration measurements. *J. Hydraul. Res.* **2011**, *49*, 13–22.
44. Germano, M.; Piomelli, U.; Moin, P.; Cabot, W.H. A dynamic subgrid-scale eddy viscosity model. *Phys. Fluids A: Fluid Dyn.* **1991**, *3*, 1760–1765.
45. Piggott, M.; Gorman, G.J.; Pain, C.C.; Allison, P.A.; Candy, A.S.; Martin, B.T.; Wells, M.R. A new computational framework for multi-scale ocean modelling based on adapting unstructured meshes. *Int. J. Numer. Methods Fluids* **2008**, *56*, 1003–1015.
46. Jiang, M.; Law, A.W.K. Mixing of swirling inclined dense jets—A numerical study. *J. Hydro-Environ. Res.* **2018**, *21*, 118–130.
47. Karimpour, F. Turbulence Modelling of Stably Stratified Wall-Bounded Flows. Ph.D. Thesis, Colorado State University, Fort Collins, CO, USA, 2014.
48. Gullbrand, J.; Chow, F. Investigation of numerical errors, subfilter-scale models, and subgrid-scale models in turbulent channel flow simulations. In *Proceedings of the Summer Program*; Center for Turbulence Research; NASA Ames/Stanford University, Stanford, CA, 2002; pp. 87–104.
49. Smagorinsky, J. General circulation experiments with the primitive equations. *Mon. Weather Rev.* **1963**, *91*, 99–152.
50. Dejoan, A.; Santiago, J.L.; Pinelli, A.; Martilli, A. Comparison between LES and RANS computations for the study of contaminant dispersion in the MUST field experiment. *Am. Meterol. Soc.* **2007**, submitted.
51. El-Amin, M.F.; Sun, S.; Heidemann, W.; Muller-Steinhagen. Analysis of a turbulent buoyant confined jet modeled using realizable k-ε model. *Heat Mass Transf.* **2010**, *46*, 943–960.
52. Shih, T.H.; Liou, W.W.; Shabbir, A.; Yang, Z.; Zhu, J. A new k–e eddy-viscosity model for high Reynolds number turbulent flows model development and validation. *Comput. Fluids* **1995**, *24*, 227–238.
53. Abou-Elhaggag, M.E.; Elgamal, M.; Farouk, M.I. Experimental and Numerical Investigation of Desalination Plant Outfalls in Limited Disposal Areas. *J. Environ. Prot.* **2011**, *2*, 828–839.

54. Yan, X.; Mohammadian, A. Numerical Modeling of Vertical Buoyant Jets Subjected to Lateral Confinement. *J. Hydraul. Eng.* **2017**, *143*, 04017016.
55. Lee, A.W.-T.; Lee, J.H.-W. Effect of Lateral Confinement on Initial Dilution of Vertical Round Buoyant Jet. *J. Hydraul. Eng.* **1998**, *124*, 263–279.
56. Chen, C.J.; Rodi, W. *A Review of Experimental Data of Vertical Turbulent Buoyant Jets*; Pergamon Press: Tarrytown, NY, USA, 1980.
57. Yan, X.; Ghodoosipour, B.; Mohammadian, A. Three-dimensional numerical study of multiple vertical buoyant jets in stationary ambient water. *J. Hydraul. Eng.* **2020,** DOI: 10.1061/(ASCE)HY.1943-7900.0001768.
58. Huai, W.; Li, Z.-W.; Qian, Z.-D.; Zeng, Y.-H.; Han, J.; Peng, W.-Q. Numerical Simulation of Horizontal Buoyant Wall Jet. *J. Hydrodyn.* **2010**, *22*, 58–65.
59. Sharp, J.J. The use of a buoyant wall jet to improve the dilution of a submerged outfall. *Proc. Inst. Civ. Eng.* **1975**, *59*, 527–534.
60. Verhoff, A. *The Two-Dimensional Turbulent Wall Jet with and Without an External Stream*; Rep. No. 626; Princeton University, Princeton, NJ, USA, 1963.
61. Li, Z.-W.; Huai, W.; Han, J. Large Eddy Simulation of the Interaction between Wall Jet and Offset Jet. *J. Hydrodyn.* **2011**, *23*, 544–553.
62. Sharp, J.J.; Vyas, B.D. The buoyant wall jet. *Proc. Inst. Civ. Eng. Part 2 Res. Theory* **1977**, 63(3), 593-611.
63. Law, A.W.-K.; Herlina, H. An Experimental Study on Turbulent Circular Wall Jets. *J. Hydraul. Eng.* **2002**, *128*, 161–174.
64. Ghaisas, N.S.; Shetty, D.A.; Frankel, S.H. Large eddy simulation of turbulent horizontal buoyant jets. *J. Turbul.* **2015**, *16*, 772–808.
65. Mohammadaliha, N.; Afshin, H.; Farhanieh, B. Numerical Investigation of Nozzle Geometry Effect on Turbulent 3-D Water Offset Jet Flows. *J. Appl. Fluid Mech.* **2016**, *9*, 2083–2095.
66. Launder, B.; Spalding, D. The numerical computation of turbulent flows. *Comput. Methods Appl. Mech. Eng.* **1974**, *3*, 269–289.
67. Shih, T.-H.; Zhu, J.; Lumley, J.L. A new Reynolds stress algebraic equation model. *Comput. Methods Appl. Mech. Eng.* **1995**, *125*, 287–302.
68. Launder, B.E.; Sharma, B.I. Application of the energy-dissipation model of turbulence to the calculation of flow near a spinning disc. *Lett. Heat Mass Transf.* **1974**, *1*, 131–137.
69. Yang, Z.; Shih, T.H. New time scale based k-ε model for near-wall turbulence. *AIAA J.* **1993**, *31*, 1191–1198.
70. Zhang, S.; Law, A.W.-K.; Zhao, B. Large eddy simulations of turbulent circular wall jets. *Int. J. Heat Mass Transf.* **2015**, *80*, 72–84.
71. Alfaifi, H.; Mohammadian, A.; Gildeh, H.K.; Gharavi, A. Experimental and numerical study of the characteristics of thermal and nonthermal offset buoyant jets discharged into stagnant water. *Desalin. Water Treat.* **2019**, *141*, 171–186.
72. Geun, K.D.; Won, S.I. Modeling the mixing of heated water discharged from a submerged multiport diffuser. *J. Hydraul. Res.* **2000**, *38*, 259–270.
73. Yan, X.; Mohammadian, A.; Chen, X. Three-Dimensional Numerical Simulations of Buoyant Jets Discharged from a Rosette-Type Multiport Diffuser. *J. Mar. Sci. Eng.* **2019**, *7*, 409.

3 Mixing of Inclined Dense Jets: A Numerical Modeling[2]

Abstract: Numerical modeling of inclined turbulent dense jets discharging into a calm homogeneous environment has been investigated in this paper. The jets are discharged at four angles: 60°,75°, 80° and 85°. The higher inclinations are more suitable for deep water outfalls where terminal rise height of the jet does not attach to the ambient water surface. Such jets, especially 60° jets, are used frequently to discharge industrial effluents. The numerical model (OpenFOAM) used in this study is based on the Finite Volume Method (FVM) applying LRR turbulence model closure. Two different densimetric Froude numbers were simulated for each discharge angle and important geometrical characteristics of the jet trajectory are investigated, i.e., the initial terminal rise height reached by the jet at flow initiation, the final terminal rise height at the steady state, and the point where the jet returns to the nozzle height. Concentration properties of these jets are also characterised numerically, i.e., the dilution at the main geometrical points of the jet. All the results are presented in the dimensionless forms in order to compare them to the previous experimental studies.

Keywords: Mixing; Outfall; Dilution; Velocity; Desalination; Dense jets; Turbulence

---

[2] This chapter of the study has been published as: Kheirkhah Gildeh, H., Mohammadian, A., Nistor, I. (2020). "Mixing of Inclined Dense Jets: A Numerical Modelling", Water Engineering Modelling and Mathematic Tools, Elsevier, https://doi.org/10.1016/B978-0-12-820644-7.00023-2.

3.1 Introduction

Disposal of wastewater with higher density than ambient water is a common phenomenon all over the world. Examples are the brine discharges from desalination plants and cooling water discharges from Liquefied Natural Gas (LNG) plants, which can be seen in the Middle Eastern countries. The former has a beneficial effect on the environment by decreasing exploitation of non-renewable water resources. However, at the same time it may cause negative local impacts on the environment (Bleninger and Jirka, 2008). The main issue is the marine environment, especially the shoreline (Einav, 2003). Seawater desalination plants discharge a large volume of concentrated salt brine into the coastal waters (Figure 3.1). There are other effluent discharges such as chemical wastes from biofouling (e.g. chlorine), and other substances that may result from fertilizers. Depending on both the discharge facility and ecological characteristics of the receiving water, those wastewaters can have a harmful impact on the local environment. For instance, areas such as coral reefs, mangrove forests, salt marshes, and generally low energy intertidal areas are very vulnerable (Hopner and Windelberg, 1996). Marine regions similar to the Persian Gulf and Red Sea have low water exchange capacities and are less energetic; consequently, they are more sensitive to desalination plant discharges. Environmental impacts of effluent discharge into coastal waters may affect local fisheries potential, the tourism industry, and have other economic consequences. Genthner (2005) noted that recently, public and scientific concerns have increased regarding the environmental impacts of desalination plants. Therefore, the mixing and dispersion mechanism of effluent discharges into ambient water has been focused on by many researchers, and this will be briefly reviewed.

Figure 3.1: Al-Ghubrah desalination plant (largest in Oman) with a surface discharge (photo: H.H. Al-Barwani)

Earlier studies on dense jet flows have had the tendency to focus on vertical jets (e.g. Turner 1966; Abraham 1967; McLellan and Randal 1986; Baines et al. 1990; Zhang and Baddour 1998). The vertical dense jets, which are usually called fountains, are different from most inclined dense jets, because in a calm environment, vertical dense jets fall back onto themselves. Thus, it is preferable to elongate the trajectory and increase the consequent entrainment. Zeitoun et al. (1972) investigated more typical inclined discharges (with no re-entrainment) and concluded that 60° was the preferred discharge angle because of the relatively higher dilution that they obtained from the experimental measurements. According to their study, other researchers focused more on the 60° inclined dense jets, which had more practical applications as well (e.g. Roberts and Toms 1997; Roberts et al. 1997). Roberts and Toms (1997) studied effluent discharges into ambient water with current. This configuration of dense jet and ambient water has also been investigated by Pincince and List (1973). The latter compared their experimental results with an integral model solution and discovered that the model was able to predict flow trajectories with reasonable accuracy, although the dilution values were underestimated.

Later, Cipolina et al. (2005), extended the dense jet studies in still ambient water to investigate flow behavior at different inclinations, 30°, 45°, and 60°. Their study mainly focused on the key geometrical properties of the inclined dense jets such as maximum height and point of impact. However, their study did not report any dilution measurements and only focused on the image

processing of the jet trajectory. Kikkert et al. (2007) developed an analytical method to predict the behavior of inclined dense discharges and compared the results to their own experiments as well as other previous studies. They studied the inclined jets up to 75° from horizontal. The integrated dilution values from their study showed that the normalized dilution at terminal rise height is about the same for angles between 30° and 60°. This result is different from the earlier study by Zeitoun et al. (1970), but is supported by predictions of the CORJET model (Jirka 2004, 2006), which shows that the dilution value is almost the same at the terminal rise height of jets with inclination from 30° to 45°, with a higher value for 45° jets. This conclusion was made earlier by Cederwall (1968) in the stationary ambient water.

Shao and Law (2010) conducted experiments on lower angles, 30° and 45° jets, using a combined Planar Laser Induced Fluorescent (PLIF) and Particle Image Velocimetry (PIV) method. They divided the experiments into two series: series F, in which the nozzle is placed far from the boundary (seabed), and series N, for cases close to the bottom boundary. The Coanda effect (see e.g. Shao and Law (2010)) was also investigated in their study. Papakonstantis et al. (2011a) measured the trajectory characteristics of dense jets with θ_0=45° to 90° visually. The turbulent concentration fluctuation (C_{rms}) measurements across a dense jet have also been studied for jet angles θ_0=45°, 60° and 75° (Papakonstantis et al. (2011b)). Lai and Lee (2012) reported a comprehensive experimental investigation of the tracer concentration field of inclined dense jets for jet densimetric Froude numbers of F_0=10 to 40 and a broad range of θ_0=15° to 60°. Empirical correlation of the terminal rise height, impact point and their dilution as a function of jet discharge angle were compared with of VISJET model prediction (Lee and Chu (2003)) as well as others in their study. Schreiner et al. (2018) used acoustic Doppler velocimeter (ADV) to study the trajectory of a jet in crossflow in a channel bend. They proposed a modified formula for the jet trajectory in the bend section. More recently, Alfaifi et al. (2019) performed an experimental and empirical study of geometrical characteristics of 15° and 52° inclined negatively buoyant jets in stagnant water.

All the above-mentioned studies are experimental. However, numerical modelling of dense jets has been started more recently, and hence requires more investigation and development. Kim et al. (2002) investigated the mixing processes of a buoyant jet discharged from a submerged

single port using a three-dimensional hybrid model. In the proposed hybrid model, the initial mixing was simulated by a jet integral method, and the advection-diffusion process was simulated using a particle tracking method. The proposed model was verified by their laboratory experiments, which were conducted for various conditions. Vafeiadou et al. (2005) studied inclined negatively buoyant jets numerically using a three-dimensional model (CFX-5). For turbulence closure, the SST (Shear Stress Transport) model was employed, which is based on a blending between the k-ε and k-ω models. They used an unstructured grid with refinement near the bottom, where the boundary layer develops, and around the inflow nozzle. They concluded that the model underestimated slightly the terminal rise height and underestimated considerably the return point compared to experimental data by Roberts et al. (1997). Kim and Cho (2006) investigated buoyant flow of heated water discharged from surface and submerged side outfalls in shallow and deep water with a cross flow. They used FLOW-3D, which is a commercial CFD package, and the RNG k-ε model was applied for turbulence closure. Oliver et al. (2008) investigated the geometrical and mixing characteristics of inclined dense jets using the CFX model. They used the standard k-ε turbulence model as well as the one they calibrated through adjustment of the turbulent Schmidt number in the tracer transport equation. Elhaggag et al. (2011) studied dense brine jets both experimentally and numerically. However, they focused only on the vertical dense jets, and no inclination is reported in their investigation. The numerical simulations were conducted via a FLUENT CFD package and were compared to those from their experimental study. More recently, with the emergence of open source CFD tools, OpenFOAM in particular, more robust numerical models have been developed for inclined dense jets. Kheirkhah Gildeh et al. (2013, 2014a, 2014b, 2015) investigated a broad range of Reynolds-averaged Navier Stokes (RANS) turbulence models in their CFD models. They studied the turbulent wall jet and inclined dense jets for 30° and 45°, but no other inclination. They concluded that realizable k-ε and LRR turbulence models are the most robust models in RANS for jet mixing problems. Based on their recommendations, Alfaifi et al. (2018) selected standard k-ε and realizable k-ε turbulence models in their study of thermal and non-thermal offset buoyant jets in stagnant water and confirmed the capability of the realizable k-ε model in replicating the jet centerline trajectory when compared to their experimental data. Jiang et al. (2019) and their

research team (Jiang and Law, 2018; Zhang et al., 2017) adopted an OpenFOAM model after its capability was shown by Kheirkhah Gildeh et al. (2013, 2014a, 2014b, 2015) for mixing problems, and used Large Eddy Simulations (LES) with the Dynamic Smagorinsky sub-grid model to investigate the turbulence characteristics of 45° inclined dense jets. They found that the model could reproduce the mixing characteristics of a 45° jet in their experiment; however, the simulated transitional spectra towards the inertial sub-range decayed substantially faster than the experiments. They attributed this discrepancy to their grid sizes. Yan and Mohammadian (2017) used OpenFOAM to investigate the vertical buoyant jets subjected to lateral confinement. They used the standard k-ε and buoyancy-modified k-ε turbulence models for their simulations. They have calibrated their model using Prandtl (Pr) and turbulent Prandtl (Pr_t) numbers. Genetic Algorithm (GA) has recently being used in the jet mixing problems for both vertical and inclined discharges (Bonakdari and Mohammadian, 2019; Yan and Mohammadian, 2019) to characterize the geometrical and dilution properties of the jets.

None of the previously mentioned CFD studies investigated the trajectory and concentration characteristics of dense jets with inclinations between 45° and 90°. Therefore, numerical analysis of mixing behaviour of inclined dense jets with θ_0=60°, 75°, 80° and 85° is needed to better understand jet characteristics for such configurations, and to quantify the numerical analysis in such jets that are relevant for the coastal regions discharging effluents in deeper waters. A 60° jet has been chosen based on its large practical use in ocean outfall systems. Moreover, as Bloomfield and Kerr (2002) reported in their experimental study, the maximum final terminal rise height is achieved for θ_0=80°. Therefore, it is important to investigate other inclinations, especially the ones closer to the vertical direction that have been studied less than other configurations. This will help to understand the key features of inclined dense jets for higher angles from horizontal. Based on Kheirkhah Gildeh et al. (2013, 2014a, 2014b, 2015), realizable k-ε and LRR turbulence models performed the best amongst other RANS turbulence models to predict the jet characteristics. LRR model has been adopted to conduct the numerical tests in this study as this model has been rarely studied before for mixing problems.

The structure of this paper for the next sections is as follows. Section 3.2 reviews theoretical concepts of jet mixing in the near-field region. Section 3.3 presents the governing equations of the

numerical model. Section 3.4 presents numerical results and comparison of the results to those from experiments. Finally, concluding remarks complete the study.

3.2 Theoretical Concepts

The side view of a dense buoyant jet discharging into a receiving water body is shown in Figure 3.2. The discharge properties are the nozzle diameter D, its height above bottom h_0, and the jet initial inclination θ_0 above horizontal and pointing offshore. The ambient water condition is unstratified with a constant density ρ_a and stagnant. The discharge velocity is U_0 and its density is ρ_0 ($\rho_0 > \rho_a$). Therefore, the following flux variables can be written, the volume flux (discharge) Q_0, momentum flux M_0, and Buoyancy flux B_0. These parameters are defined as (Fischer et al. 1979):

$$Q_0 = \frac{\pi D^2}{4} U_0 \tag{3.1}$$

$$M_0 = U_0 Q_0 \tag{3.2}$$

$$B_0 = g_0' Q_0 \tag{3.3}$$

in which $g_0' = g|\rho_0 - \rho_a|/\rho_a$ is the buoyant gravitational acceleration at the source.

The turbulent jet that resulted from a high velocity condition rises up to a maximum height named the terminal rise height and then falls downward due to negative buoyancy of the jet until it impacts the bed. Then, a density current is formed and propagated downstream of the impact point.

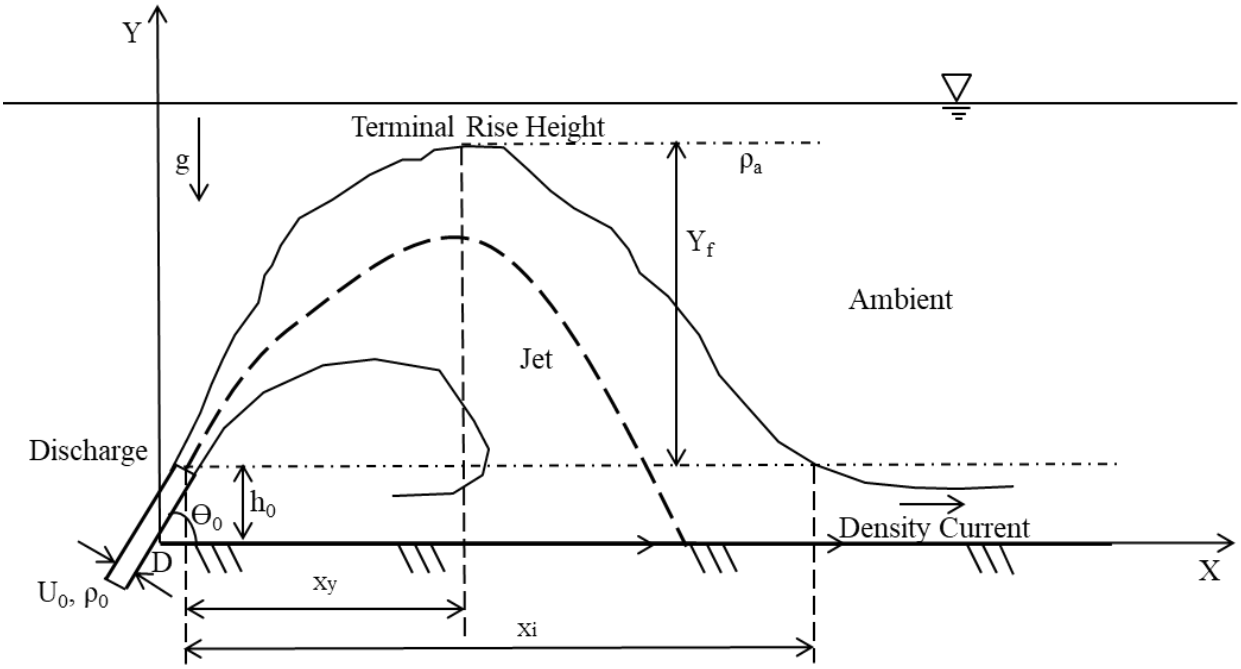

Figure 3.2: Schematic view of an inclined dense jet in stagnant ambient water

The geometrical and mixing properties of the turbulent dense jets can be characterized by two length scales, the discharge length scale L_Q and the momentum length scale L_M as (Wright 1977; Jirka and Doneker 1991):

$$L_Q = \frac{Q_0}{M_0^{1/2}} \tag{3.4}$$

$$L_M = \frac{M_0^{3/4}}{B_0^{1/2}} \tag{3.5}$$

A related non-dimensional parameter is the densimetric Froude number F_0 and is defined as:

$$F_0 = \frac{U_0}{\sqrt{g_0' D}} \tag{3.6}$$

This parameter is proportional to the length scales ratio as $\frac{L_M}{L_Q} = (\pi/4)^{-1/4} F_0$. For the high Froude number discharges, $F_0 >> 1$ or $L_M/L_Q >> 1$ (momentum-driven flow), the effect of initial volume flux becomes unimportant (Jirka, 2004). Moreover, Zhang and Baddour (1998) showed that the dilution at the maximum level of a vertical dense jet becomes independent of the Froude number when $F_0 \geq 10$. Therefore, for a specific angle θ_0, dimensional analysis leads to the following expression for any length parameter such as the rise height Y, and for dilution S at any location (X, Y) of the central plane $Z=0$ (Turner 1966, Roberts et al. 1997):

$$\frac{Y}{L_M} = Constant \quad \text{or} \quad \frac{Y}{DF_0} = Constant \tag{3.7}$$

$$S\frac{L_Q}{L_M} = f\left(\frac{X}{L_M}, \frac{Y}{L_M}\right) \quad \text{or} \quad \frac{S}{F_0} = f\left(\frac{X}{DF_0}, \frac{Y}{DF_0}\right) \tag{3.8}$$

The jet reaches an initial maximum height (initial terminal rise height) Y_i. Then, the flow reaches a steady state and the terminal rise height is reduced to a final value Yf. This height appears at a horizontal distance X_y from the source, whereas X_i denotes the horizontal distance from the source to the outer jet boundary at the nozzle elevation. Therefore, the following constants are obtained for trajectory characteristics of a dense jet:

$$\frac{Y_i}{DF_0} = C_1(\theta_0) \tag{3.9}$$

$$\frac{Y_f}{DF_0} = C_2(\theta_0) \tag{3.10}$$

$$\frac{X_y}{DF_0} = C_3(\theta_0) \tag{3.11}$$

$$\frac{X_i}{DF_0} = C_4(\theta_0) \tag{3.12}$$

For a certain point on the jet axis plane with dimensionless coordinates (X/DF_0, Y/DF_0), Eqn. (3.8) can be written as (Zeitoun et al. 1970; Pincince and List 1973):

$$\frac{S}{F_0} = Constant \tag{3.13}$$

The time-averaged dilution at a point is the ratio of the initial concentration C_0 to the local mean concentration C_M (Papakonstantis et al. (2011b)). For a point on the jet central plane at a specific position X, for instance, at location X_y of the terminal rise height (X_y/DF_0=constant), Eqn. (3.8) reads:

$$\frac{C_0}{C_M}\frac{1}{F_0} = f\left(\frac{Y}{DF_0}\right) \tag{3.14}$$

Where Y is the vertical coordinate of the point where C_M is obtained. Similarly, this equation can be written for Y_c, jet centerline rise height at the location of X_y, (Y_c/DF_0=constant):

$$\frac{C_M}{C_{Mc}} = f\left(\frac{Y}{DF_0}\right) \tag{3.15}$$

3.3 Numerical Model

3.3.1 Numerical Model Framework

The open-source CFD software platform OpenFOAM was used in this study. OpenFOAM uses the finite-volume discretization approach for fluid flow applications. A transient solver for

incompressible fluid within OpenFOAM - pisoFoam - has been modified and used. For the current paper, the standard pisoFoam solver has been extended in the following way:

- Addition of salinity and temperature fields and associated transport equations;
- Addition of the Boussinesq term to the momentum equations; and
- Addition of an equation of state that calculates the density of seawater as a function of salinity and temperature (Millero and Poisson, 1981).

The governing equations are the RANS equations with a Boussinesq assumption for buoyancy effects and a Boussinesq hypothesis for modelling the Reynolds stresses for three-dimensional, incompressible fluids, as follows:

Continuity equation:

$$\frac{\partial u}{\partial x}+\frac{\partial v}{\partial y}+\frac{\partial w}{\partial z}=0 \tag{3.16}$$

Momentum equations:

$$\frac{\partial u}{\partial t}+u\frac{\partial u}{\partial x}+v\frac{\partial u}{\partial y}+w\frac{\partial u}{\partial z}=-\frac{1}{\rho_0}\frac{\partial P}{\partial x}+\frac{\partial}{\partial x}\left(\upsilon_{eff}\left(\frac{\partial u}{\partial x}\right)\right)+\frac{\partial}{\partial y}\left(\upsilon_{eff}\left(\frac{\partial u}{\partial y}\right)\right)+\frac{\partial}{\partial z}\left(\upsilon_{eff}\left(\frac{\partial u}{\partial z}\right)\right) \tag{3.17}$$

$$\frac{\partial v}{\partial t}+u\frac{\partial v}{\partial x}+v\frac{\partial v}{\partial y}+w\frac{\partial v}{\partial z}=-\frac{1}{\rho_0}\frac{\partial P}{\partial y}+\frac{\partial}{\partial x}\left(\upsilon_{eff}\left(\frac{\partial v}{\partial x}\right)\right)+\frac{\partial}{\partial y}\left(\upsilon_{eff}\left(\frac{\partial v}{\partial y}\right)\right)+\frac{\partial}{\partial z}\left(\upsilon_{eff}\left(\frac{\partial v}{\partial z}\right)\right)-g\frac{\rho-\rho_0}{\rho_0} \tag{3.18}$$

$$\frac{\partial w}{\partial t}+u\frac{\partial w}{\partial x}+v\frac{\partial w}{\partial y}+w\frac{\partial w}{\partial z}=-\frac{1}{\rho_0}\frac{\partial P}{\partial z}+\frac{\partial}{\partial x}\left(\upsilon_{eff}\left(\frac{\partial w}{\partial x}\right)\right)+\frac{\partial}{\partial y}\left(\upsilon_{eff}\left(\frac{\partial w}{\partial y}\right)\right)+\frac{\partial}{\partial z}\left(\upsilon_{eff}\left(\frac{\partial w}{\partial z}\right)\right) \tag{3.19}$$

where u, v, and w are the mean velocity components in the x, y, and z directions, respectively, t is the time, P is the mean fluid pressure, υ_{eff} represents the effective kinematic viscosity ($\upsilon_{eff}=\upsilon_t+\upsilon$), υ_t is the turbulent kinematic viscosity, υ is the kinematic viscosity, g is the gravity acceleration, ρ is the fluid density, and ρ_0 is the reference fluid density.

One should note that the current approach invokes the Boussinesq assumption for handling the buoyancy effects, which allows the solution of the simplified incompressible RANS equations to be obtained by neglecting the density variation, except for the buoyancy term in the momentum equation in the vertical direction (y-coordinate).

The time-history of the concentration and temperature are modelled using the advection-diffusion equation, as:

$$\frac{\partial C}{\partial t} + u\frac{\partial C}{\partial x} + v\frac{\partial C}{\partial y} + w\frac{\partial C}{\partial z} = D\left(\frac{\partial^2 C}{\partial x^2} + \frac{\partial^2 C}{\partial y^2} + \frac{\partial^2 C}{\partial z^2}\right) \tag{3.20}$$

$$\frac{\partial T}{\partial t} + u\frac{\partial T}{\partial x} + v\frac{\partial T}{\partial y} + w\frac{\partial T}{\partial z} = k_{eff}\left(\frac{\partial^2 T}{\partial x^2} + \frac{\partial^2 T}{\partial y^2} + \frac{\partial^2 T}{\partial z^2}\right) \tag{3.21}$$

with

$$k_{eff} = \frac{\upsilon_t}{Pr_t} + \frac{\upsilon}{Pr} \tag{3.22}$$

where C is the fluid concentration (salinity), D is the diffusion coefficient, T is the fluid temperature, k_{eff} is the heat transfer coefficient, Pr is the Prandtl number, and Pr_t is the turbulent Prandtl number. The turbulent Prandtl number was changed within the conventional range of 0.6-1, and it was numerically found that the results were not sensitive to this parameter within this range.

3.3.2 Numerical Solution

The pisoFoam solver is a transient solver for incompressible flow. The code first predicts the velocity field by solving the momentum equations. Pressure is then found by solving the Poisson equation in the Issa's PISO (Pressure-Implicit with Splitting of Operators) algorithm via an iterative process. Rather than solving all the coupled equations in a coupled or iterative sequential fashion, PISO splits the operators into an implicit predictor and multiple explicit corrector steps. At each time step, velocity and temperature are predicted, and then pressure and velocity are corrected. The velocity is predicted implicitly because of the greater stability of implicit methods, which means that a set of coupled linear equations, expressed in matrix-vector form as $Ax=b$, are solved. More information about Issa's PISO algorithm can be found in references (e.g., Issa, 1986). The advection and diffusion equations are then solved using the finite volume method.

The temporal term has been discretized by a first order, implicit Euler scheme. The advection and diffusion terms are discretized by the standard finite volume method using Gaussian integration with a linear interpolation scheme for calculating values at face centres from cell centres.

For the pressure field, the PCG (Preconditioned Conjugate Gradient) method is used to solve the linear system. The PBiCG (Preconditioned Bio Conjugate Gradient) method has been used for

other fields, U, T, k, and ε. In order to enhance the rate of convergence for iterative solvers, the DIC (Diagonal Incomplete Cholesky) pre-conditioner is used to calculate the pressure field. This is a simplified diagonal-based pre-conditioner for symmetric matrices. The DILU (Diagonal Incomplete LU) pre-conditioner is used for the other fields, U, T, k, and ε, which mostly include asymmetric matrices to be solved.

3.3.3 Domain and Boundary Conditions

Due to the transversal symmetry of the flow problem, only half of the domain was included in the computational domain as illustrated in Figure 3.3. It is noteworthy that vortex shedding is not resolved by RANS equations within the range of parameters considered in this paper and therefore the symmetry assumption is justified. The nozzle has been placed far enough from the bed and left wall to avoid any interaction with the walls. Otherwise, bed effects such as the Coanda effect may decrease the dilution rate since the water entrainment toward the jet centreline would be reduced. The dimensions of the computational domain are selected based on those of the experimental setup. The numerical simulations were performed in a computational domain corresponding to the physical tank with dimensions of 2 m length, 0.5 m width, and 1.0 m depth (Figure 3.3a). A refined mesh system, especially close to the nozzle and the bed boundary (Figure 3.3b), is used for simulations to better capture velocity and concentration characteristics in the near-field zone. As part of a mesh sensitivity analysis, more than 20 initial test runs were performed to ensure that the mesh was sufficiently refined to resolve the velocity and concentration gradients, especially close to the nozzle. The grid refinement criterion was set to reach a difference of less than 3% between the predicted results when using the last two grids. When this criterion was reached, it was assumed that a satisfactory mesh was established, and no further refinement was needed.

For the inlet (nozzle), the boundary conditions are: $u=U_0\times cos(\theta)$, $v=U_0\times sin(\theta)$, $w=0$, $C=C_0$, $T=T_0$, $k=0.06u^2$, and $\varepsilon=0.06u^3/D$. The inlet values for k and ε are chosen based on Huai et al. (2010). Regarding the flow at the outlet section, a zero-gradient boundary condition perpendicular to the outlet plane was defined for u, v, k, ε, C, T and P. Moreover, for the wall boundaries, the standard wall functions were used for U, k, and ε, and the no-slip condition is considered. Finally, the symmetry boundary was included in the model using zero-gradient conditions. In fact, the

symmetry boundary condition implies zero normal velocity and zero normal gradient of all variables at the symmetry plane, and vortex shedding effects were not resolved.

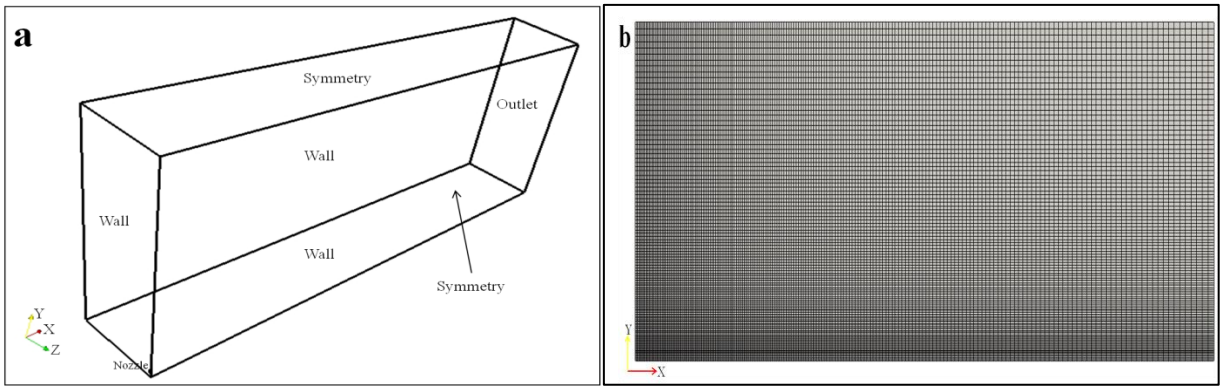

Figure 3.3: Computational domain. (a) domain dimensions and boundary conditions of the numerical model (b) the refined mesh system used in this study (view of the X-Y plane)

3.4 Numerical Results and Discussion

Eight different cases for the 60°, 75°, 80° and 85° inclined dense jets have been numerically simulated (i.e. four angles by two densimetric Froude numbers). The comparative results are further presented in graphs and tables. For some graph comparisons, and for the sake of simplicity, the numerical results are compared only to Papakonstantis et al. (2011a, 2011b) experimental data. However, the numerical results for constants described above will be compared to other studies in the tables. The characteristics of the eight cases are summarized in Table 3.1.

Table 3.1: Parameters of numerical simulations

Case #	Inclined Angle θ_0	Inlet Diameter D (mm)	Initial Inlet Height Y_0 (mm)	$\Delta\rho/\rho_a$ (%)	Densimetric Froude # Fr_0
1	60	6	11	2.6	19
2	60	6	11	2.6	27
3	75	6	11	2.6	19
4	75	6	11	2.6	27
5	80	6	11	2.6	19
6	80	6	11	2.6	27
7	85	6	11	2.6	19
8	85	6	11	2.6	27

3.4.1 Geometrical Characteristics

terminal rise height

The initial and final terminal rise heights normalized by the jet diameter D for each discharge angle is plotted against F_0 in Figure 3.4. The numerical results comply with the dimensional analysis, and the respective constants (Eqns. 3.9 and 3.10) are therefore determined. The numerical results are compared with previously obtained experimental data by Papakonstantis et al. (2011a). The results obtained using the LRR turbulence model are in good agreement with the experimental data.

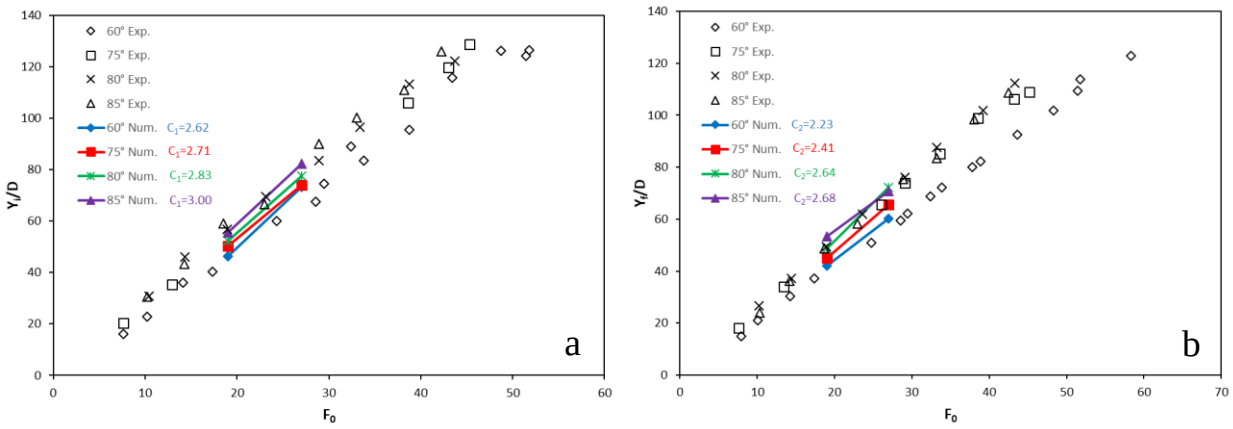

Figure 3.4: Normalized (a) initial and (b) final terminal rise heights for various discharge angles. Experimental data are from Papaconstantis et al. (2011a) and numerical results are from this study.

Final terminal rise height for the 60° jets from the current numerical study were further compared to the other experimental data when normalized by DF_0, as shown in Figure 3.5. Numerical results are within the scattered range of experimental data. It is noted that this large range of values could be due to differences in defining the terminal rise height (Parakonstantis et al., 2011a). Herein, the terminal rise height is obtained after the jet reached a steady-state solution.

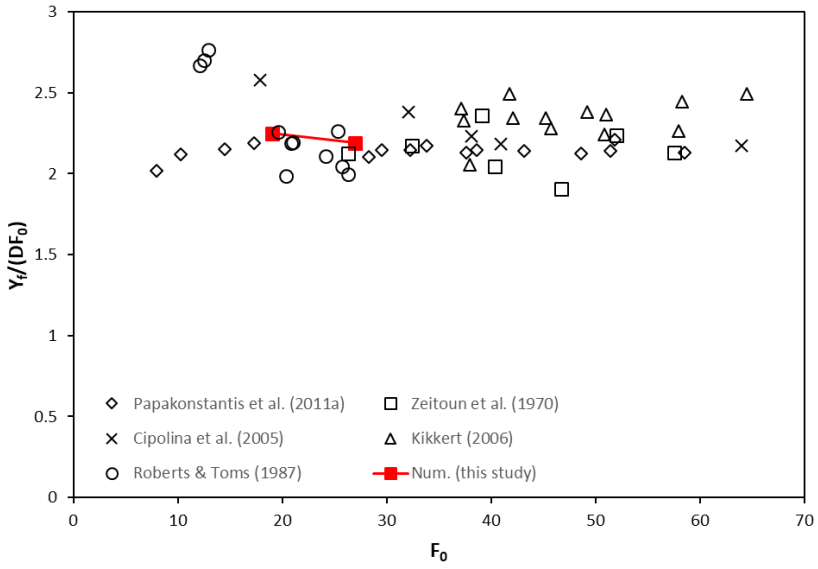

Figure 3.5: Comparison of final terminal rise height for 60° jets.

Effects of the discharge angle θ_0 on the terminal rise height for all discharge angles were compared to past experimental data and are shown in Figure 3.6. Considering that the results by Bloomfield and Kerr (2002) are systematically lower than the other experimental studies (Papakonstantis et al., 2011a), current numerical results are on the lower bound of the data range from experiments. For both initial and final terminal rise heights, the slope of rise becomes milder from 80° to 85° discharge angle compared to the one from 60° to 80°. The maximum final terminal rise height is seen to occur at the 85° jet as shown in Figure 6b. This study does not include vertical jets; however, Papaconstantis et al. (2011a) reported that for the initial terminal rise height, the maximum height happens in 90° jets, whereas, for the final terminal rise height, the maximum height happens in 80° jets. The current numerical study does not match their latter observations on the final terminal rise height.

The ratios of initial to final terminal rise heights Y_i/Y_f for various discharge angles were compared to those from two previous experimental studies. As seen in Table 3.2, the values are somewhat close to the experimental studies but on the lower end. However, it is consistent with the previous experimental data in estimating higher values for the 60° and 85° jets compared to the other discharge angles.

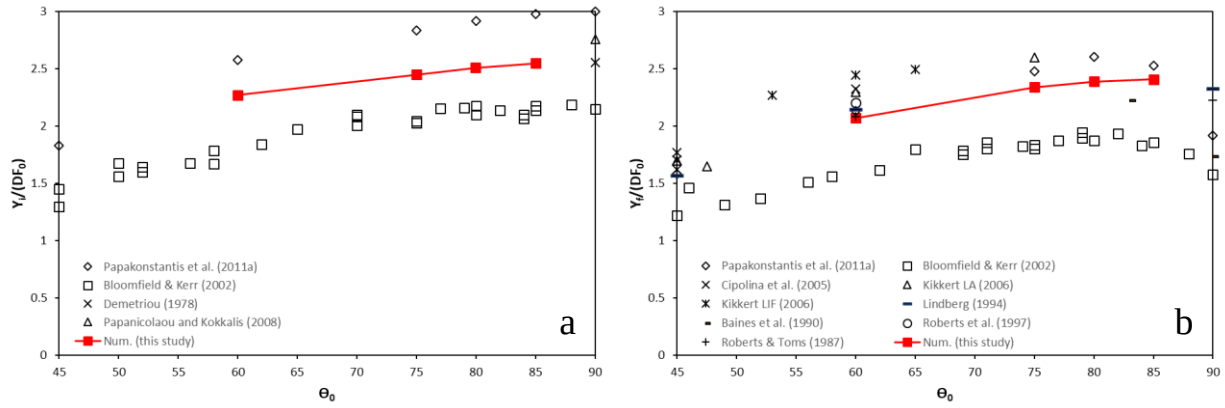

Figure 3.6: Dimensionless (a) initial and (b) final terminal rise heights versus discharge angle Θ_0

Table 3.2: Comparison of Y_i/Y_f between the current numerical study and previous experimental studies

	Y_i/Y_f			
Θ_0	60°	75°	80°	85°
This Study	1.10	1.05	1.05	1.06
Papakonstantis et al. (2011a)	1.20	1.14	1.12	1.18
Bloomfield and Kerr (2002)	1.11	1.08	1.13	1.18

horizontal distance to the location of maximum height of outer boundary

The jet outer boundary peak is defined based on the outer boundary trajectory. The horizontal location of the jet outer boundary peak, X_y, is normalized by the nozzle diameter, D, and is plotted versus F_0 in Figure 3.7. Similar to previous parameters, the results generated by the model when using the LRR turbulence model are consistent with the experimental data obtained in Papakonstantis et al. (2011a). Besides the 60° jets, the other discharge angles predict slightly higher values for X_y compared to the experimental data.

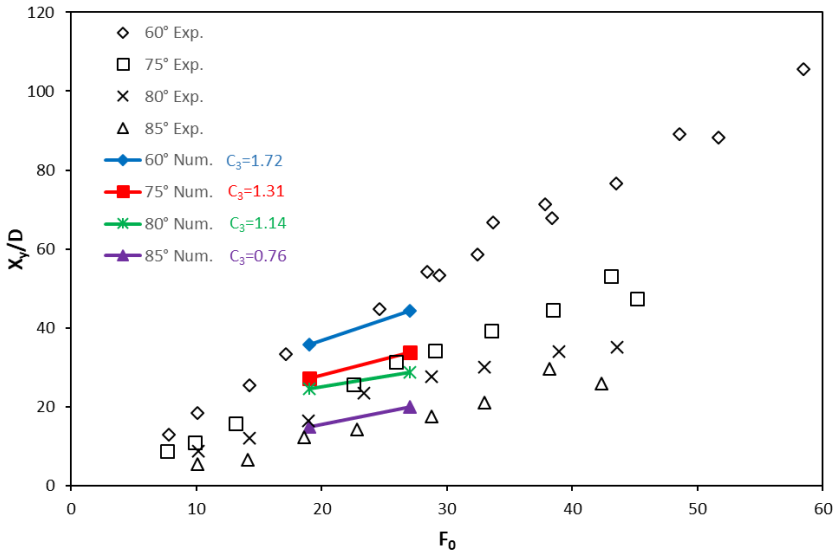

Figure 3.7: Normalized horizontal location of jet outer boundary peak versus F_0 for various discharge angles. Experimental data are from Papaconstantis et al. (2011a) and numerical results are from this study.

Figure 3.8 compares the dimensionless distances X_y/DF_0 from this study to previous experimental data. It is noted that except for the data by Papakonstantis et al. (2011a), the other experimental data refer to the horizontal distance of the maximum height of the jet centerline, and that could be the reason that the current numerical results seem to predict a slightly longer distance and therefore closer values to Papakonstantis et al. (2011a) than other experimental data. As seen in Figure 3.8, it is evident that the dimensionless distance X_y/DF_0 decreases as the discharge angle increases and becomes theoretically zero for θ_0=90°.

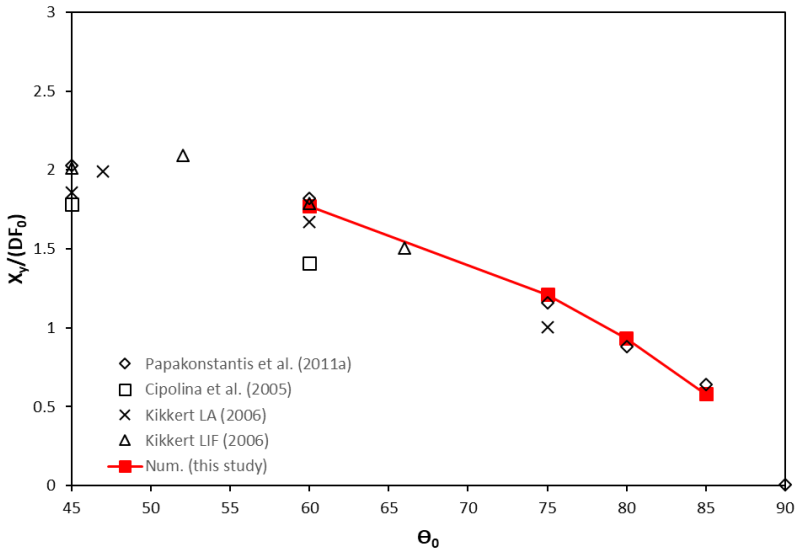

Figure 3.8: Dimensionless horizontal location of jet outer boundary peak as a function of the discharge angle Θ_0

horizontal distance to the location of outer boundary at return point

The normalized horizontal distance from the nozzle to the point where the jet outer boundary returns at the elevation of the source X_i/D is plotted in Figure 3.9 against the densimetric jet Froude number F_0 for various discharge angles. The numerical results follow the same pattern as the distance to the maximum height, where they are slightly longer when compared to the data by Papakonstantis et al. (2011a). The C4 constants are shown in Figure 3.9 for various discharge angles. The dependence of the dimensionless distance X_i/DF_0 on the discharge angle is shown in Figure 3.10 and as expected, it decreased as θ_0 is increased.

The results regarding the constants C1, C2, C3 and C4 of equations 3.9 to 3.12 are summarized in Table 3.3 and are compared to those from Papakonstantis et al. (2011a). The final terminal rise height, which is reported more frequently in the literature, is summarized in Table 3.4 for various studies. As seen in Table 3.4, the predicted constants in the current numerical study are in general good agreement with the previous experimental data and on the higher end of the range.

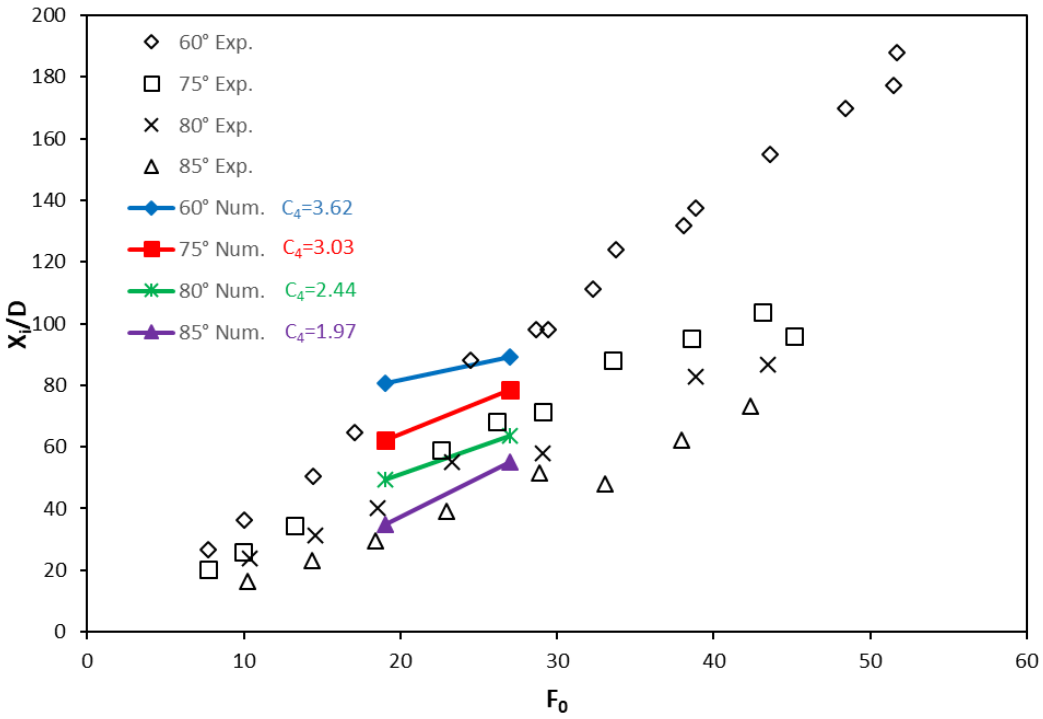

Figure 3.9: Normalized horizontal location of jet outer boundary return point versus F_0 for various discharge angles. Experimental data are from Papaconstantis et al. (2011a) and numerical results are from this study.

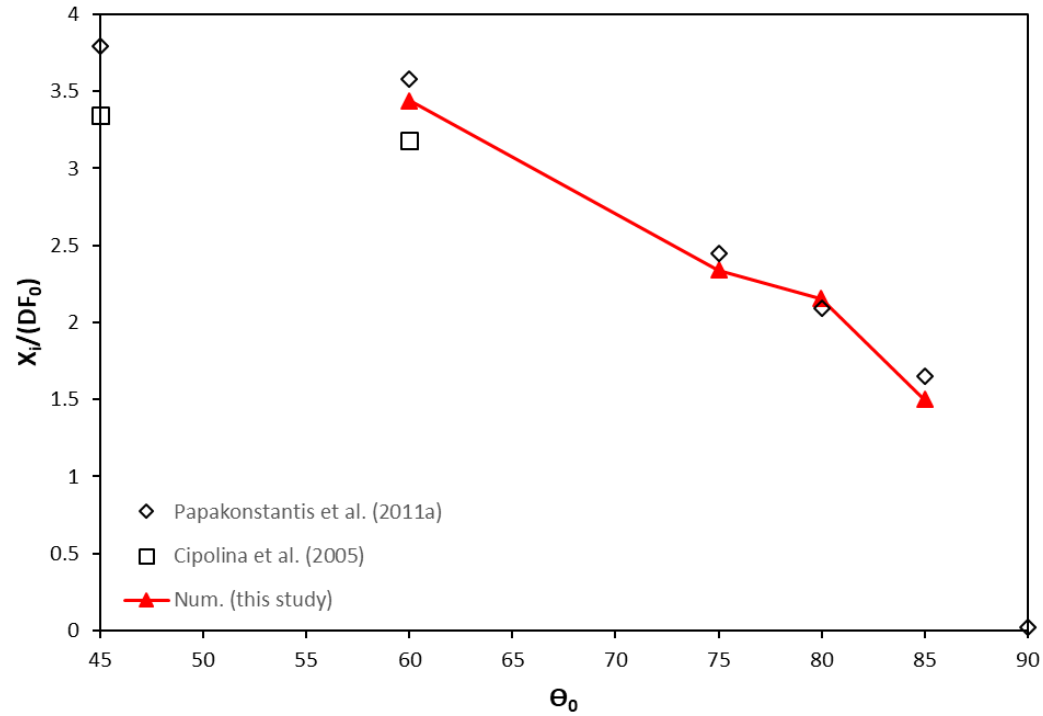

Figure 3.10: Dimensionless horizontal location of jet outer boundary return point as a function of the discharge angle Θ_0.

Table 3.3: Summary of jet geometrical coefficients (equations 3.9 to 3.12).

θ_0	Study	$C_1=Y_i/DF_0$	$C_2=Y_f/DF_0$	$C_3=X_y/DF_0$	$C_4=X_i/DF_0$
60	Papakonstantis et al. (2011a)	2.53	2.13	1.84	3.59
	This Study	2.62	2.23	1.72	3.62
75	Papakonstantis et al. (2011a)	2.80	2.47	1.15	2.51
	This Study	2.71	2.41	1.31	3.03
80	Papakonstantis et al. (2011a)	2.96	2.59	0.88	2.16
	This Study	2.83	2.64	1.14	2.44
85	Papakonstantis et al. (2011a)	2.99	2.51	0.60	1.60
	This Study	3.00	2.68	0.76	1.97

Table 3.4: Comparison of results for the jet final terminal rise height (equation 3.10: $C_2=Y_f/DF_0$).

Study / θ_0	**60**	**75**	**85**	**90**
This Study	2.23	2.41	2.64	2.68
Papakonstantis et al. (2011a)	2.13	2.47	2.59	2.51
Zeitoun et al. (1970)	2.13	–	–	–
Lindberg (1994)	2.14	–	–	–
Bloomfield and Kerr (2002)	1.63	1.89	1.91	1.84
Cipollina et al. (2005)	2.32	–	–	–
Kikkert (2006), LA	2.28	2.57	–	–
Kikkert (2006), LIF	2.45	–	–	–
Kikkert et al. (2007), LA	2.05	2.56	–	–
Roberts and Toms (1987)	2.08	–	–	–
Roberts et al. (1997)	2.20	–	–	–

3.4.2 Concentration Characteristics

vertical concentration distributions

The concentration normalized by mean concentration obtained on a vertical line on the jet axis plane at location X_y of the terminal rise height is plotted in Figure 3.11. As seen in the figure,

distribution of time-averaged concentration is not symmetric. The scatter at small elevations Y could be due to the buoyancy instabilities in that region as observed by Kikkert et al. (2007) and Papakonstantis et al. (2011b).

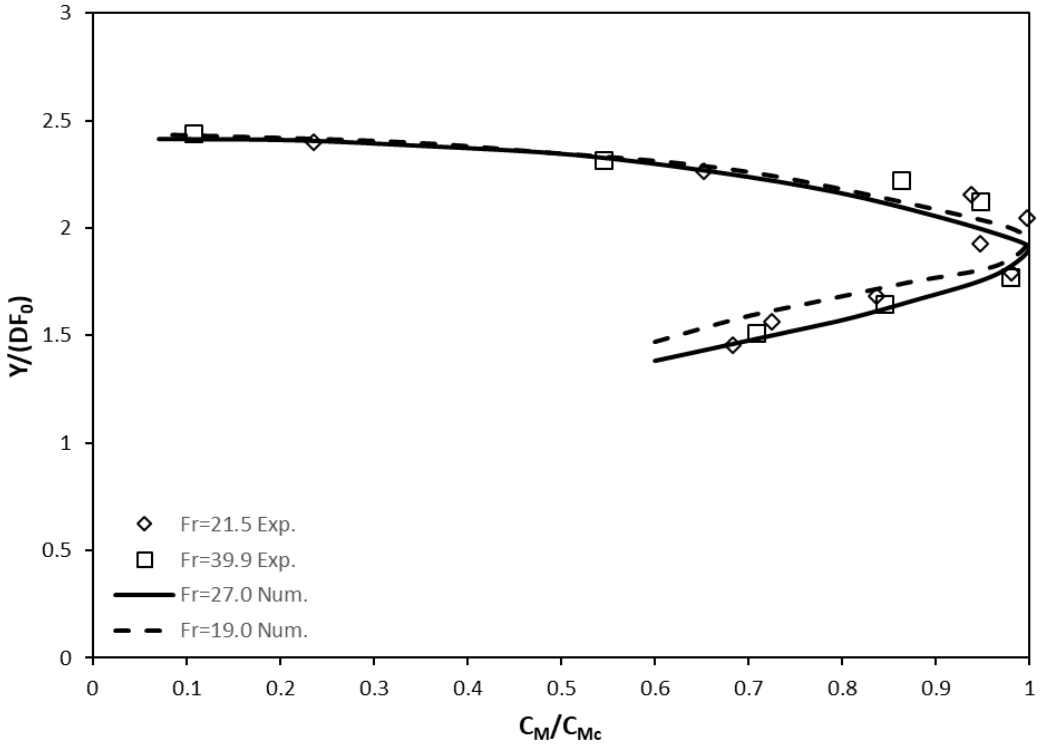

Figure 3.11: Vertical distribution of dimensionless mean concentration at Xy for θ0=75°. Experimental data are from Papaconstantis et al. (2011a) and numerical results are from this study.

width of vertical mean concentration distribution

Figure 3.12 shows the normalized 1/e-width of the jet b_c/DF_0 of the Gaussian vertical mean concentration distributions against F_0 for 60° and 75° discharge angles. Despite the large scatters in the experimental data, the numerical jet half widths are relatively close to each other for 60° and 75° discharge angles. The numerical study investigated two F_0 numbers and there might have been more variations in the presence of more numerical simulations. As discharge angle approaches the vertical jet, larger fluctuations in the jet half width could be expected.

centreline dilution

Jet centerline minimum dilution can be calculated as:

$$S = \frac{C_0}{C_{Mc}} \tag{3.23}$$

Where C_0 is the jet centerline concentration at the nozzle and C_{Mc} is the maximum concentration obtained at the terminal rise height (and/or return point).

Normalized centreline dilutions S_t and S_i with the densimetric Froude number are shown in Figure 3.13a for all discharge angles. Note that the centreline dilution at the terminal rise height is almost independent of θ_0, similar to observation by Kikkert et al. (2007) for $\Theta 0$ = 15°, 30°, 45° and 60°. This seems to be reasonable since if the discharge angle increases, the rise height would increase but the horizontal distance would decrease, resulting in almost similar trajectory lengths. The numerical results obtained from this study follow the same trend as Papakonstantis et al. (2011b). However, there is no experimental data for densimetric Froude numbers smaller than 28 to compare the numerical results to.

The data of the centreline dilution at the return point show a considerable scatter probably because in this region, the concentration is close to that of the ambient water. This has been shown in Figure 3.13b, where the values of the normalized minimum dilution are plotted against all discharge angles. The normalized dilution at the terminal rise height does not vary significantly with θ_0. The numerical results of LRR turbulence model showed a great agreement with experimental data collected by Papakonstantis et al. (2011b).

Table 3.5 summarizes the centerline dilution results of the current study compared with the other experimental results for 60° and 75° discharge angles. As seen in the table, there is a very good agreement between the numerical results and experimental data. The dilution at the terminal rise height of 60° jet seems to be slightly underpredicted when compared to the previous studies and in a better agreement with Roberts and Toms (1987). The average value of S_i/S_t is 3.55 for the 60° jets and 3.25 for 75° jets. The latter is very close to the value of 3.30 reported by Papakonstantis et al. (2011b), while the former is higher than the value of 3.0 reported by them.

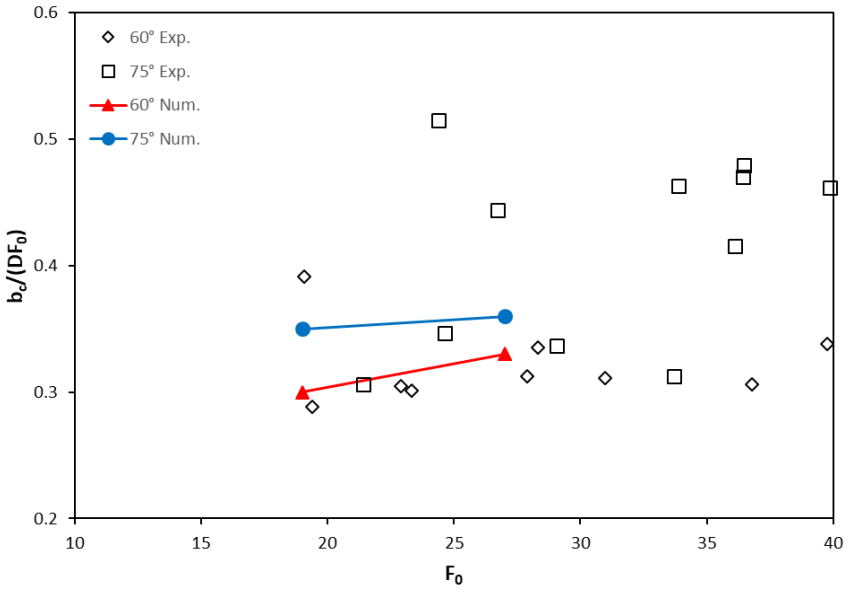

Figure 3.12: Dimensionless width of vertical mean concentration distribution. Experimental data are from Papaconstantis et al. (2011a) and numerical results are from this study.

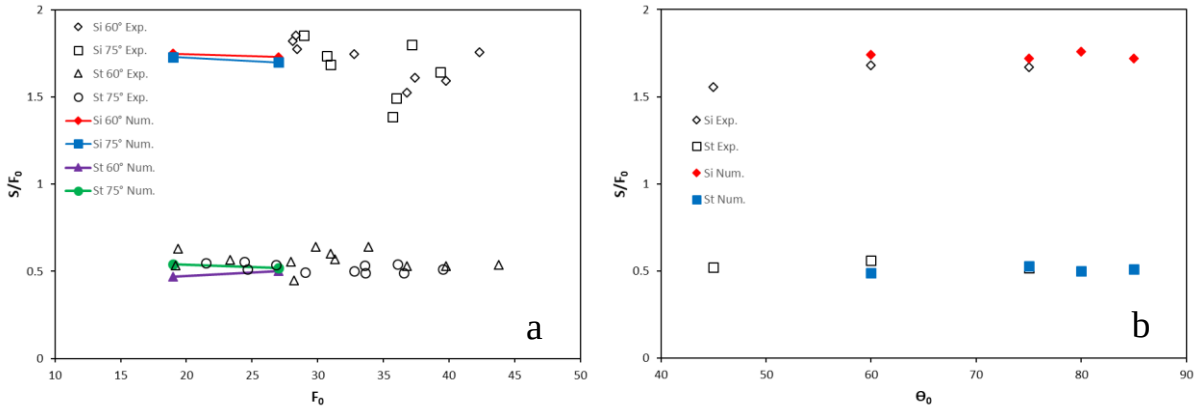

Figure 3.13: Normalized minimum (centerline) dilution at terminal rise height and return point against (a) densimetric Froude number and (b) discharge angle. Experimental data are from Papaconstantis et al. (2011a) and numerical results are from this study.

Table 3.5: Jet centerline dilution results.

	60		**75**	
Study	S_t/F_0	S_i/F_0	S_t/F_0	S_i/F_0
This Study	0.49	1.74	0.53	1.72
Papakonstantis et al. (2011b)	0.56	1.68	0.51	1.67
Zeitoun et al. (1970)	0.56	1.12	–	–
Roberts and Toms (1987)	0.38	1.03	–	–
Roberts et al. (1997)	–	1.60	–	–
Nemlioglu and Roberts (2006)	–	1.70	–	1.80
Kikkert et al. (2007)	0.53	–	–	–

3.5 Conclusions

Dimensional analysis suggests that the geometrical characteristics of inclined dense jets normalized by the nozzle diameter D and the densimetric Froude number F_0 take constant values for any specific discharge angle. Four discharge angles, θ_0 = 60°, 75°, 80° and 85°, were numerically simulated for two densimetric Froude numbers, F_0 = 19 and 27, using the LRR turbulence model in OpenFOAM. These discharge angles were not previously modelled numerically. Geometrical and dilution characteristics of such jets were investigated in this study. Initial and final jet terminal rise heights as well as horizontal distance to the terminal rise height and return point at the source elevations were estimated for the jet geometry. Jet concentration was estimated for two discharge angles, 60° and 75°, and were compared to the experimental data by Papakonstantis et al. (2011b).

The following conclusions can be drawn from this study:

- Dimensionless initial and final terminal rise heights (Y_i/DF_0 and Y_f/DF_0) increase with discharge angle and become maximum for the 85° jets. This is in agreement with the most previous experimental studies except Papakonstantis et al. (2011a) which reported 80° discharge angle with the highest final terminal rise height;
- The ratio of Y_i/Y_f is about 1.05 for the four discharge angles simulated in this study, with the maximum of 1.10 for the 60° jets. This ratio seems to be independent of discharge angle;
- Dimensionless horizontal distance from the nozzle X_y/DF_0 at which the terminal rise height appears as well as the horizontal distance X_i/DF_0, where the outer jet boundary crosses the nozzle elevation, decreases as the discharge angle increases;
- Vertical distributions of dimensionless mean concentration at the location of the terminal rise height are asymmetric. It is approximately a Gaussian distribution and deviates from a Gaussian form in the falling limb due to the buoyancy induced instabilities in the jet farther from the discharge point; and

- The jet centreline dilutions at the terminal rise height and at the jet return elevation, normalized by the densimetric Froude number, suggest minimal changes for different discharge angles.

Notations

B_0 = specific buoyancy flux at source
b_c = nominal width of vertical mean concentration distribution where $C_M = e^{-1}C_{Mc}$
C = concentration relative to ambient concentration
C_M = mean (time-averaged) concentration
C_{Mc} = mean concentration at jet axis
C_{RMS} = RMS value of concentration fluctuations
$C_1, \ldots, C_4$ = constants
D = jet pipe diameter
F_0 = densimetric Froude number at source
g′ = apparent gravitational acceleration at source
L_M, L_Q = characteristic length scales
M_0 = specific momentum flux at source
Q_0 = volume flux at source
U_0 = jet exit velocity
S_i = centreline (minimum) dilution at region where the jet returns at source elevation
S_t = centreline (minimum) dilution at terminal height
X = horizontal axis of the coordinate system
X_y = horizontal distance from jet exit to location of terminal rise height
X_i = horizontal distance from jet exit to outer jet boundary at nozzle elevation
Y = vertical axis of coordinate system
Y_f = final terminal height of rise (refers to outer jet boundary)
Y_i = initial terminal height of rise
θ_0 = discharge angle to horizontal
ϱ = density
$\Delta\varrho$ = density difference

References

Abraham G. 1967. Jets with negative buoyancy in homogeneous fluid. J Hydraul Res. 5(4): 235–248.

Alfaifi, H., Mohammadian A., Bonakdari, H. (2019). Experimental and empirical study of geometrical characteristics of 15° and 52° inclined negatively buoyant jets. Journal of Coastal Research (Coastal Education & Research Foundation). Accepted.

Alfaifi, H., Mohammadian, A., Kheirkhah Gildeh, H., Gharavi, A. (2018). "Experimental and numerical study of the characteristics of thermal and nonthermal offset buoyant jets discharged into stagnant water", J. Des. & Wat. Treat., doi:10.5004/dwt.2019.23477.

Baines, W.D., Turner, J.S., Campbell, I.H. (1990). Turbulent fountains in an open chamber. J. Fluid Mech. 212, 557–592.

Bleninger, T., Jirka, G.H., 2008, “Modelling and Environmentally Sound Management of Brine Discharges from Desalination Plants”, Desalination Vol. 221/1–3 pp. 585–597.

Bloomfield LJ, Kerr RC. 2000. A theoretical model of a turbulent fountain. J Fluid Mech. 424: 197–216.

Bonakdari, H., Mohammadian, A. (2019). Evolutionary prediction of an inclined dense jet in shallow water. DESALINATION AND WATER TREATMENT 155, 32-47.

CEDERWALL, K. *1968* Hydraulics of marine waste disposal. Chalmers Institute of Technology, Hydraulics Division, Report no. 42, Göteborg, Sweden.

Cipollina, A., Brucato, A., Grisafi, F., Nicosia, S. (2005). Benchscale investigation of inclined dense jets. J. Hydraulic Eng. 131(11), 1017–1022.

Einav R, Lokiec F. 2003. Environmental aspects of a desalination plant in Ashkelon. J. Desalin. 156: 79-85.

Elhaggag M.E., Elgamal M.H., Farouk M.I. (2011). Experimental and numerical investigation of desalination plant outfalls in limited disposal areas. J. Environ. Protec., 2:828-839.

Fischer HB, List EJ, Koh RCY, Imberger J, Brooks NH. 1979. Mixing in inland and coastal waters. Academic Press, New York, USA.

Genthner K. (2005). Research and Development in Desalination–Current Activities and Demand, in Lecture Notes. DME Seminar, Berlin.

Huai W, Li Z, Qian Z, Zeng Y, Han J. 2010. Numerical simulation of horizontal buoyant wall jet, J Hydrody 22(1):58-65.

Hoepner T. and Windelberg J., (1996), “Elements of environmental impact studies on coastal desalination plants”, Desalination, Vol. 108, pp. 11–18.

R.I. Issa. Solution of the implicitly discretised fluid flow equations by operator-splitting. Journal *of Computational Physics*, 62(1):40–65, 1986.

Jiang M, Law AWK. 2018. Mixing of swirling inclined dense jets – A numerical study. J. Hydro-Env. Res. 118-130.

Jiang M, Law AWK, Lai ACH. 2019. Turbulence characteristics of 45 inclined dense jets. J. Env. Fluid. Mech. 19:27-54.

Jirka G.H. (2004). Integral Model for Turbulent Buoyant Jets in Unbounded Stratified Flows. Part I: Single Round Jet. J. Env. Fluid Mech. 4: 1. https://doi.org/10.1023/A:1025583110842.

Jirka G.H. (2006). Integral Model for Turbulent Buoyant Jets in Unbounded Stratified Flows Part 2: Plane Jet Dynamics Resulting from Multiport Diffuser Jets. J. Env. Fluid Mech. 6: 43. https://doi.org/10.1007/s10652-005-4656-0.

Jirka G.H. and Doneker R.L., Hydrodynamic classification of submerged single port discharges, J. Hydraul. Eng., 117 (1991) 1095–1112.

Kikkert, G.A., Davidson, M.J., Nokes, R.I. (2007). Inclined negatively buoyant sischarges. J. Hydraulic Eng. 133(5), 545–554.

Kim, D. G., and Cho, H. Y. (2006). “Modeling the buoyant flow of heated water discharged from surface and submerged side outfalls in shallow and keep water with a cross flow.” J. Environ. Fluid Mech., 6(6), 501–518.

Kim, Y. D., Seo, I. W., Kang, S. W., and Oh, B. C. (2002). “Jet integralparticle tracking hybrid model for single buoyant jets.” J. Hydraul. Eng., 10.1061/(ASCE)0733-9429(2002)128:8(753), 753–760.

Kheirkhah Gildeh H (2013) Numerical modelling of thermal / saline discharges in coastal waters. Master of Applied Science Thesis in Civil Engineering. University of Ottawa, Ottawa, Canada.

Kheirkhah Gildeh, H., Mohammadian, A., Nistor, I., and Qiblawey, H. (2014a). "Numerical modelling of turbulent buoyant wall jets in stationary ambient water.", J. Hydraul. Eng., 140(6), 04014012.

Kheirkhah Gildeh, H., Mohammadian, A., Nistor, I., and Qiblawey, H. (2014b). "Numerical modelling of 30° and 45° inclined dense turbulent jets in stationary ambient.", J. Environ. Fluid Mech.,15(3): 537-562.

Kheirkhah Gildeh, H., Mohammadian, A., Nistor, I., Qiblawey, H., and Xiaohui, Y. (2015). "CFD modelling and analysis of the behavior of 30° and 45° inclined dense jets; New Numerical Insights.", J. Appl. Water. Eng. & Res., DOI:10.1080/23249676.2015.1090351.

Lai CCK, Lee JHW. 2012. Mixing of inclined dense jets in stationary ambient. J Hydro-environ Res. 6: 9-28.

Lee J.H.W., Chu V.H. (2003). Turbulent jets and plumes: a lagrangian approach. Academic Publishers, the Netherland.

McLellan, T.M., Randall, R.E. (1986). Measurement of brine jet height and dilution. J. Waterw. Port Coastal Ocean Eng. 112(2), 200–216.

Millero FJ, Poisson A. 1981. International one-atmosphere equation of state of sea water. J Deep-Sea Res. 28A(6): 625 to 629.

Oliver CJ, Davidson MJ, Nokes RI. 2008. k-ε prediction of the initial mixing of desalination discharges, J Environ Fluid Mech. 8:617-625.

Papakonstantis, I.L., Christodoulou, G.C., and Papanicolaou, P.N. 2011a. Inclined negatively buoyant jets 1: geometrical characteristics, Journal of Hydraulic Research, 49: 3-12.

Papakonstantis, I.L., Christodoulou, G.C., and Papanicolaou, P.N. 2011b. Inclined negatively buoyant jets 2: concentration measurements, Journal of Hydraulic Research, 49: 13-22.

Pincince, A.B., List, E. J. (1973). "Disposal of brine into an estuary." J. Water Poll. Control Fed., 45(11), 2335-2344.

Roberts, P.J.W., Ferrier, A., Daviero, G. (1997). Mixing in inclined dense jets. J. Hydraulic Eng. 123(8), 693–699.

Roberts, P.J.W., Toms, G. (1987). Inclined dense jets in flowing current. J. Hydraulic Eng. 113(3), 323–341.

Schreiner, HK., Rennie, CD, Mohammadian, A. (2018). Trajectory of a jet in crossflow in a channel bend. Environmental Fluid Mechanics 18 (6), 1301-1319.

Shao D, Law AWK. 2010. Mixing and boundary interactions of 30 and 45 inclined dense jets. J Env. Fluid Mech. 10:521-553.

Turner JS. 1966. Jets and plumes with negative or reversing buoyancy. J Fluid Mech. 26: 779–792.

Vafeiadou P, Papakonstantis I, Christodoulou G. 2005. Numerical simulation of inclined negatively buoyant jets. The 9th international conference on environmental science and technology, September 1-3, Rhodes island, Greece.

Wright, S.J. (1977). Mean behavior of buoyant jets in cross flow. Journal of Hyd Eng., 103(5), 449 513.

Yan X, Mohammadian A. 2017. Numerical Modeling of Vertical Buoyant Jets Subjected to Lateral Confinement. J. Hydr. Eng. 04017016-1.

Yan X, Mohammadian A. 2019. Multigene Genetic-Programming-Based Models for Initial Dilution of Laterally Confined Vertical Buoyant Jets. Journal of Marine Science and Engineering 7 (8), 246.

Zeitoun, M.A., McIlhenny,W.F., Reid, R.O. (1970). Conceptual designs of outfall systems for desalting plants. Res. and Devel. Progress Report 550, Office of Saline Water, US Dept. of Interior, Washington DC.

Zhang, H., Baddour, R.E. (1998). Maximum penetration of vertical round dense jets at small and large Froude numbers. J. Hydraulic Eng. 124(5), 550–553.

Zhang S, Law AWK, Jiang M. 2017. Large eddy simulations of 45° and 60° inclined dense jets with bottom impact. J. Hydro.-Env. Res. 54-66.

4 Inclined Dense Effluent Discharge Modelling in Shallow Waters[3]

Abstract: Two jet discharge angles relative to the horizontal (30° and 45°) were investigated based on the experimental results from Jiang et al. (J Hydraul Eng 140:241-253, 2014). Five Reynolds-averaged Navier-Stokes (RANS) turbulence models were examined in this study: realizable k-ε and k-ω SST models (known as two-equation turbulence models), v2f (four equations to model anisotropic behavior) and LRR and SSG turbulence models (known as Reynolds stress models - six equations to model anisotropic behavior). Three mixing regimes introduced in Jiang et al. (2014) were reproduced numerically for both discharge angles applying various turbulence models: full submergence, plume contact and centerline impingement regimes (i.e. FSR, PCR and CIR). Key geometrical and dilution properties of these jets at surface contact (X_s, S_s) with minimum dilution and jet centerline return point (X_r, S_r) were compared to those available from experiments. Normalization parameter that was selected for jets in shallow waters is H/D (water depth above discharge point over nozzle diameter). It was found that surface attachment increases the return point length from the nozzle and that surface dilution decreases from FSR toward CIR. Among turbulence models tested herein, Reynolds stress models (LRR and SSG) predicted the effluent discharge kinematic and dilution properties better compared to two- and four-equations models. This is mainly attributed to the anisotropic nature of the effluent discharge problem studied herein and that these models are better capable to account for anisotropies.

Keywords: Inclined dense jet; Shallow water, Surface dilution, Return point, Effluent discharge, OpenFOAM

---

3 This chapter of the study has been published as: Kheirkhah Gildeh, H., Mohammadian, A., Nistor, I. (2021). "Inclined Dense Effluent Discharge Modelling in Shallow Waters", Environ. Fluid Mech. 21, 955–98, https://doi.org/10.1007/s10652-021-09805-6.

4.1 Introduction

Seawater desalination plants are increasingly designed and constructed around the world. They have been identified to provide as high-productivity potable water sources for the rising population in the coastal cities such as those dotting the shorelines of arid countries around the Persian Gulf. A byproduct of desalination processes, such as reverse osmosis, is the saline effluent which is usually discharged back into the sea after some degree of treatment. These hypersaline effluents are often the most prominent problem-causing factors with potential to impact coastal waters in the near-field discharge area.

Several effluent discharge methods are currently used in the industry such as submerged outfalls with different configurations for the outlet nozzles, as well as free surface conveyance channels. The former method was proven to be more efficient in terms of mixing and dispersion of effluents. Moreover, among all types of submerged jets, the use of inclined dense jets was reported to be the most popular method used in practice (e.g. [2], [3]).

There may be some examples where there is not enough water column in the zone of the effluent discharge and thus discharge impact to the water surface is inevitable. Several experimental and numerical studies have been conducted to study mixing properties of inclined dense jets in deep water conditions with enough coverage for full submergence discharge regimes (e.g. [3-7]). However, few studies focused on the mixing properties of inclined dense jets in shallow water where discharge impacts the water surface. A schematic view of this configuration is shown in Figure 4.1.

Jiang et al. [1] conducted, in premiere, a comprehensive experimental study for the discharge of 30° and 45° jets into shallow waters. Three different regimes were categorized by [1] for inclined dense discharges: (i) *full submerged regime (FSR)* for discharges in deep waters with sufficient water depth above the discharge point with a certain discharge momentum to keep the full jet submerged, (ii) *plume contact regime (PCR)* for discharges where the outer jet layer impacts the water surface but not the jet centerline (Figure 4.1 represents a PCR) and (iii) *centerline impingement regime (CIR)* for discharges where the jet centerline impacts the water surface. [1] experimentally investigated the jet trajectory for these three regimes and presented the minimum surface dilution (S_s) rate for PCR (i.e., S_s in the attached area in Figure 4.1) and CIR in relationship

to the jet densimetric Froude number (F) and cover water depth (H). They observed that the surface attachment increases the return point length from the discharge point. It was found that S_s decreases from FSR (which theoretically approaches infinity) toward CIR, when H is reduced or a certain momentum in a discharge. Their experimental data showed that the surface properties of both $S_s.D/H$ and X_s/H are functions of FD/H, while at the return point, $S_r.D/H$ and X_r/H are not only as function of FD/H, but are also dependent on H/D (the non-dimensional cover depth), where D, X_s, S_r, and X_r represent nozzle diameter, horizontal location of minimum dilution at the water surface, minimum dilution at the return point and horizontal location of minimum dilution at the return point, respectively.

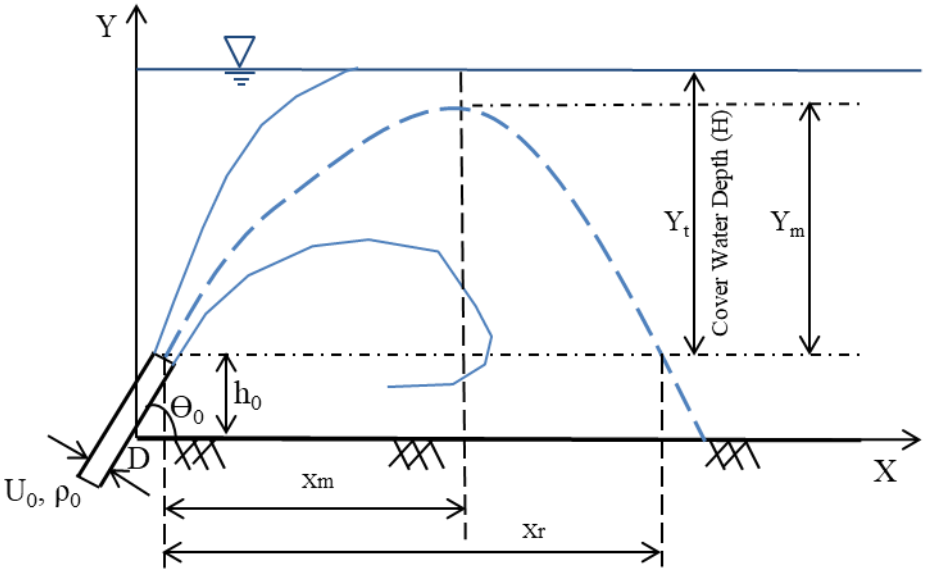

Figure 4.1: Schematic side view of an inclined dense jet discharging into stagnant shallow water with surface attachment. Effluent discharges from a round nozzle at an angle Θ0 with respect to the horizontal level and impinges into the surface water due to its momentum force. Jet interaction with the water surface reduces the entertainment, and thus, the dilution. The surface attachment increases the inclined jet trajectory path compared to discharge in a deep water and therefore the expected return point is farther away from the nozzle.

Abessi et al. [8] conducted a study similar to [1] and added 60° jets to their experiments compared to the previous study of [1]. They also presented the dilution results at key locations including the surface impact in the case of PCR and CIR. They found that PCR occurs at FD/H= 0.80, 0.48 and 0.42 for nozzle angles of 30°, 45° and 60°, respectively and dilution starts decreasing above these values as the jet transitions to CIR. CIR was found to occur at FD/H= 1.15, 0.70 and

0.64 for nozzle angles of 30°, 45° and 60°, respectively. It was also discussed that in the CIR, the asymmetrical concentration profiles resemble half-Gaussian profiles similar to those of wall jets. Kheradmand et al. [9] performed a high-level experimental and CFD study to compare the jet characteristics in shallow water for discharge angles of 30° and 45° jets. They used OpenFOAM with realizable k-ε and LRR (Launder, Reece and Rodi) turbulence models. There were no quantitative comparisons between the numerical and experimental results and only side-by-side snapshots of the spatio-temporal jet evolution were compared for FSR, PCR and CIR. They found out that the RANS turbulence models can predict the discharge trajectory when impinging the water surface. However, the qualitative comparison of averaged side plan of the discharge revealed some underestimation and overestimation of jet trajectory at different time stamps.

Ahmed et al. [10] studied the effluent discharges in shallow water for the vertical dense fountains. They experimentally measured the jet maximum height (Y_t), the minimum return point dilution (S_r) and the jet lateral spread (R_{sp}). Slightly different names were used for the vertical jet regimes in the shallow water: *deep*, *intermediate* and *impinging mixing regimes*, which are equivalent of FSR, PCR and CIR adopted in this study. Y_t values increased as jets entered into intermediate regime from deep regime. They found that S_r for the intermediate regime were higher than those of deep regime. It was also observed that the Sr decreased dramatically in the impinging mixing regime where the jet continuously impacted the water surface. Finally, jet vertical height (Z_m) was normalized by length scale r_0Fr_0 (r_0 is the nozzle radius and Fr_0 is the jet densimetric Froude number) and it was shown that normalized jet vertical height, Z_m/r_0Fr_0, is constant at higher water depths but increases rapidly at shallow water depths.

Similar to [10], [11] also studied the vertical jets with surface impingement, with more focus on the measurement of the spreading width of the vertical fountain, as well as of the concentration dilution at the surface impact point. They compared their experimental data to the CORJET model (a CORMIX sub-model). However, the capability of the CORJET model was deemed limited in predicting flow properties of discharges impinging the water surface and the numerical results of the centerline dilution only were presented. Inclined dense discharges feature complex three-dimensional (3D) turbulent flows and integral models are not accurate in estimating their flow properties. The latter represents an important shortfall of integral models compared to CFD

models that they are unable to provide a detailed understanding of discharge kinematic and dilution properties.

To the best knowledge of authors [12], except the high-level numerical study by [9], there is no study reported in the literature dealing with the numerical modelling of dense effluent discharges in the shallow waters with surface attachment. Past numerical studies on mixing of effluent discharges have only focused on FSR. [5,6] discussed the suitability of Reynolds-averaged Navier-Stokes (RANS) turbulence models in modelling of mixing properties of inclined dense jets. [7] used both Large Eddy Simulation (LES) and RANS models to simulate 45° and 60° inclined dense jets and found that despite slight improvement in estimation of some geometrical properties of the jets (e.g. return point and centerline peak), it underestimated the dilution at the return point by approximately 20% compared to data from experiments.

As reported in past numerical studies of mixing of inclined dense jets in FSR (e.g. [4-6]), RANS models perform relatively well in replicating the geometrical and flow properties of effluent discharges. However, more investigations regarding the sensitivity of these models to various input parameters as well as of the receiving ambient water (e.g. shallow water with surface attachment) are required. RANS models are popular in mixing applications, as they have a lower CPU demand compared to the LES models while still providing an adequate theoretical framework. There are some applications such as the scalar transport in a vegetated environment [13] that the models should go beyond the estimate of mean concentration and should resolve smaller scales of the fluid motions. In those cases, LES models may be a more suitable approach. It is noteworthy that more CFD applications are currently being run on GPU which may improve the computational performance of solvers being used for mixing problems.

The main objective of this study is to numerically investigate effluent discharges of inclined dense discharges in shallow waters, where the jet attaches to the surface, using OpenFOAM CFD model. This aspect was not investigated in past studies to the best knowledge. This study attempts to address this research gap. Several RANS turbulence models were employed to estimate the trajectory and dilution properties of effluent discharges impinging the water surface. The performance of these models to predict the geometric and kinematic properties of jets were evaluated by comparing its results against previously published experimental data.

4.2 Methodology

4.2.1 Numerical Details

A RANS turbulence closure family was adopted for this study. While LES models might improve the simulation of phenomena in quiescent ambientes, the benefits are incremental and suffer large computational expense [14].

The governing equations for CFD modelling of inclined dense effluent discharges for incompressible fluids are based on the full Navier-Stokes equations. Using the same analogy described in [15] and [16] for the time-averaged Navier-Stokes equations for continuity, momentum and scalar transport, the deriving equations could be written as [14]:

$$\frac{\partial \rho}{\partial t} + \frac{\partial}{\partial x_i}(\bar{\rho}\overline{u_\iota}) = 0 \tag{4.1}$$

$$\frac{\partial (\overline{\rho u_\iota})}{\partial t} + \frac{\partial}{\partial x_j}\left(\bar{\rho}\overline{u_\iota}\overline{u_j}\right) = \frac{\partial \bar{P}}{\partial x_i} + \bar{\rho} g_i + \frac{\partial}{\partial x_j}\left(\mu \frac{\partial \overline{u_\iota}}{\partial x_j}\right) - \frac{\partial \tau_{ij}}{\partial x_j} \tag{4.2}$$

$$\frac{\partial (\overline{\rho u_\iota})}{\partial t} + \frac{\partial}{\partial x_j}\left(\bar{\rho}\bar{c}\overline{u_j}\right) = \frac{\partial}{\partial x_j}\left(\Gamma \frac{\partial \bar{c}}{\partial x_j}\right) - \frac{\partial q_j}{\partial x_j} \tag{4.3}$$

where subscripts i, j and k denote the axis of system of coordinates; ρ is fluid density; u is fluid velocity; p is pressure; g is gravitational acceleration; μ is fluid viscosity; Γ is scalar diffusivity; c is scalar concentration and overbar denotes time-averaged variables. A Boussinesq hypothesis is applied to some of the selected RANS models (realizable k-ε, k-ω SST and v2f) to estimate the Reynolds stresses, τ_{ij} and turbulent scalar flux q_j, which can be written as:

$$\tau_{ij} = \mu_t \left(\frac{\partial \overline{u_i}}{\partial x_j} + \frac{\partial \overline{u_j}}{\partial x_i}\right) - 2/3(\rho k + \mu_t \frac{\partial \overline{u_k}}{\partial x_k})\delta_{ij} \tag{4.4}$$

$$q_j = \Gamma_t \frac{\partial \bar{c}}{\partial x_j} \tag{4.5}$$

where μ_t is turbulent eddy viscosity; k is turbulent kinetic energy; δ_{ij} is Kronecker delta and Γ_t is turbulent dispersion. Certain other models, such as the Reynolds Stress Models (RSM) described below, directly calculate the Reynolds stresses.

A Finite Volume Method (FVM) was used to discretize the above-mentioned RANS equations. Simulations were conducted using an open-source CFD model, OpenFOAM version 4.1.0 [17], using the twoLiquidMixingFoam solver.

The transient simulations in this study were run long enough to reach a steady state condition for the jet flows. A physical time step of 0.001 s and a time duration of 80 s were selected for the simulations and the velocity and concentration results were then time-averaged.

4.2.2 Model Domain and Boundary Conditions

The model geometry is presented in Figure 4.2. The modelled tank dimensions were selected to be 1.5 m long, 0.5 m wide and 0.3 m deep. These dimensions ensure no recirculation caused by boundary walls. The effluent is discharged with a velocity of U_0 and density of ρ_0 (ranging approximately from 1016 kg/m^3 to 1018 kg/m^3) through a nozzle with a diameter of D=0.006 m. The jet velocity and discharge density were the variable parameters used in this study to model cases for each of the two discharge angles relative to the horizontal axis. The inlet values for k, ε and ω are chosen based on [18] as $k=0.06U_0^2$, $\varepsilon=0.06U_0^3/D$, $\omega=\varepsilon/k$. The ambient water body is still, with a homogeneous density of $\rho_a = 996.4\ kg/m^3$. The nozzle was mounted 0.05 m above the bed to eliminate any boundary effects [19]. There was an outlet face at the other end of the tank with a zero gradient boundary condition positioned perpendicular to the outlet plane. A symmetry boundary was modeled using a zero-gradient condition to represent the atmosphere. The symmetry plane condition specifies that flux and component of the gradient normal to the plane should be zero but free to slide in tangential directions. A Dirichlet condition was used on all wall boundaries to implement the zero-velocity condition. OpenFOAM standard wall functions (e.g. epsilonWallFunction, omegaWallFunction, etc.) were also implemented for the wall surfaces to model hydraulically smooth walls.

The model domain was spatially discretized using a hexahedral mesh with a minimum cell size of 0.002 m around the nozzle and maximum cell size of 0.025 m at the farthest end of tank at the outlet face. The mesh was refined with a higher resolution along the potential jet trajectory to better resolve the flow properties. As part of the mesh sensitivity analysis, more than 10 initial test runs were performed to ensure that the mesh was sufficiently refined to resolve the velocity and concentration gradients especially close to the nozzle. The grid refinement criterion was set to reach a difference of less than 2% between the predicted results between the last two grids employed. When this criterion was reached, it was assumed that a satisfactory mesh was

established and no further refinement were needed (Figure 4.3). The final mesh configuration used in this study includes ~1.8 million cells.

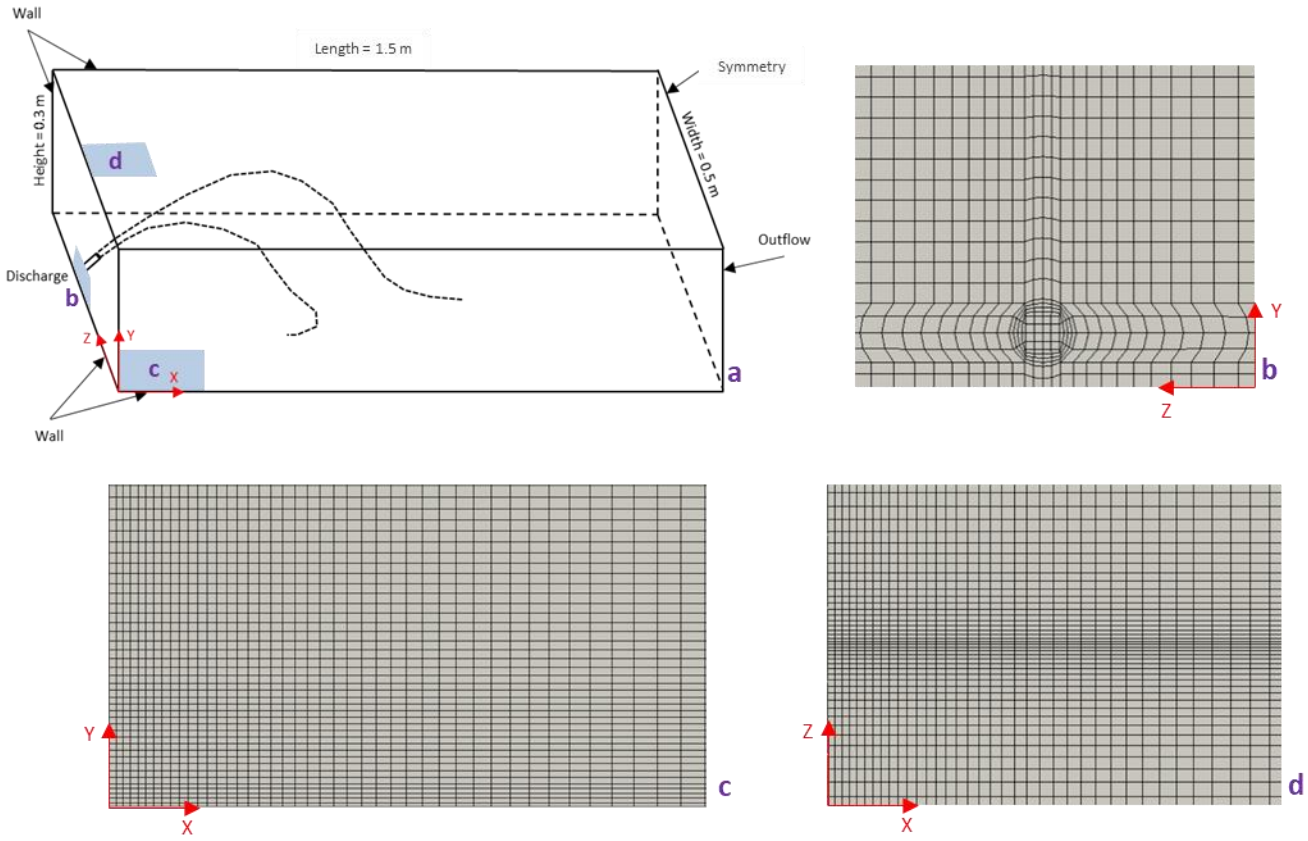

Figure 4.2: Final model geometry and boundary conditions.

For all the simulations in this study, a physical time step of 1×10^{-3} s was used, which leads to a Courant-Friedrichs-Lewy (CFL) number less than 0.5 for stability considerations. Smaller time steps were also tried but the results remained the same. The convergence criteria for each time step were set such that the residuals for the velocity components and pressure are 1×10^{-5} and 1×10^{-6}, respectively.

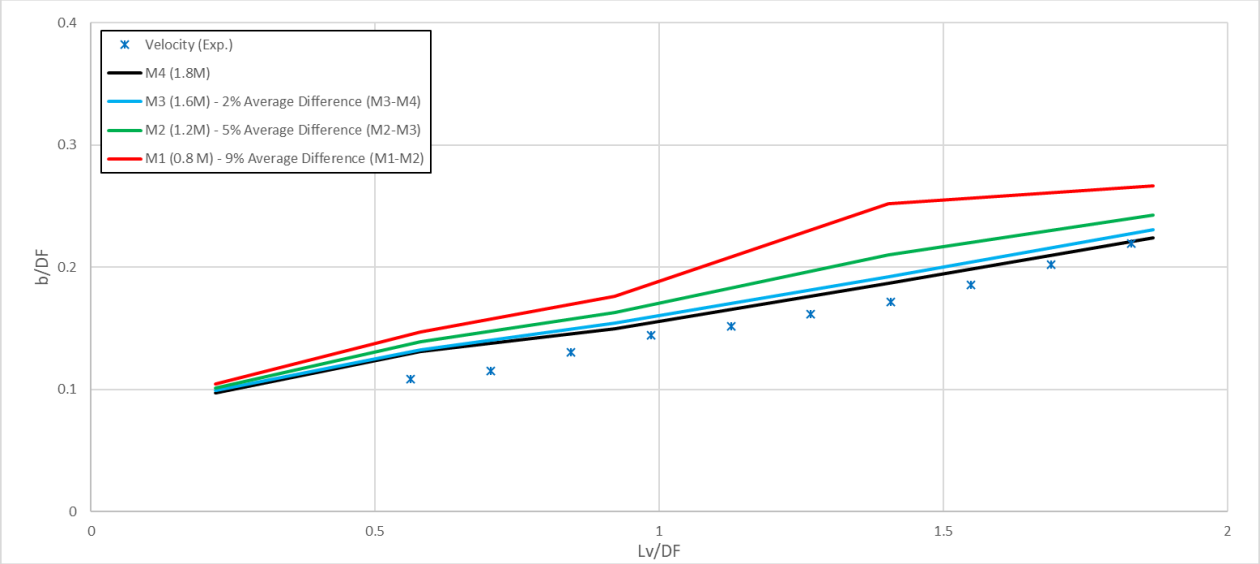

Figure 4.3: Mesh sensitivity results - velocity 1/e widths propagation for FSR (D5) using LRR turbulence model.

4.2.3 Turbulence Models

Five RANS turbulence models were used and their performance was investigated in this study: the realizable k-ε and k-ω SST models (known as two-equation turbulence models), the v2f (four equations to model anisotropic behavior), the LRR and the SSG (Speziale, Sarkar and Gatski) turbulence models (known as Reynolds stress models - six equations to model anisotropic behavior). It is important to note that the scalar fields (e.g., concentration) in shear flows such as inclined dense jets studied herein are anisotropic [20]. Moreover, experiments have found scalar anisotropy at both dissipation and inertial scales of the scalar fields [21]. This section summarizes the deriving equations of these turbulence models and Section 5 discusses further in this paper the performance of the turbulence models tested herein for the mixing of effluents in shallow waters.

Realizable k-ε Model

The realizable k-ε model is a widely used turbulence models in the k-ε family and was first proposed by [22]. This model exhibits two main differences from the standard k-ε model. It uses (i) a new equation for the turbulent viscosity, and (ii) the dissipation rate transport equation has been derived from the equation for the transport of the mean-squared vorticity fluctuation. The new turbulent viscosity equation is more robust compared to the other two-equations turbulence models. In reality, the properties of the turbulence are not similar along and across the jet,

especially at the shear surfaces of the jet-ambient boundary in the inclined dense jets, and the improvements in the realizable k-ε model help with predicting those parameters better. The form of the eddy viscosity equations is based on the realizability constraints; the positivity of normal Reynolds stresses and Schwarz's inequality for turbulent shear stresses which make the realizable k-ε model more precise than other k-ε models when predicting flows with complex secondary flow features. Transport equations for k and ε are:

$$\frac{\partial k}{\partial t} + \frac{\partial k u_i}{\partial x_i} = \frac{\partial}{\partial x_j}\left(Dk_{eff}\frac{\partial k}{\partial x_j}\right) + G_k - \varepsilon \tag{4.6}$$

$$\frac{\partial \varepsilon}{\partial t} + \frac{\partial \varepsilon u_i}{\partial x_i} = \frac{\partial}{\partial x_j}\left(D\varepsilon_{eff}\frac{\partial \varepsilon}{\partial xj}\right) + \sqrt{2}C_{\varepsilon 1}S_{ij}\varepsilon - C_{\varepsilon 2}\frac{\varepsilon^2}{k+\sqrt{\upsilon\varepsilon}} \tag{4.7}$$

where G_k represents the generation of turbulent kinetic energy due to the mean velocity gradients and Dk_{eff} and $D\varepsilon_{eff}$ are the effective diffusivity for k and ε, respectively. Their values are calculated as:

$$Dk_{eff} = \nu + \nu_t \tag{4.8}$$

$$D\varepsilon_{eff} = \nu + \frac{\nu_t}{\sigma_\varepsilon} \tag{4.9}$$

$$\upsilon_t = C_\mu \frac{k^2}{\varepsilon} \tag{4.10}$$

For more details on the model and $C_{\varepsilon 1}$, $C_{\varepsilon 2}$ and C_μ constants, the reader is referred to [22].

k-ω SST Model

The shear stress transport k-ω model has been developed by [23] using the standard k-ω model and a transformed k-ε model. The main difference of the k-ω SST model to the realizable k-ε model is the way in which the model calculates the turbulent viscosity to account for the transport of the principal turbulent shear stress. This model incorporates a cross diffusion term in the ω equation and a blending function to allow the proper calculation of the near wall and far field flow areas. The blending function triggers the standard k-ω model near wall regions, and of the standard k-ε model in areas away from the surface. The transport equations for k and ω are:

$$\frac{\partial k}{\partial t} + \frac{\partial k u_i}{\partial x_i} = \frac{\partial}{\partial x_j}\left(Dk_{eff}\frac{\partial k}{\partial x_j}\right) + G_k - \beta^* k\omega \tag{4.11}$$

$$\frac{\partial \omega}{\partial t} + \frac{\partial \omega u_i}{\partial x_i} = \frac{\partial}{\partial x_j}\left(D\omega_{eff}\frac{\partial \omega}{\partial x_j}\right) + 2\gamma S_{ij} - \beta\omega^2 + (1 - F_1)CD_{k\omega} \tag{4.12}$$

For the description and values of the G_k, Dk_{eff}, $D\omega_{eff}$, β, γ, S_{ij}, F_1, C, $D_{k\omega}$ parameters as well as of all model constants, the reader is referred to [23].

v2f (v^2-f) Model

The v2f model, which is based on k-ε-v^2 model of [24], is a four-equation model that includes turbulence kinetic energy (k), its dissipation rate (ε), a velocity variance (v^2) and a relaxation factor (f). This model is similar to the k-ε family of turbulence models with added features of turbulence anisotropy and pressure-strain effects. Therefore, it can be considered as a model whose characteristics place it in between k-ε models and Reynolds stress models. In this model, the velocity scale (v^2) is used instead of the kinetic energy, k, to estimate the eddy viscosity. K, ε, v^2 and f are obtained from the following transport equations:

$$\frac{\partial k}{\partial t} + \frac{\partial k u_i}{\partial x_i} = P - \varepsilon + \frac{\partial}{\partial x_j}(D k_{eff} \frac{\partial k}{\partial x_j}) + S_k \tag{4.13}$$

$$\frac{\partial \varepsilon}{\partial t} + \frac{\partial \varepsilon u_i}{\partial x_i} = \frac{C'_{\varepsilon 1} P - C_{\varepsilon 2} \varepsilon}{T} \frac{\partial}{\partial x_j}(D \varepsilon_{eff} \frac{\partial \varepsilon}{\partial x_j}) + S_\varepsilon \tag{4.14}$$

$$\frac{\partial \overline{V^2}}{\partial t} + \frac{\partial \overline{V^2} u_i}{\partial x_i} = kf - 6\overline{V^2} \frac{\varepsilon}{k} \frac{\partial}{\partial x_j}(D k_{eff} \frac{\partial \overline{V^2}}{\partial x_j}) + S_{\overline{V^2}} \tag{4.15}$$

$$f - L^2 \frac{\partial^2 f}{\partial {x_i}^2} = (C_1 - 1) \frac{\frac{2}{3} - \frac{\overline{V^2}}{k}}{T} + C_2 \frac{P}{k} + \frac{5\overline{V^2}/k}{T}) + S_f \tag{4.16}$$

where T and L are turbulent time and length scale, respectively; C_1, C_2, $C_{\varepsilon 1}$, $C'_{\varepsilon 1}$ and $C_{\varepsilon 2}$ are constants and S_k, S_ε, $S_{\overline{V^2}}$ and S_f are user-defined source terms. Variable f is the solution for Eqn. 16. The v2F model uses the elliptic operator to compute a term analogous to the pressure-strain correlation of the Reynolds stress model. The reader is referred to [24] for further details on the v2f model.

Reynolds Stress Models (LRR and SSG)

The Reynolds Stress Models (RSMs) or sometimes termed as the Reynolds Stress Turbulence Models (RSTMs) are among the most complete turbulence models for the RANS system which are available within OpenFOAM. RSMs' concept is different from the isotropic eddy-viscosity hypothesis as it closes the RANS equations by solving the transport equations for the Reynolds stresses, as well as an equation for the dissipation rate. Therefore, in the case of three-dimensional flows, seven additional transport equations are required (i.e., six equations for Reynolds stresses and an additional one for the dissipation rate). The exact transport equations for the transport of the Reynolds stresses, $\rho \overline{u'_i u'_j}$, can be written as:

Local Time Derivative + Convection (C_{ij}) = - Turbulent Diffusion ($D_{T,ij}$) + Molecular Diffusion ($D_{L,ij}$) - Stress Production (P_{ij}) - Buoyancy Production (G_{ij}) + Pressure strain (ϕ_{ij}) - Dissipation (ε_{ij}) - Production by System Rotation (F_{ij}) + User Defined Source Term

Its mathematical representation is:

$$\frac{\partial}{\partial t}\left(\rho\overline{u_i'u_j'}\right)+\frac{\partial}{\partial x_k}\left(\rho u_k\overline{u_i'u_j'}\right)=-\frac{\partial}{\partial x_k}\left(\rho\overline{u_i'u_j'u_k'}+\overline{p(\delta_{kj}u_i'+\delta_{ik}u_j')}\right)+\frac{\partial}{\partial x_k}\left(\mu\frac{\partial}{\partial x_k}\left(\overline{u_i'u_j'}\right)\right)$$
$$-\rho\left(\overline{u_i'u_k'}\frac{\partial u_j}{\partial x_k}+\overline{u_j'u_k'}\frac{\partial u_i}{\partial x_k}\right)-\rho\beta\left(g_i\overline{u_j'\theta}+g_j\overline{u_i'\theta}\right)+\overline{p\left(\frac{\partial u_i'}{\partial x_j}+\frac{\partial u_j'}{\partial x_i}\right)}-2\mu\overline{\frac{\partial u_i'}{\partial x_k}\frac{\partial u_j'}{\partial x_k}}$$
$$-2\rho\Omega_k\left(\overline{u_j'u_m'}\varepsilon_{ikm}+\overline{u_i'u_m'}\varepsilon_{jkm}\right)+Source \tag{4.17}$$

Parameters C_{ij}, $D_{L,ij}$, P_{ij}, and F_{ij} do not need to be modelled, because they do not include higher order correlations such as $\overline{u_i'u_j'u_k'}$, whereas $D_{T,ij}$, G_{ij}, ϕ_{ij}, and ε_{ij} require modelling in order to close the equation, because they include additional unknows.

Among all the terms above, only the buoyancy production equations are presented below due to their importance in dense effluent discharge modelling:

$$G_{ij}=-\rho\beta(g_i\overline{u_j'\theta}+g_j\overline{u_i'\theta}) \tag{4.18}$$

$$\overline{u_i'\theta}=\frac{\mu_t}{Pr_t}\left(\frac{\partial T}{\partial x_i}\right) \tag{4.19}$$

where Pr_t is the turbulent Prandtl number for the flow energy with a value of 0.85 set as default in OpenFOAM model.

The RSMs do not always generate better results compared to simpler turbulence models for all applications. However, for the effluent discharge mixing application, in which the problem includes modelling the streamline curvature and jet anisotropy in the Reynolds stresses, RSMs' equations are good candidates to consider. Two different RSMs were used in OpenFOAM for this study: the Launder-Reece-Rodi (LRR) model which was developed by [25] and the Speziale-Sarkar-Gatski (SSG) model developed by [26]. The difference between the LRR and SSG turbulence models is due to how they model the terms including unknows in Eqn. 17. For instance, SSG turbulence model uses an invariant dynamical systems approach to model the pressure-strain correlation of turbulence.

4.3 Numerical Experiment Cases

The simulation cases employed in this study were selected based on the experiments conducted by [1]. Two discharge angles (30° and 45°) were selected and three regimes (FSR, PCR and CIR) were considered for each discharge angle. Finally, five different turbulence models were applied to each case. This resulted in 2×3×5=30 simulation cases. Table 4.1 and Table 4.2 present the parameters used in the numerical experiment cases studied herein.

4.4 Results and Discussion

4.4.1 Mixing Regimes

The time-averaged normalized concentration maps (C/C_0; where C is concentration at each numerical cell and C_0 is the discharge concentration) for 30° discharges, and all turbulence models, are shown in Figure 4.4. The three regimes introduced by [1] can be observed in these figures. When the densimetric Froude number F, Eqn. 20, is relatively small with large water depth H, a full submergence regime (FSR) for dense jet discharge could be achieved (Figure 4.4a-e).

$$F = \frac{U_0}{\sqrt{\frac{\rho_0 - \rho_a}{\rho_a} g D}} \tag{4.20}$$

As F increases, the upper half of the discharge plume impacts the water surface and water entrainment is only limited to the ambient water beneath of the jet. This results in the plume contact regime (PCR) shown in Figure 4.4f-j. With further increase of F, the limitation of water depth becomes more prominent and the jet centerline directly impinges the water surface. This results in the centerline impingement regime (CIR) as shown in Figure 4.4k-o. In the PCR and CIR regimes, the jet attaches to the surface and moves downstream due to the initial momentum of the discharge and then eventually descends when the negative buoyancy forces overcome the initial momentum forces.

4.4.2 Flow Characteristics

For the numerical cases investigated, five to seven cross sections were considered (depending on the regime) which are selected such that they are perpendicular to the jet trajectory to extract data related to the velocity and concentration distribution along the jet width. The nondimensional streamwise distance, Lv/D (Lv is distance along the jet centerline and D is the

nozzle diameter), is used to indicate the distance along the jet centerline at the central plane. Figure 4.5 shows the location of these cross sections for the LRR turbulence model. From this point onwards, for the sake of readability of the numerical result plots and for brevity, only the LRR and v2f turbulence model results are plotted and results from other models will only be summarized in tables. The last horizontal line shown in Figure 4.5 is used for quantifying the return point location and dilution at this point. The red line in Figure 4.5 represents the jet centerline which was defined by connecting the maximum velocity values on each cross section. In some studies, the jet centerline might be defined based on the maximum concentration, but the maximum velocity was adopted in this study based on [1].

Table 4.1: Numerical experiment parameters and results for 30° discharge case

Jet Properties									Return Point Results			
ID		θ (°)	D (mm)	U_0 (m/s)	Δρ/ρa (%)	F	H/D	F/(H/D)	Sr	Sr/(H/D)	Xr/D	Xr/D(H/D)
C3 (Full Submerged Regime - FSR)	[1]	30	6	0.58	1.99	17	20	0.85	18.0	0.90	49.0	2.45
	LRR								17.9	0.89	50.5	2.52
	SSG								17.2	0.86	56.9	2.84
	v2f								16.4	0.82	40.6	2.03
	Realizable k-ε								17.2	0.86	52.3	2.61
	k-ω SST								13.3	0.67	36.9	1.84
C6 (Plume Contact Regime - PCR)	[1]	30	6	0.92	2.00	27	20	1.35	17.7	0.884	84.5	4.23
	LRR								17.5	0.88	80.0	4.00
	SSG								16.4	0.82	81.7	4.08
	v2f								15.2	0.76	73.3	3.67
	Realizable k-ε								18.5	0.93	81.7	4.08
	k-ω SST								14.3	0.71	60.0	3.00
C8 (Centerline Impingement Regime - CIR)	[1]	30	6	1.10	2.03	32	20	1.60	17.2	0.862	140	7.02
	LRR								20.0	1.00	108.3	5.42
	SSG								20.4	1.02	108.3	5.42
	v2f								18.2	0.91	95.0	4.75
	Realizable k-ε								20.8	1.04	98.3	4.92
	k-ω SST								17.5	0.88	70.0	3.50

Table 4.2: Numerical experiment parameters and results for 45° discharge case

Jet Properties									Return Point Results			
ID		**θ (°)**	**D (mm)**	**U_0 (m/s)**	**$\Delta\varrho/\varrho a$ (%)**	**F**	**H/D**	**F/(H/D)**	**Sr**	**Sr/(H/D)**	**Xr/D**	**Xr/D(H/D)**
D5 (Full Submerged Regime - FSR)	[1]	45	6	0.78	2.11	22.3	40	0.56	23.8	0.595	66.7	1.67
	LRR								24.4	0.61	68.3	1.71
	SSG								22.7	0.57	70.0	1.75
	v2f								20.0	0.50	63.3	1.58
	Realizable k-ε								23.3	0.58	71.7	1.79
	k-ω SST								19.2	0.48	56.7	1.42
D8 (Plume Contact Regime - PCR)	[1]	45	6	1.05	2.11	29.9	40	0.75	25.6	0.641	118	2.96
	LRR								26.3	0.66	111.7	2.79
	SSG								25.0	0.63	110.0	2.75
	v2f								22.7	0.57	105.0	2.63
	Realizable k-ε								26.3	0.66	111.7	2.79
	k-ω SST								23.8	0.60	100.0	2.50
D11 (Centerline Impingement Regime - CIR)	[1]	45	6	1.22	2.10	34.8	40	0.87	23.4	0.584	-	-
	LRR								23.8	0.60	118.3	2.96
	SSG								24.4	0.61	113.3	2.83
	v2f								22.7	0.57	108.3	2.71
	Realizable k-ε								23.3	0.58	115.0	2.88
	k-ω SST								2.2	0.06	105.0	2.63

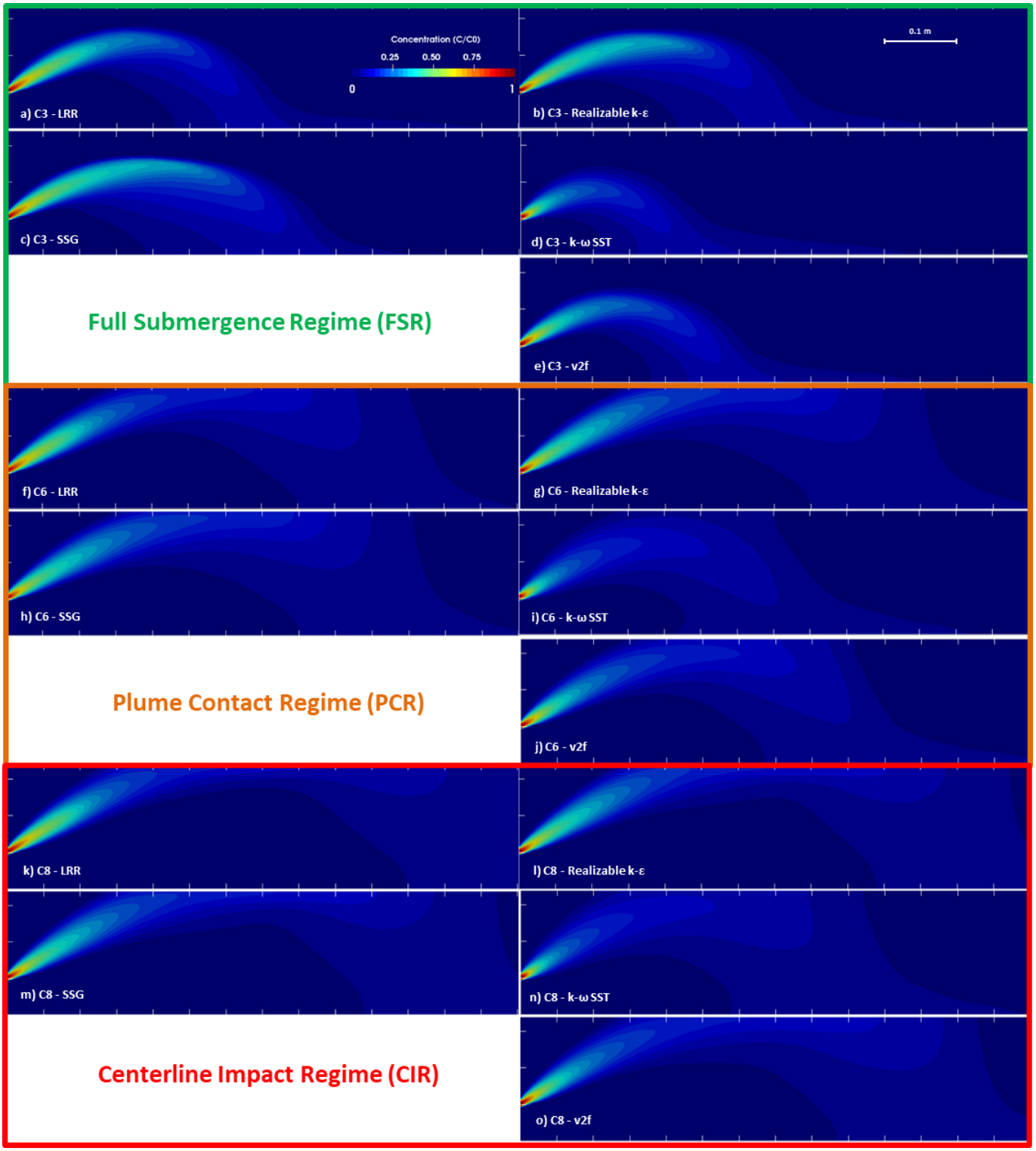

Figure 4.4: Mixing regimes of the 30° inclined dense jets in shallow ambient water: a) FSR – LRR; b) FSR – realizable k-ε; c) FSR – SSG; d) FSR – k-ω SST; e) FSR – v2f; f) PCR – LRR; g) PCR – realizable k-ε; h) PCR – SSG; i) PCR – k-ω SST; j) PCR – v2f; k) CIR – LRR; l) CIR – realizable k-ε; m) CIR – SSG; n) CIR – k-ω SST; o) CIR – v2f. For details of each case refer to Table 4.1.

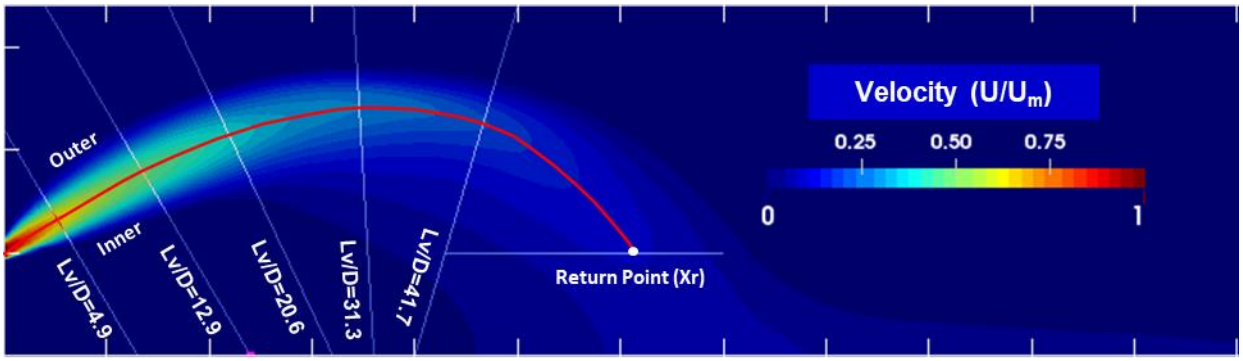

Figure 4.5: Full Submergence Regime (SFR) of a 30° discharge (C3) with cross section alignments used to extract discharge velocity and concentration – LRR model. The red line represents the jet centerline.

Figure 4.6 plots the outer jet boundaries and centerline of the FSR jets resulted from LRR and v2f turbulence models for a 30° discharge. Note that $C=0.03C_0$ (i.e., 3% of maximum concentration at the source) was used to delineate the jet outer boundary in the numerical results. The outline from experiment is for a different case with different F and is presented for a qualitative comparison only. For all three regimes (i.e., FSR, PCR and CIR), the jet starts with a dominant momentum force (this area was named "initial stage" as per [1]). The momentum force reduces as jet height increases and, at the maximum jet rise height, the buoyancy forces dominate the flow and the negative buoyancy causes the jet to sink back. Surface attachment will further reduce the upward momentum and thus the initial stage becomes shorter and this is followed by an "attachment stage" ([1]). The difference in the centerlines separately obtained from the LRR and the v2f models are shown in Figure 4.6. This highlights the importance of evaluating the effect of using different turbulence models in effluent discharge modelling. This aspect is further discussed in Section 4.5.

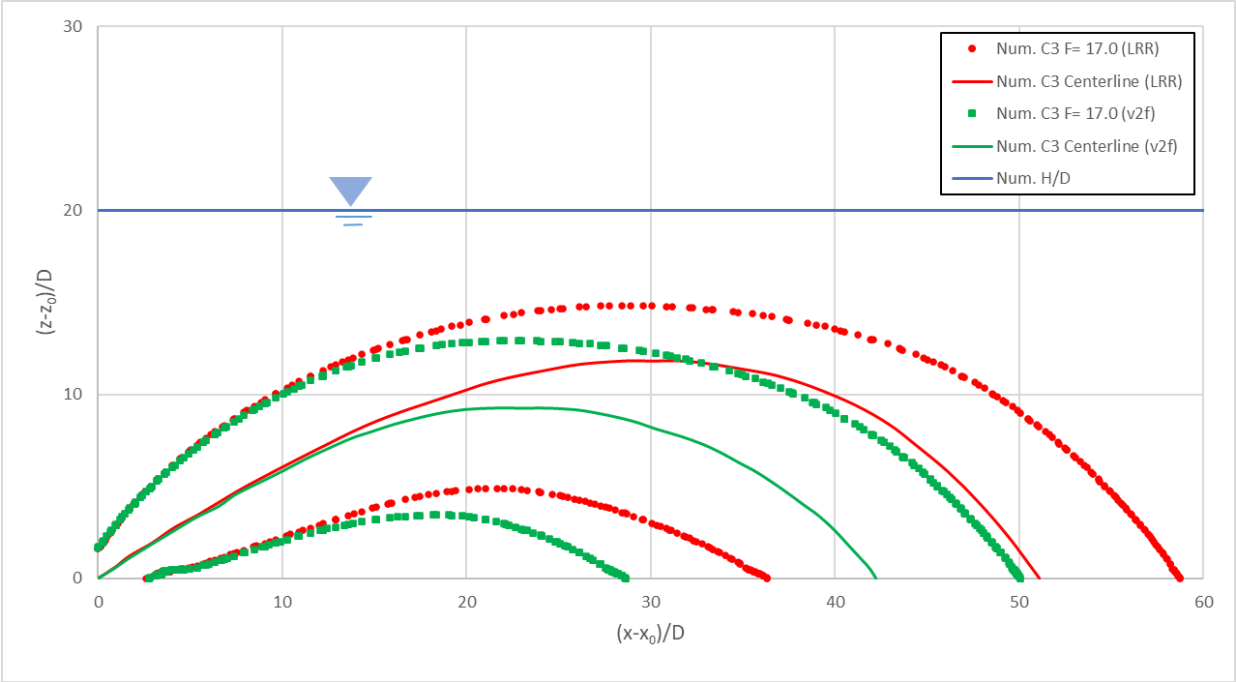

Figure 4.6: Comparison of jet boundaries of a 30° discharge in FSR using the of LRR and v2f models with an experimental case from [1].

Full Submergence Regime (FSR)

Figure 4.4 and Figure 4.5 show the flow pattern of the effluent discharge in the FSR. Flow pattern could be divided in inner half and outer half by the jet centerline (i.e., the locus of maximum jet velocity) as shown in Figure 4.5. The cross-sectional axial velocity for an inclined dense jet can be approximated by a Gaussian profile described as:

$$U = U_m e^{-(\frac{r}{b})^2} \tag{4.21}$$

where U_m is maximum streamwise velocity at a cross section; r is radial distance and b is velocity 1/e width where the jet velocity decreases to 1/e of the maximum velocity on the cross section (e is the Naperian number which is 2.718). It is noteworthy that b is not viable for the PCR and CIR and is only applicable to the FSR. The numerical results of the LRR and the v2f models are compared to those experimentally obtained by [1] for the nondimensional cross sectional distribution of U/U_m at five Lv/D locations and are presented in Figure 4.7. As reported in previous experimental and numerical studies on inclined dense jets (e.g., [5, 27]), the outer half of the jet is more consistent with a Gaussian profile, while a larger distortion is observed in the inner half of the jet with a larger rate of spreading. The transversal jet cross-sections on numerical results have

an average distance of ~8D from each other and larger gap between two neighboring profiles would suggest a larger distortion rate in inner half of the jet.

Similar to the experimental work of [1], the largest velocity internal asymmetry identified in this study occurred at an *Lv*/*D* which is the closest cross section to the jet terminal rise location where the vertical velocity is minimum. This is in fact the line along which the buoyancy-induced instability seems to be perpendicular to the flow direction. Discrepancies between the numerical and the experimental results, mainly overpredicting the velocity spread by numerical results, could be attributed to the inaccuracy of RANS models to properly capture the internal detrainment.

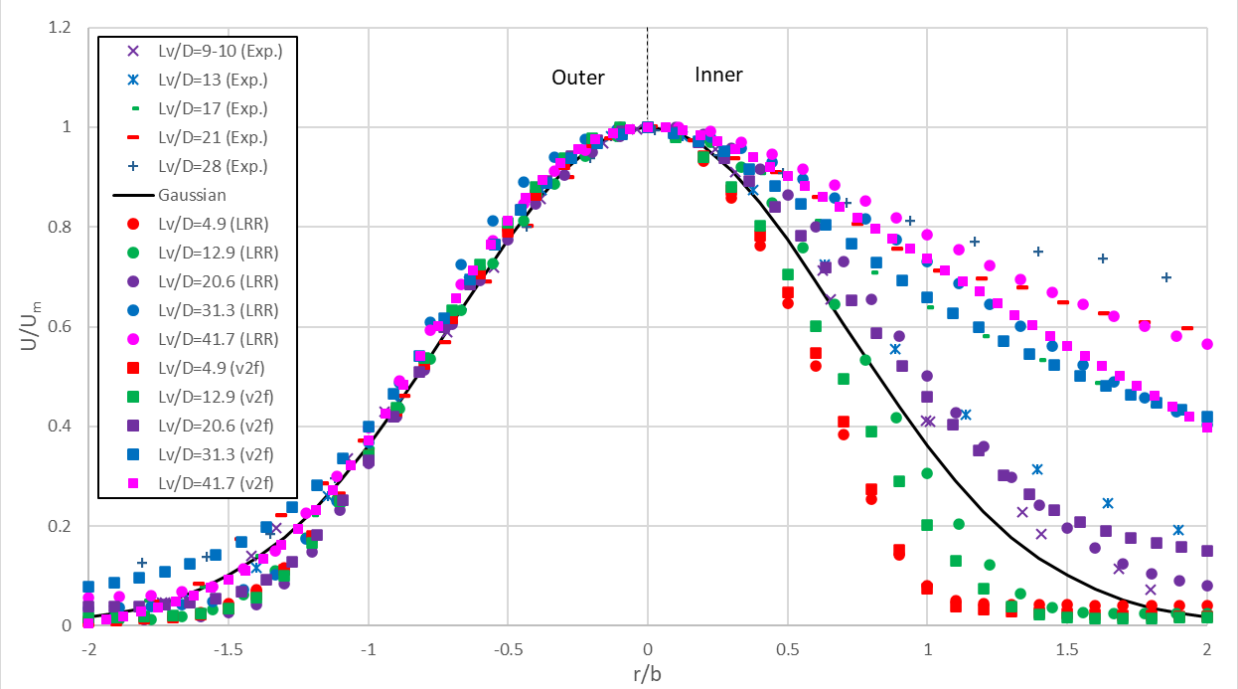

Figure 4.7: Nondimensional velocity profiles at different downstream cross sections for a 45° discharge (D5) using LRR and v2f turbulence models in FSR. Experimental results are from [1].

Plume Contact Regime (PCR) and Centerline Impingement Regime (CIR)

The general flow patterns for PCR and CIR for a 30° jet are shown in Figure 4.4. [1] proposed defining five regions for PCR and CIR: the initial stage (immediately after the discharge point where momentum forces are dominant), the attachment stage (where jet centerline attaches to the water surface, in CIR) and the developed stage (where jet centerline detaches from the water surface, in CIR, and sinks due to strong buoyancy forces) with two transition stages between them. These are shown in Figure 4.8. The nondimensional cross sectional distribution of the

velocity in the PCR and CIR scenarios follows similar patterns as the FSR scenario in the initial stage where buoyancy-induced distortions would result in wider spread in the inner half of the jet (Figure 4.9a, only PCR). The numerical results from LRR and v2f model show similar patterns as experimental data by [1].

In the attachment stage, the velocity *1/e* width could not be identified and, thus, *r/D* was used instead of *r/b* for the horizontal axis to plot the nondimensional cross sectional distribution of velocity in PCR and CIR. The numerical results (LRR and v2f models) are compared to those from the experiment [1] for this stage in Figure 4.9b for PCR (results of CIR follow the same pattern as PCR and, thus, not shown here). The difference between PCR and CIR in the attachment stage is that the maximum velocity will occur below the water surface for the PCR and at the water surface for the CIR. [1] proposed Eqn. 22 for a distorted Gaussian profile for the attachment stage of a PCR that is plotted in Figure 4.9b.

$$\frac{U}{U_m} = 0.67e^{-(\frac{r}{2D})^2} + 0.33 \tag{4.22}$$

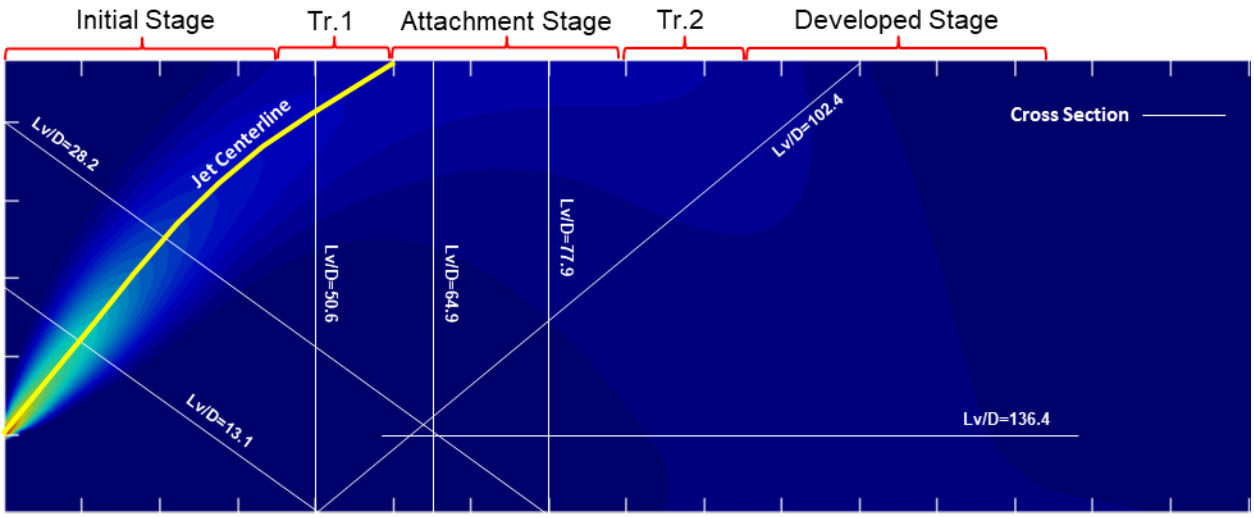

Figure 4.8: CIR of a 45° discharge (D11, LRR model) with cross section alignments used to extract velocity and concentration.

Finally, for the developed stage, the outer half of jets for all numerical models do match better the Gaussian profile compared to the inner half. For the inner half, the jets stabilized as shown in Figure 4.9c for PCR. This stabilization means that the jet discharge reaches a fully developed stage with symmetrical and self-similarity jet spreading. The numerical results from LRR and v2f turbulence models are relatively close, with slightly higher values for the v2f turbulence model.

Shear stress forces on a turbulent jet impact the velocity and its spread along the jet trajectory which might have contributed to the different results between the turbulence models applied here.

4.4.3 Jet Concentration Spread

Jet spread rate in inclined dense jet discharges is usually quantified using either the velocity or concentration 1/e widths. The FSR case was used to quantify the jet spread, as used in [1]. Nondimensional velocity profiles for a 45° discharge were plotted in Figure 4.7 earlier. Similar analysis was performed for nondimensional concentration profiles, as presented in Figure 4.10. Comparing the latter to velocity profiles in Figure 4.7, it was observed that for the areas that buoyancy forces dominate the plume (i.e. descending section of the jet), the deviation from Gaussian profile is larger in the concentration profiles compared to those of velocity profiles, in the inner half of the jet. This is attributed to larger effect of buoyancy distortion on the concentration rather than velocity.

For the five cross sections used in Figure 4.7 and Figure 4.10, the locations of the velocity and concentration 1/e widths were normalized with the nozzle diameter plotted against the distance along the jet centerline as shown in Figure 4.11 for FSR. The differences between the numerical results and experimental data are because of the cases considered (i.e. different Froude numbers). Values calculated by the LRR model were consistently higher for both the concentration and velocity spread widths. This is assumed to be due to the capability of the LRR model to capture anisotropies in the jet, especially due to the pressure differences at the jet boundaries similar to that reported in [5]. However, milder slopes observed in the numerical results compared to those from experimental data suggests slightly lower rates of spread for jet velocity and concentration.

4.4.4 Velocity Decay

The magnitude of both the axial and vertical velocity were evaluated to quantify the velocity decay of the inclined dense jet. Similar to previous sections, from all models studied herein, only the LRR and v2f models are presented in the graph forms for the sake of brevity. However, unlike previous plots, all three regimes' (FSR, PCR and CIR) values are presented. Maximum vertical velocity values at each cross section were extracted and plotted against the axial location of the

cross sections along the jet centerline as shown in Figure 4.12. As expected, the maximum vertical velocity decreases until the jet reaches its maximum height at which point the negative buoyancy causes the jet to sink downward. Maximum vertical velocity will then increase again while jet is descending toward the bed. A steep decline is observed in the CIR around Lv/D=45 and that is due to the surface impingement of the jet. Numerical results show a similar pattern as the experimental ones (even though the Froude numbers are different) of [1]. LRR model values are slightly higher than the v2f model. Given the longer distance of return point resulted from the LRR turbulence model than v2f turbulence model for all cases studied, the higher maximum vertical velocity in the LRR turbulence model seems to be reasonable. Since there is a better agreement between the geometrical properties of LRR turbulence model with experimental data from [1] when comparing to the v2f turbulence model (Table 1 and Table 2), one can conclude that the maximum vertical and axial velocity results from LRR turbulence model are more reliable than the v2f model.

Maximum axial velocity decay is plotted in Figure 4.13 where it shows a constant decrease in velocity for FSR for both the LRR and v2f models. This is consistent with the behavior observed in the experimental study of [1]. The velocity magnitude, observed in [1], remained almost constant for the PCR when it impinged the water surface and it increased slightly in the CIR before it continued to decrease again. The numerical results could not reproduce the increase in the axial velocity in the impinging region for the CIR. [1] argued that this velocity increase could be due to the change in the jet cross sectional area as it impinges the water surface (i.e., a decrease of the jet cross sectional area at the surface impingement point and, thus, an increase in the velocity). Both LRR and v2f models show an approximately constant axial velocity in the impingement region. This could be because the numerical model did not capture the change in the cross sectional area of the impinging jet discussed in [1].

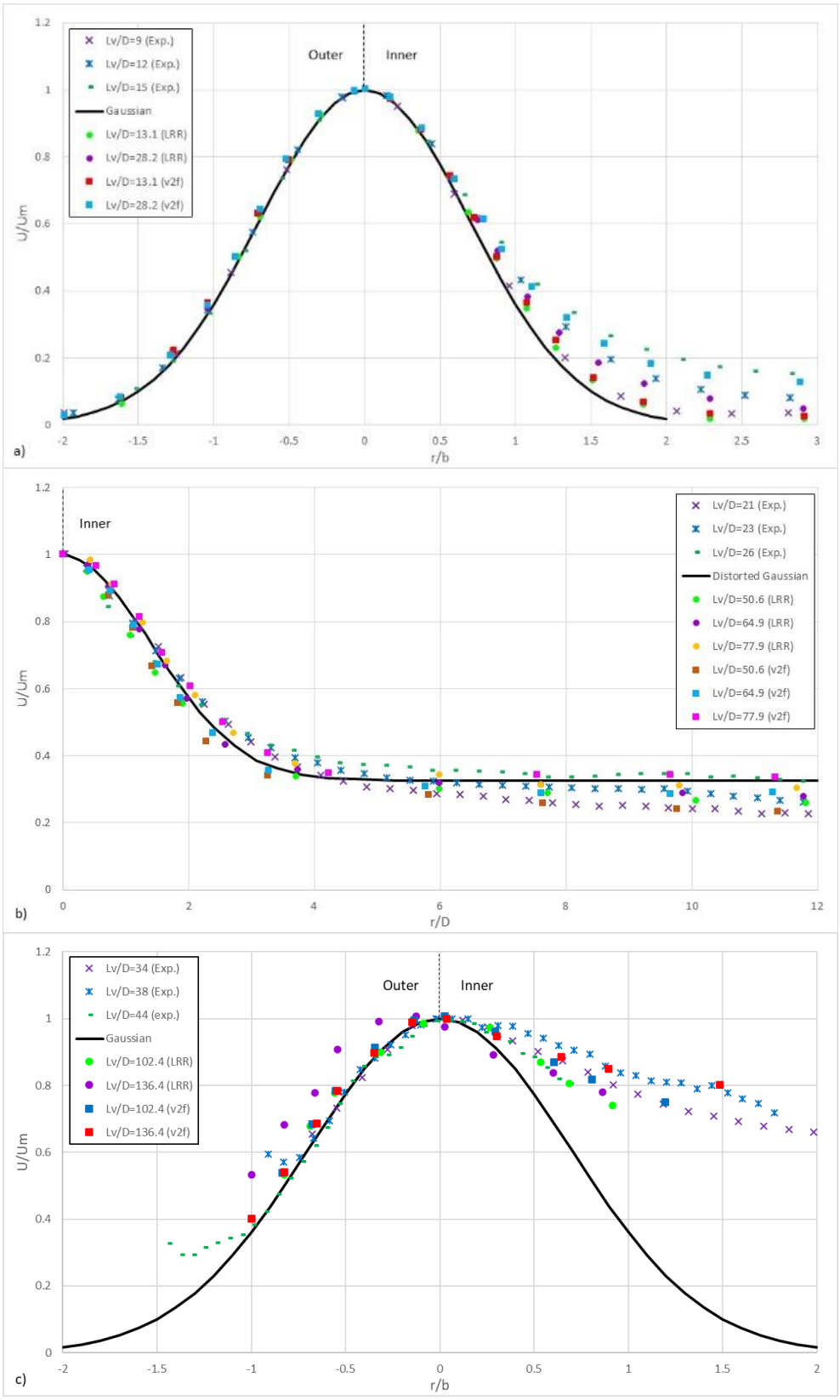

Figure 4.9: Nondimensional velocity profiles at different downstream cross sections for a 45° discharge using LRR and v2f turbulence models in PCR; a) initial stage, b) attachment stage and c) developed stage.

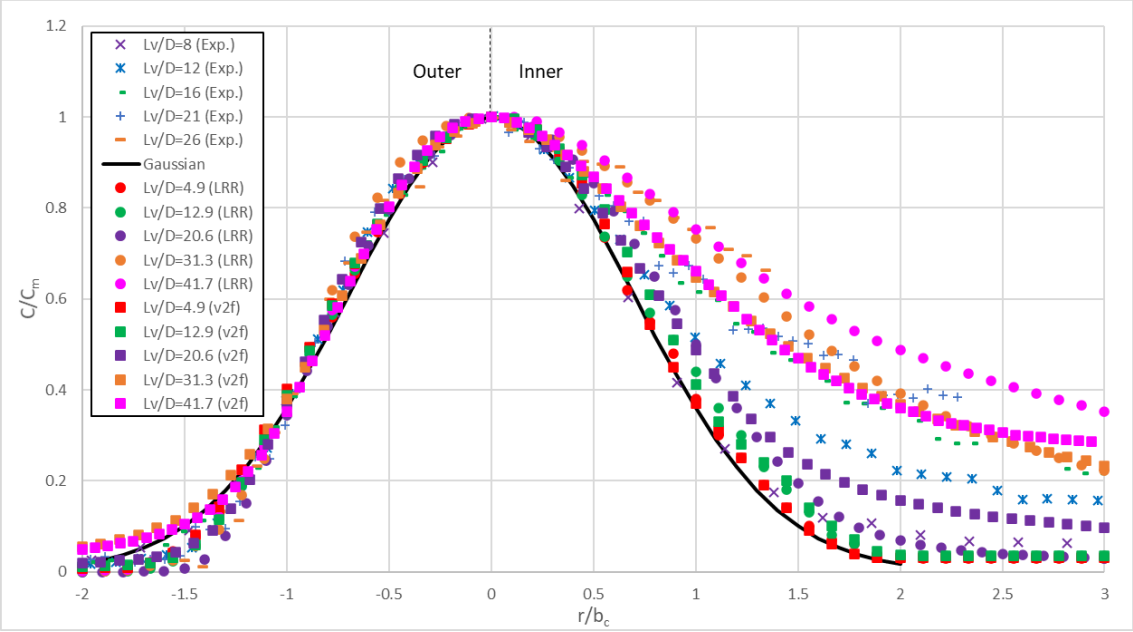

Figure 4.10: Nondimensional concentration profiles at different downstream cross sections for a 45° discharge (D5) in FSR with F=22.3. Experimental case is from Jiang et al. (2014) with F=7.1.

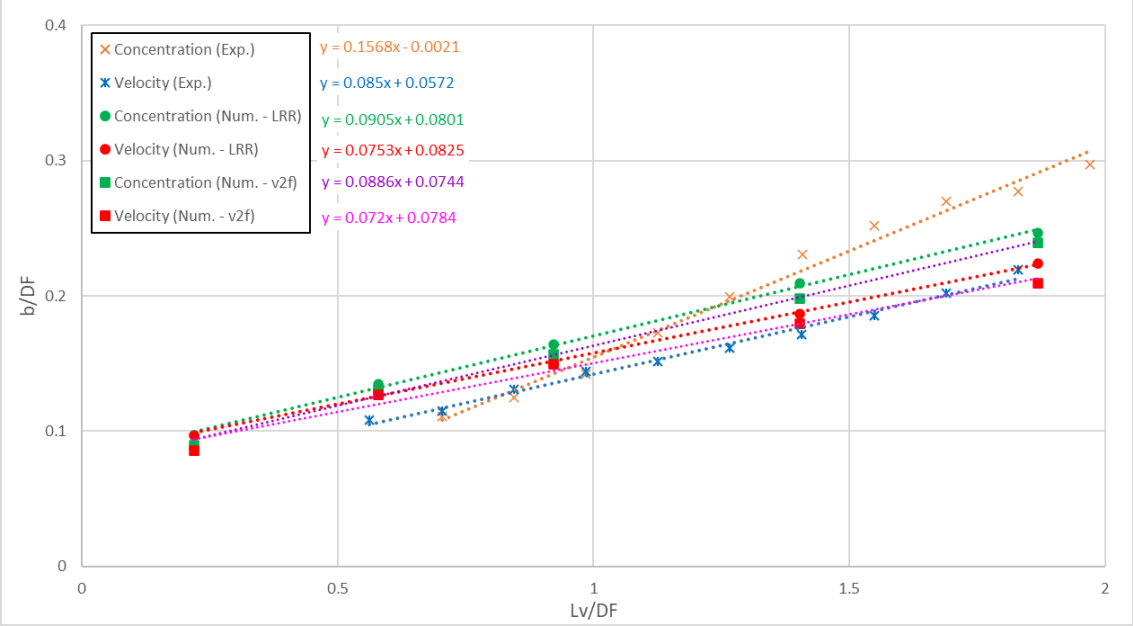

Figure 4.11: Velocity and concentration 1/e widths propagation for FSR (D5). Experimental case is from Jiang et al. (2014).

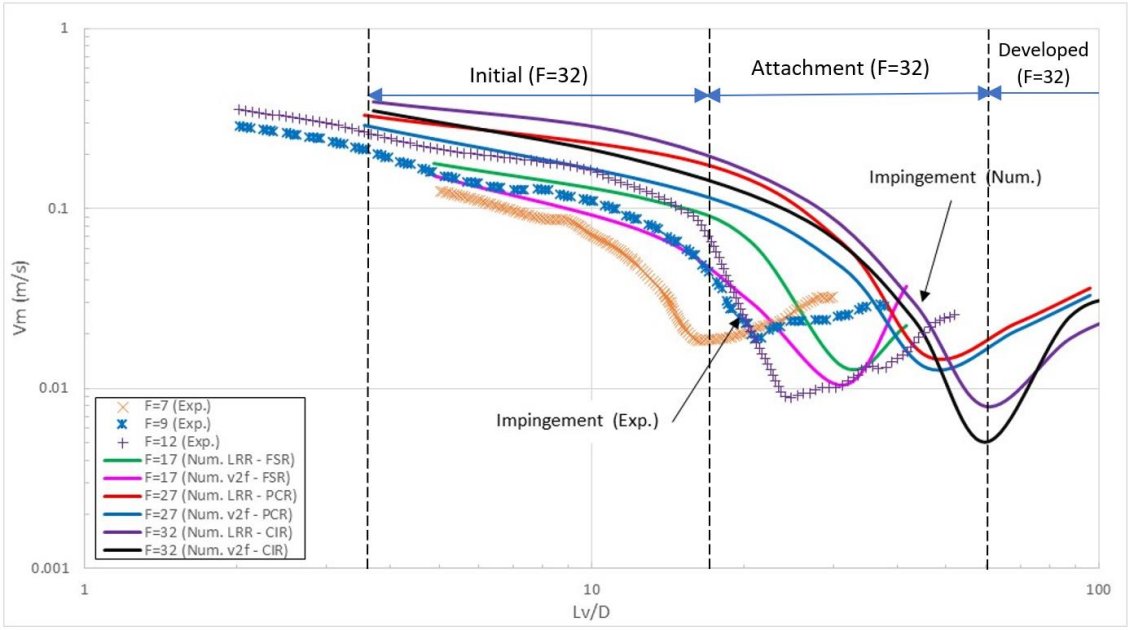

Figure 4.12: Maximum vertical velocity propagation along the jet trajectory at the central plain for the 30° discharge cases (C3, C6 and C8).

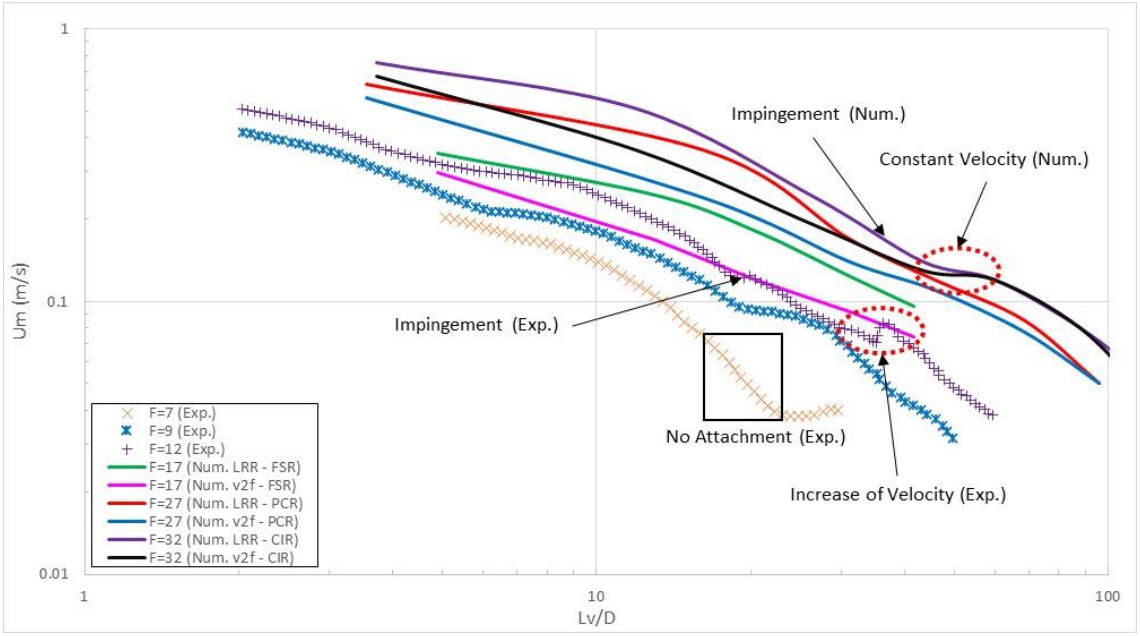

Figure 4.13: Maximum axial velocity decay along the jet trajectory at the central plain for 30° discharge cases (C3, C6 and C8).

4.4.5 Surface Impingement Dilution and Location

Minimum Surface Dilution

Minimum Surface Dilution (S_s) could be nondimensionalized by H/D, where H is the water depth above the nozzle, for similar $\Delta\rho/\rho_0$. This was found to be an appropriate nondimensionalization parameter for shallow waters [1]. Discharge Froude number F is also known to be suitable for nondimensionalization of dilution [8]. Froude number F was normalized by H/D [1, 8]. The normalized $S_s/(H/D)$ versus $F/(H/D)$ for the 30° and 45° discharge angles are plotted in Figure 4.14 and Figure 4.15, respectively. The minimum surface dilution results are divided into three regimes (FSR, PCR and CIR). For the FSR condition, the jet terminal rise does not interact with the water surface and thus the dilution would approach infinity, theoretically. As the Froude number increases, the outer half of the jet starts reaching the water surface (i.e. the PCR) and causes a drop in dilution. When F is sufficiently large, the jet transforms into a CIR and the dilution reaches its minimum in the attachment zone and $S_s/(H/D)$ becomes constant in the asymptotic range of high $F/(H/D)$ values. In the attachment zone, the jet behaves like a wall jet where the water entrainment is restricted from top of the jet toward its centerline. This causes a decrease in the dilution rate compared to that of a free jet. Numerical results show good agreement with the experimental data for LRR and v2f models, for both the 30° and 45° jets. The average differences between numerical results and experimental data are +4% and -7% for the LRR and v2f turbulence models, respectively, for 45° discharges.

The transitional lines for $F/(H/D)$ were identified by [1] to distinguish the three jet regimes. The normalized $F/(H/D)$ values for both 30° and 45° discharge angles in numerical cases ($F/(H/D)$ value is the same for all turbulence models in each regime) are provided in Table 4.3. The values are within the range proposed by [1] which confirms that the modelled jets fall within the correct classification for each $F/(H/D)$. There has not been any discussion on the waves generated due to impingement of the discharge into the water surface in the experimental studies. Waves may not happen in the PCR, but they may emerge in the CIR if $F/(H/D)$ is much larger than 1.4 and 0.77 for the 30° and 45° discharge angles, respectively. A parametric study using a volume of fluid (VOF) model is able to quantify this, but it is not the scope of the current study.

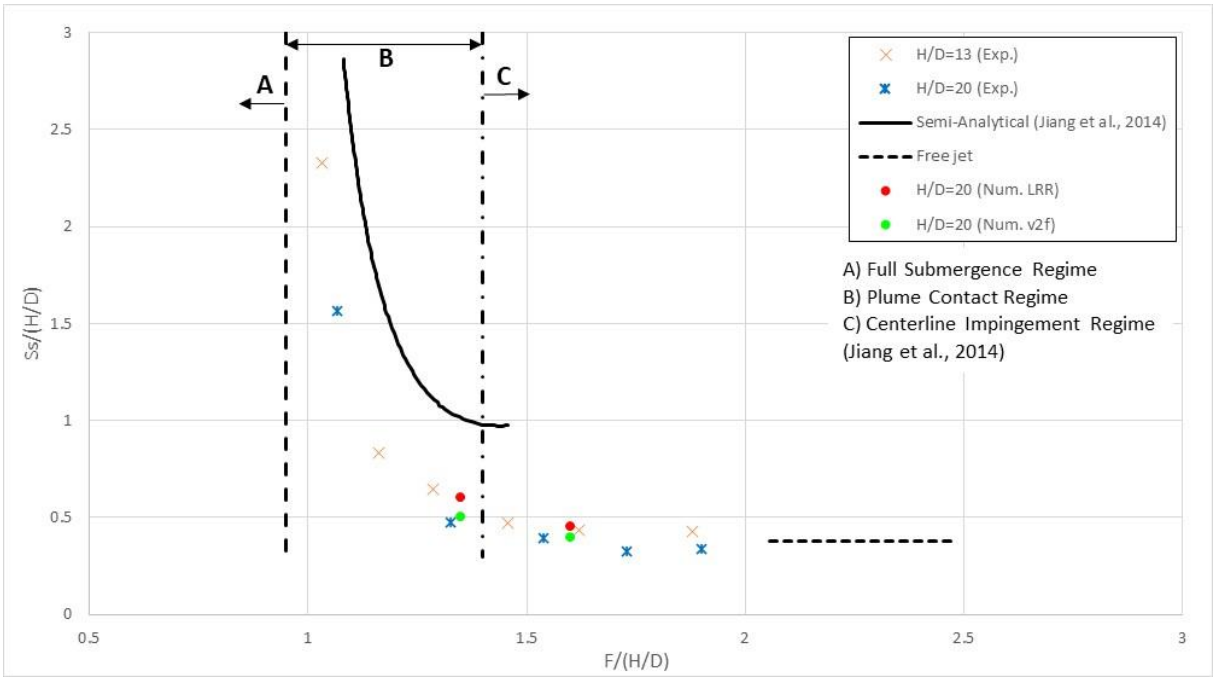

Figure 4.14: Normalized minimum surface dilution versus normalized F for 30° discharge.

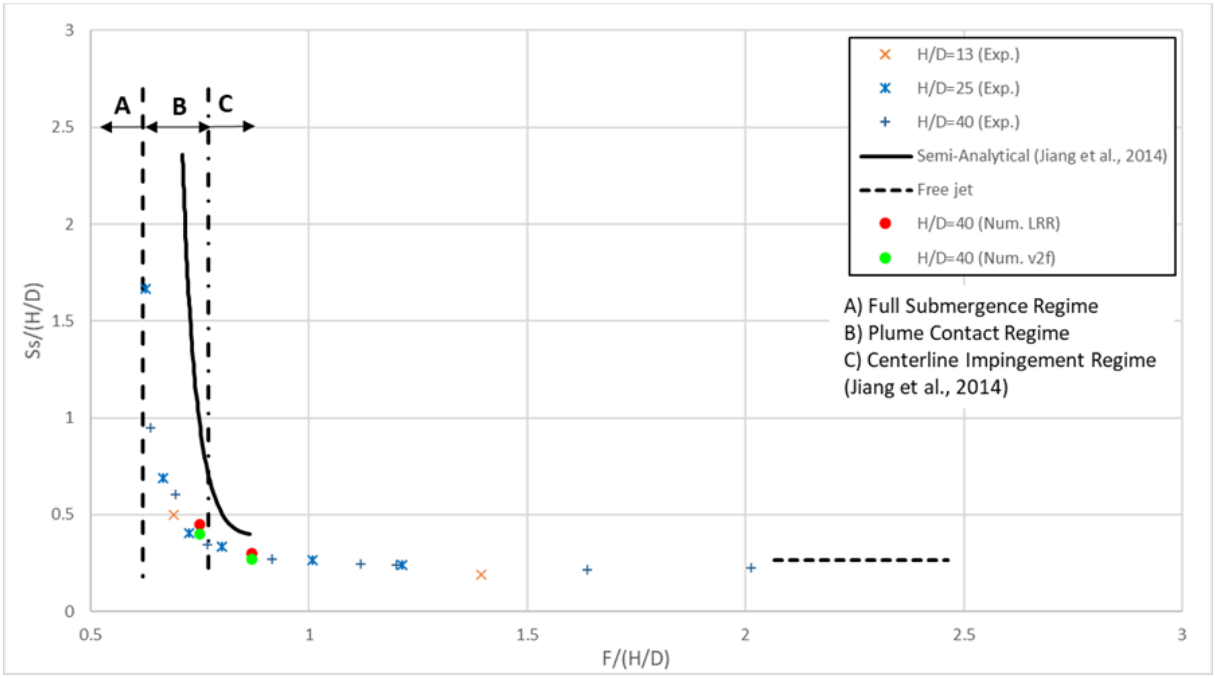

Figure 4.15: Normalized minimum surface dilution versus normalized F° for 45° discharge.

Table 4.3: Comparison of numerical (this study) and experimental [1] regime transition values for the 30° and 45° discharges.

Regime	Experimental [1]		Numerical	
	30°	**45°**	**30°**	**45°**
FSR	$F.D/H < 0.95$	$F.D/H < 0.62$	0.85	0.56
PCR	$0.95 \leq F.D/H < 1.4$	$0.62 \leq F.D/H < 0.77$	1.35	0.75
CIR	$F.D/H \geq 1.4$	$F.D/H \geq 0.77$	1.60	0.87

Horizontal Location of Minimum Surface Dilution

The horizontal location of minimum surface dilution (X_s/D) was plotted against F, both normalized by H/D, in Figure 4.16 according to [1]. Similar to the dilution plot, no minimum surface dilution point is viable for the FSR. As F increases in the PCR, the X_s/D reaches an almost constant value and it will decrease with further increase of F, when the CIR governs. Numerical results of the LRR and v2f models are in good agreement with the experimental data, as shown in Figure 4.16, with lower estimate of Xs for v2f turbulence model comparing to the experimental data. The average differences between numerical results and experimental data are 2% and 6% for the LRR and v2f turbulence models, respectively, for 45° discharges.

An important observation made by [1], as a result of their experiments, was that the horizontal locations of minimum surface dilution, the maximum horizontal velocity and the maximum vertical velocities are different in the PCR and the CIR regimes. The numerical results of both the LRR and the v2f turbulence models verify this observation as well as confirming the maximum horizontal velocity in the attachment zone occurs at a farther distance from the nozzle compared to the maximum vertical velocity. This suggests that after the impingement point, the vertical velocity decreases while the horizontal velocity increases as the jet flows downstream. This is in line with elements evident in Figure 4.12 and Figure 4.13 where the velocity magnitude stayed constant (in PCR) or even increased locally (in CIR) even though the vertical velocity dropped. This suggests a transition from vertical momentum to horizontal momentum in the surface impingement zone.

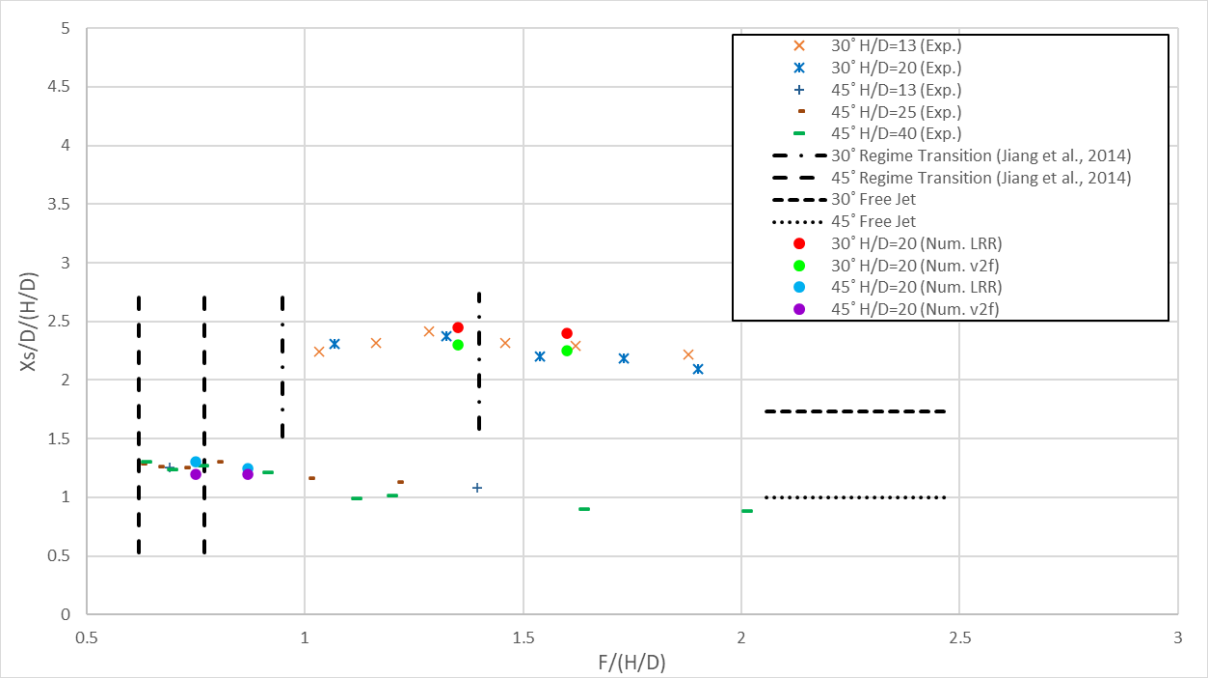

Figure 4.16: Horizontal locations of minimum surface dilution for 30° and 45° discharges.

4.4.6 Return Point Dilution and Location

The numerical results of minimum return dilutions and their corresponding horizontal locations obtained from all turbulence models are presented in Table 4.1 and Table 4.2, for 30° and 45° discharge inclinations, respectively.

Minimum Return Dilution

Similar to that of the minimum surface dilution (S_s), the minimum return dilutions (S_r) are normalized with H/D and plotted in Figure 4.17 and Figure 4.18 for 30° and 45° inclinations, respectively. Consistent with past studies of submerged jets [6, 28], the dilution at the return point is almost linearly proportional to F. As F increases and the jet transitions into PCR and CIR, where surface attachment occurs, the dilution reaches an approximate asymptotic condition. This is the main limitation of effluent discharges into shallow water environments. Root mean square error (RMSE) and mean error (ME) are calculated for each numerical model and are presented in Table 4.4 for the 30° and 45° discharge angles. As shown in Figure 4.17, Figure 4.18 and in Table 4.4, the LRR model performs better at estimating the return point dilution compared to all other turbulence models evaluated in this study.

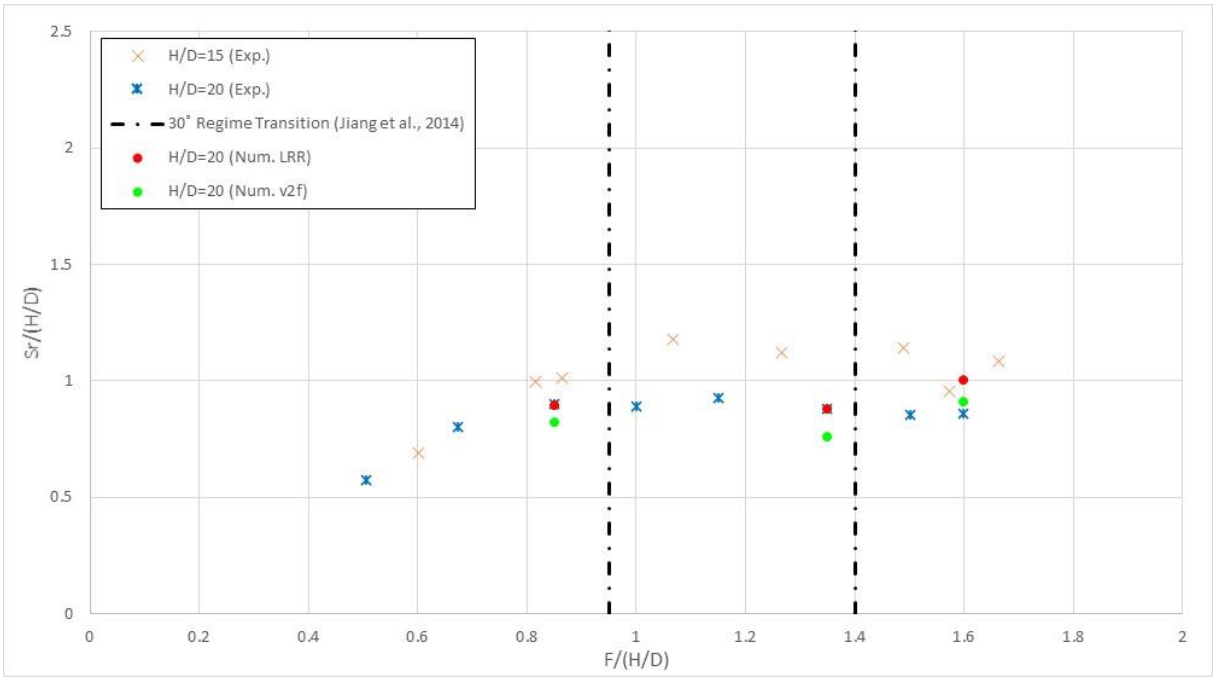

Figure 4.17: Normalized minimum return dilution versus normalized Froude number for 30° discharge.

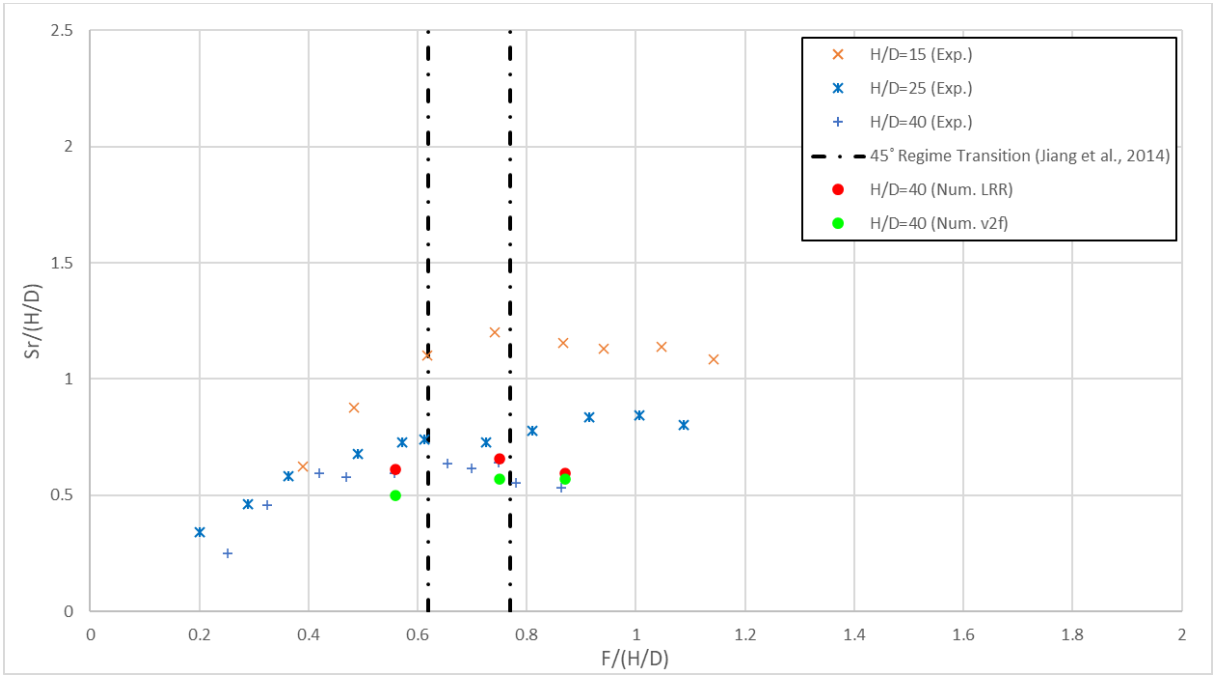

Figure 4.18: Normalized minimum return dilution versus normalized Froude number for 45° discharge.

Table 4.4: Root mean square error (RMSE) and mean error (ME) of return location and dilution for 30° and 45° discharges.

Turbulence Model	Parameter RMSE				Parameter ME (Present Study – Jiang et al., 2014)			
	Sr/(H/D)	Xr/D/(H/D)	Sr/(H/D)	Xr/D/(H/D)	Sr/(H/D)	Xr/D/(H/D)	Sr/(H/D)	Xr/D/(H/D)
	30°		45°		30°		45°	
LRR	**0.08**	**0.94**	**0.01**	**0.12**	0.04	-0.59	0.01	-0.06
SSG	0.10	0.96	0.02	0.16	0.02	-0.45	-0.01	-0.06
v2f	0.09	1.37	0.07	0.24	-0.05	-1.09	-0.06	-0.21
Realizable k-ε	0.11	1.22	**0.01**	0.15	0.06	-0.70	0.00	-0.02
k-ω SST	0.17	2.18	0.31	0.37	-0.13	-1.79	-0.23	-0.36

Horizontal Location of Minimum Return Dilution

Horizontal location of minimum return dilution (X_r/D) is normalized by H/D (according to [1]) and plotted versus F (Figure 4.19 and Figure 4.20, for 30° and 45° discharges, respectively). As expected, the return point length increases with an increase in F. However, the slope of the increase at the return point length versus F is steeper in the PCR and CIR than FSR which is due to the surface attachment. Numerical results shown in Figures 4.19 and 4.20 are in good agreement with experimental data of [1], especially for the FSR and PCR regimes. Numerical results underestimate the horizontal location of minimum return dilution in the CIR regime for both 30° and 45° discharges by about 20%. The X_r/DF coefficients on Figure 18 and Figure 19 were extracted for each turbulence model and for each discharge angle. They are compared to the return point location values from experiments as shown in Table 5. Moreover, to better quantify the comparisons, the absolute differences of the horizontal locations of minimum return dilution are also shown in Table 5. Figure 20 shows the numerical results (this study) versus experimental data [1] of return location and dilution for 30° and 45° discharges. LRR turbulence model performed the best among all turbulence models evaluated in this study for both the minimum return dilution and the corresponding horizontal location, except for the horizontal location of the minimum return dilution for 30° discharge. For the latter, the realizable k-ε turbulence model showed a better performance when results were compared to the average value of all other past experimental studies.

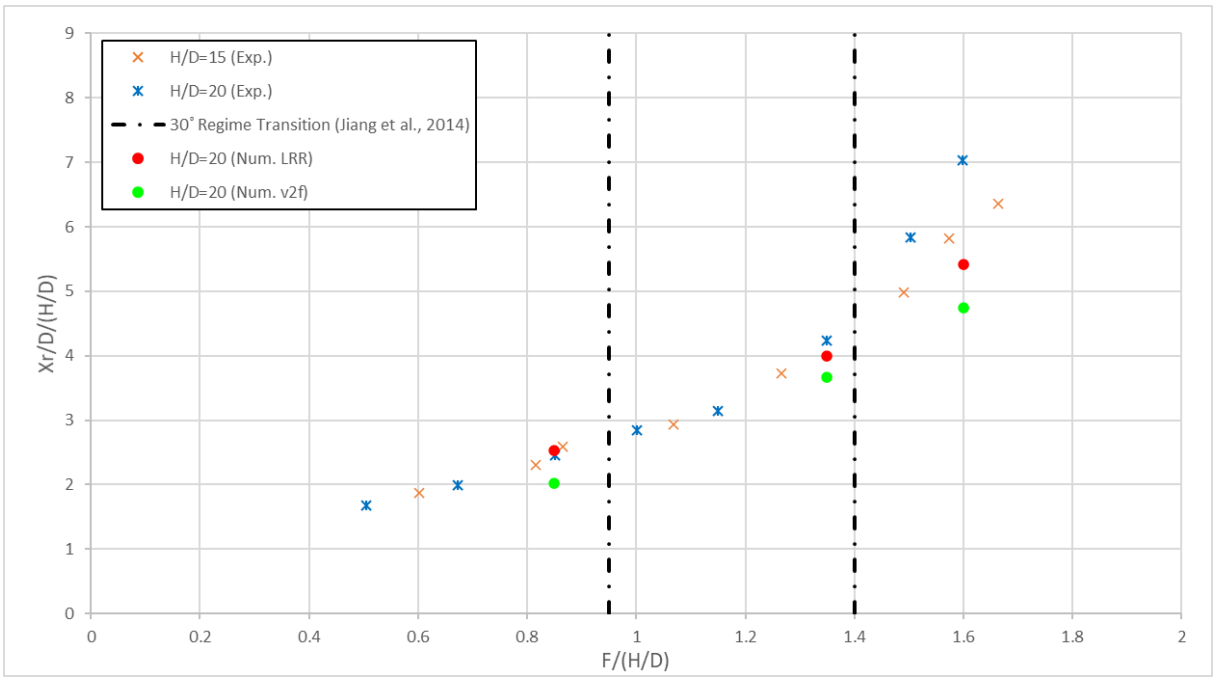

Figure 4.19: Horizontal locations of minimum return dilution for 30° discharge.

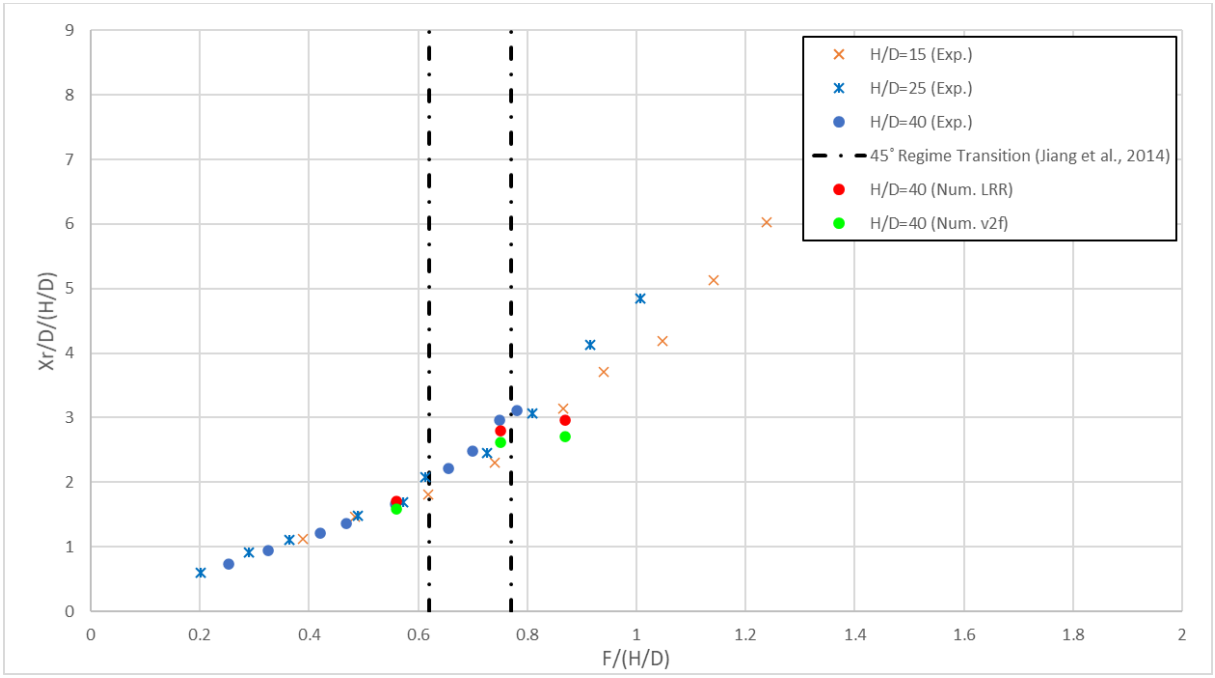

Figure 4.20: Horizontal locations of minimum return dilution for 45° discharge.

Table 4.5: Comparison of return point location coefficients (bold number is the lowest absolute difference).

Study		Coefficient of the Return Point Horizontal Displacement		Coefficient of the Return Point Dilution		Absolute Difference (Present Study – the Average of All Other Experimental Studies)			
		Xr/DF		Sr/F		Xr/DF		Sr/F	
		30˚	**45˚**	**30˚**	**45˚**	**30˚**	**45˚**	**30˚**	**45˚**
Present Study	LRR	2.97	3.06	1.05	1.09	0.14	**0.02**	**0.28**	**0.31**
	SSG	3.35	3.14	1.01	1.02	0.24	0.05	0.32	0.38
	v2f	2.39	2.84	0.96	0.90	0.72	0.25	0.37	0.51
	Realizable k-ε	3.07	3.21	1.01	1.04	**0.03**	0.13	0.32	0.36
	k-ω SST	2.17	2.54	0.78	0.86	0.93	0.55	0.55	0.54
[1]		2.98	3.00	1.16	1.42	-			
[26]		3.18	3.34	0.82	1.09				
[27]		-	3.16	-	1.55				
[24]		3.00	2.83	1.45	1.26				
[25]		3.14	3.26	-	-				
[28]		3.30	3.20	1.90	1.70				
[29]		3.03	2.82	-	-				

4.5 Discussion on the Performance of Turbulence Models

One of the main objectives of the current study was to evaluate the suitability of RANS turbulence models used for the modelling of the mixing of effluents in the shallow waters, especially with surface attachment.

Based on the numerical results and comparisons presented in Table 4.1 and Table 4.2 and in the subsequent comparison tables (Table 4.4 and Table 4.5), it can be concluded that the LRR model performed best among all other RANS model tested herein. There could be multiple reasons for this as hypothesized by the authors below:

- *Secondary flow*: secondary flows are important in the effluent discharge and mixing application [33]. Due to its anisotropic structure, the LRR model is more accurate since it considers the effects of secondary flows that occur due to stress-induced flows. The secondary flow vortexes in the case of inclined dense jet discharges into a stagnant ambient water are due to multiple mechanisms. One is due to the buoyancy-induced gravitational instabilities, where momentum pushes the jet forward and buoyancy sinks

the jet downward. The other mechanism is due to Kelvin-Helmholtz (KH) shear instabilities which happen at the jet-water interface where there is a velocity difference across. Such secondary flows result in higher turbulence and, thus, stronger mixing of the jet. A more detailed numerical study using LES models will reveal the details on the turbulence structure of these vortexes.

- *Pressure*: the pressure strain term combined with the stress production term in the LRR model results in more accurate calculation of shear stresses especially on the jet-water interface where the pressure difference controls the jet trajectory. This is especially important in the surface impingement area in the PCR and CIR regimes, as well as in the bed impact area (not investigated in this study) due to higher pressure differences occurring at the jet boundary in these areas.
- *Buoyancy*: amongst all turbulence models employed in this study, the RSMs include turbulent kinetic energy production due to buoyancy effects. Even though the buoyancy difference between the jet and the ambient receiving water is not large in the cases studied herein (i.e. $\Delta\rho/\rho_a < 3\%$), it is a key factor in the jet spread width as well as in the buoyancy distortions observed in the case of such inclined dense jets, especially for the inner half of the jet. It is expected that RSMs perform significantly better as the buoyancy difference between the jet and ambient water increases. Other turbulence models could be modified to include the buoyancy terms in the governing equations of the production and dissipation of turbulent kinetic energy. [6] evaluated this using the standard k-ε model and found that it helps with the jet growth rate prediction. However, the changes were relatively small, something attributed to a small difference in density between the discharge and the ambient water.

Among the four other turbulence models applied in this study, the v2f turbulence model is a four-equation model and conceptually between the RSMs and two-equation models, with added features for the turbulence anisotropy and pressure-strain effects. However, as shown in Table 4.4 and Table 4.5, the v2f turbulence model was not able to reproduce the geometrical and kinematic properties of the inclined dense jets as well as the LRR turbulence model or even the realizable k-ε model. It was reported [34] that v2f model is more successful when applied to the

case of wall jets and boundary layer applications as it is closer to the k-ω SST model which is more suitable for the high shear regions such as boundary layer problems. On the other hand, the realizability assumption in the realizable k-ε model improves the shortcoming of the isotropic character of eddy viscosity in the k-ε family models (e.g. standard k-ε model) which makes them rather insensitive to the orientation of the turbulence structure and its transporting and mixing mechanisms. The realizable k-ε model was also reported to be a suitable choice of turbulence model for effluent discharge modelling in the previous studies [4-6]. The SSG turbulence model (also an RSM, similar to LRR) performance was not as good as that of the LRR turbulence model but was comparable to the realizable k-ε model's performance (see Table 4.4 and Table 4.5). The computational time required by the SSG turbulence model is longer than that of the realizable k-ε for the mixing cases studied herein: thus, this could be a trade-off for choosing among these two models.

The performance of various RANS turbulence models has been previously evaluated for the mixing of turbulent inclined dense jets in stationary deep ambient waters [6-8]. The difference in results of the two-equation turbulence models (e.g. realizable k-ε) and RSMs (e.g. LRR) in those studies are smaller than that of shallow waters studied in the present paper. This suggests that for mixing in shallow waters with surface attachment, applying turbulence models such as the LRR, that better handle the flow interactions and nonlinearities, is more critical.

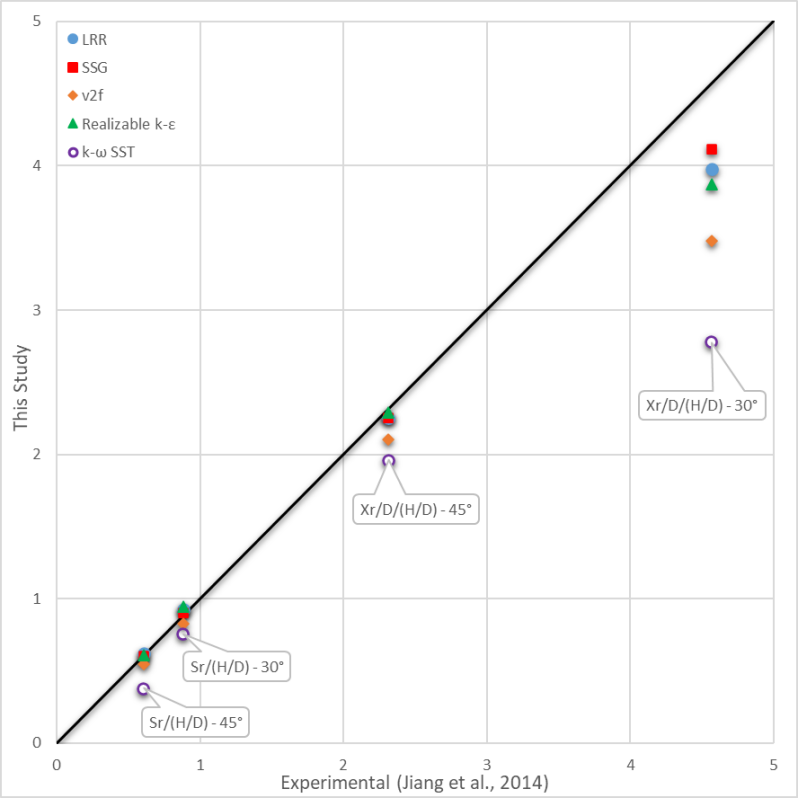

Figure 4.21: Numerical results (this study) versus experimental data (Jiang et al., 2014) of return location and dilution for 30° and 45° discharges.

4.6 Conclusions

A comprehensive numerical modelling study was performed for the first time to investigate the effluent discharge of 30° and 45° inclinations into shallow waters. A range of RANS turbulence models were examined: the realizable k-ε and the k-ω SST models (known as two-equation turbulence models), v2f (four equations to model anisotropic behavior) and the LRR and SSG turbulence models (known as Reynolds stress models - six equations to model anisotropic behavior). The validated model in this study will be applicable to other discharge inclinations as well (e.g., 60° discharge). The following conclusions are drawn based on the results of this study.

- Axial velocities were extracted at different cross sections along the jet trajectory. They were then used to identify the jet centerline, as well as the different stages (i.e. initial, attachment, developed and two transitions between them for the PCR and CIR). For the PCR and CIR, the decay of the maximum axial velocity was affected by the surface attachment which results in farther propagation of the jet along the water surface.

- Minimum dilution at the surface and the return point were extracted in all numerical cases and were compared to those from the experimental work of [1]. It was found that, as the Froude number increased and the mixing regime changed from FSR to PCR and then CIR, the surface dilution (Ss) decreased until it reached an asymptotic limit, which is about *Ss/(H/D)* of 0.38 and 0.27 in the CIR for 30° and 45° discharges, respectively. The average differences between numerical results and experimental data of minimum surface dilution are +4% and -7% for the LRR and v2f turbulence models, respectively, for 45° discharges.
- The normalized *F/(H/D)* values for both 30° and 45° discharge angles in numerical cases (*F/(H/D)* value is the same for all turbulence models in each regime) are given in Table 4.3. The values are within the range proposed by [1] which confirms that the modelled jets fall within the correct classification for each *F/(H/D)*.
- Lower discharge angle (30°) reduces the probability of surface attachment for a given water depth when compared to the higher discharge angle (45°). However, if surface attachment occurs for both the 30° and 45° inclinations, the 45° discharges would be preferable since, for this case, the jet ensures a better return dilution. For instance, the average estimated return dilution *Sr* by LRR turbulence model in the PCR and CIR regimes for the 30° and 45° discharges are 18.75 and 25.05, respectively.
- The LRR RSM turbulence model was the most accurate among the five different turbulence models tested herein. The RSM models (and particularly the LRR model) reasonably captured secondary flows and buoyancy-induced forces since these models account for the effects of the stress anisotropy. Discrepancies between the numerical results and the experimental data exists, e.g. in the simulation of processes such as internal detrainment and therefore the velocity spread and dilution predictions. Moreover, the computational costs of the different turbulence models have to also be considered. RSMs are more computationally expensive than both two- and four-equation models (e.g. about 20 % more than realizable k-ε).
- The experimental data from [8] includes 60° inclined dense jets in shallow waters. Authors are currently performing analyses using the existing model for simulation of 60° inclined

dense jets in shallow waters using the data from [8]. The observations from [8] is close to that from [1] and our numerical results are capable to reproduce those cases. [8] has suggested slightly different transition criteria. Table 6 summarizes the comparison of transition criteria between the current study, [1] and [10].

- For the next steps, parameters such as ambient water stratification, current and wave can be added to the existing model to account for the environmental forcing. Turbulence and vorticity of the jet, especially in the attachment zone, can also be studied in more details using LES turbulence models.

Table 4.6: Comparison of regime transition criteria (values of F.D/H) in shallow water jets.

Regime	Experimental [1]		Experimental [10]			Numerical	
	30°	**45°**	**30°**	**45°**	**60°**	**30°**	**45°**
FSR	< 0.95	< 0.62	< 0.80	< 0.48	< 0.42	0.85	0.56
PCR	$0.95 - 1.4$	$0.62 - 0.77$	$0.80 - 1.15$	$0.48 - 0.70$	$0.42 - 0.64$	1.35	0.75
CIR	≥ 1.4	≥ 0.77	≥ 1.15	≥ 0.70	≥ 0.64	1.60	0.87

Notation

Following symbols were used in this paper:

b = velocity 1/e width
b_c = concentration 1/e width
C = concentration at each cell
C_0 = discharge concentration
D = nozzle diameter
F = densimetric Froude number
g = gravitational acceleration
H = water depth above nozzle level
k = turbulent kinetic energy
Lv = distance along the jet centerline
P *or* p = fluid pressure
Pr_t = turbulent Prandtl number
q_j = turbulent scalar flux
r = radial distance
S_r = minimum dilution at the return point
S_s = minimum dilution at the water surface
u = fluid velocity
U_0 = discharge initial velocity
U_m = maximum streamwise velocity at a cross section
V_m = maximum vertical velocity at a cross section
X_r = horizontal location of minimum dilution at the return point

X_s = horizontal location of minimum dilution at the water surface
Y_t = jet terminal rise height
R_{sp} = jet lateral spread rate
Γ = scalar diffusivity
Γ_t = turbulent dispersity
δ_{ij} = Kronecker delta
ε = dissipation rate
μ = fluid viscosity
μ_t = turbulent eddy viscosity
ρ = fluid density
ρ_0 = discharge density
ρ_a = ambient density
τ_{ij} = Reynolds stresses

References

[1] Jiang, B., Law, A.W.K., Lee, J.H.W. 2014. Mixing of 30˚ and 45˚ Inclined Dense Jets in Shallow Coastal Waters. Journal of Hydraulic Engineering, 140(3), 241–253. https://doi.org/10.1061/(ASCE)HY.1943-7900.0000819.

[2] Gildeh, H.K. 2013. Numerical modeling of thermal/saline discharges in coastal waters. M.A.Sc. Thesis. University of Ottawa, Ottawa, Ontario, Canada.

[3] Zhang, S.; Jiang, B.; Law, A.W.K. 2016. Large Eddy Simulation of 45 Inclined Dense Jets. Env. Fluid. Dyn. 16:101-121.

[4] Gildeh, H.K., Mohammadian, A., Nistor, I., Qiblawey, H. 2014. Numerical Modeling of Turbulent Buoyant Wall Jets in Stationary Ambient Water. Journal of Hydraulic Engineering, 140(6), 04014012. https://doi.org/10.1061/(ASCE)HY.1943-7900.0000871.

[5] Gildeh, H.K., Mohammadian, A., Nistor, I., Qiblawey, H. 2015. Numerical modeling of 30˚ and 45˚ inclined dense turbulent jets in stationary ambient. Environmental Fluid Mechanics, 15(3), 537–562. https://doi.org/10.1007/s10652-014-9372-1.

[6] Gildeh, H.K., Mohammadian, A., Nistor, I., Qiblawey, H., Yan, X. 2016. CFD modeling and analysis of the behavior of 30˚ and 45˚ inclined dense jets – new numerical insights. Journal of Applied Water Engineering and Research, 4(2), 112–127. https://doi.org/10.1080/23249676.2015.1090351.

[7] Zhang, S.; Law, A.W.K.; Jiang, B. 2017. Large eddy simulations of 45˚ and 60˚ inclined dense jets with bottom impact. J. Hydro. Env. Res. 54-66.

[8] Abessi, O., Roberts P.J.W. 2016. Dense Jet Discharges in Shallow Water. Journal of Hydraulic Engineering, 142(1), 04015033. https://doi.org/10.1061/(ASCE)HY.1943-7900.0001057.

[9] Kheradmand, S., Mohammadian, A., Seidou, O., Gildeh, H. K. 2015. Numerical and experimental investigation of saline discharges in stationary ambient. 22nd Canadian Hydrotechnical Conference, Montreal, Quebec, Canada.

[10] Ahmad, N., Suzuki, T. 2016. Study of dilution, height, and lateral spread of vertical dense jets in marine shallow water. Water Science and Technology, 73(12), 2986–2997. https://doi.org/10.2166/wst.2016.121.

[11] Angelidis, P., Kalpakis, D., Gyrikis, V., Kotsovinos, N. 2017. 2D brine sewage after impinging on a shallow sea free surface. Environmental Fluid Mechanics, 17(3), 615–628. https://doi.org/10.1007/s10652-017-9511-6.

[12] Mohammadian, A., Gildeh, H.K., Nistor, I. 2020. CFD Modeling of Effluent Discharges: A Review of Past Numerical Studies. Water. 12, 856.

[13] Yan, C., Nepf, H.M., Huang, W.X., Cui, G.X. 2017. Large eddy simulation of flow and scalar transport in a vegetated channel. Environ Fluid Mech (2017) 17:497–519. DOI 10.1007/s10652-016-9503-y.
[14] Baum, M.J., Gibbes, B. 2019. Field-scale numerical modeling of dense multiport diffuser outfall in crossflow. Journal of Hydraulic Engineering. 146(1): 05019006.
[15] Pope, S. B. 2000. Turbulent flows. Cambridge, UK: Cambridge University Press.
[16] Leschziner, M. 2016. Statistical turbulence modelling for fluid dynamics—demystified: An introductory text for graduate engineering students. London: Imperial College Press.
[17] OpenCFD Limited. (2017). OpenFOAM - User Guide, Version 4.1.0.
[18] Huai, W., Li, Z., Qian, Z. et al. 2010. Numerical simulation of horizontal buoyant wall jet. J Hydrody. 22(1):58-65.
[19] Ramakanth, A. Quantifying Boundary Interaction of Negatively Buoyant Jets. Ph.D. Thesis, Department of Civil and Natural Resources Engineering, University of Canterbury, Christchurch, New Zealand, 2016.
[20] Shan, J. W. & Dimotakis, P. E. 2006 Reynolds-number effects and anisotropy in transverse-jet mixing. J. Fluid. Mech. 566, 47–96.
[21] Mydlarski, L. & Warhaft, Z. 1998 Three-point statistics and the anisotropy of a turbulent passive scalar. Phys. Fluids 10, 2885–2894.
[22] Shih, T.H., Liou, W.W., Shabbir, A., Yang, Z., Zhu, J. 1994. A new k-ε eddy viscosity model for high Reynolds number turbulent flows- Model development and validation. Computers Fluids. 24(3).227–238. 1995.
[23] Menter., F. R. 1994. Two-Equation Eddy-Viscosity Turbulence Models for Engineering Applications. AIAA Journal. 32(8). 1598–1605.
[24] Durbin, P. A. 1995. Separated Flow Computations with the k-ε-v^2 Model. AIAA Journal. 33(4). 659–664.
[25] Launder, B.E., Reece, G.J., W. Rodi. Progress in the Development of a Reynolds-Stress Turbulence Closure. *Journal of Fluid Mechanics*, 68:537–566, 1975.
[26] Speziale, C.G., Sarker, S., Gatski, T.B. 1991. Modelling the pressure-strain correlation of turbulence. An invariant dynamical systems approach. Journal of Fluid Mechanics. 227:245–272, 1991.
[27] Shao, D., Law, A.W.K. 2010. Mixing and boundary interactions of 30° and 45° inclined dense jets. Env Fluid Mech 10:521-553.
[28] Kikkert, G.A., Davidson, M.J., Nokes, R.I. 2007. Inclined negatively buoyant discharge. J Hydraul Eng, ASCE 133(5):545-554.
[29] Lai, C., Lee, J. H. W. 2012. Mixing of inclined dense jets in stationary ambient. J. Hydro-Environ. Res., 6(1), 9–28.
[30] Papakonstantis, I. G., Christodoulou, G. C., Papanicolaou, P. N. 2011. Inclined negatively buoyant jets 2: Concentration measurements. J. Hydraul. Res., 49(1), 13–22.
[31] Nemlioglu, S., Roberts, P. J. W. 2006. Experiments on dense jets using three-dimensional laser-induced fluorescence (3DLIF). MWWD 2006–4th Int. Conf. on Marine Waste Water Disposal and Marine Environment, International Association for Hydro-Environment Engineering and Research (IAHR), International Water Association (IWA), Madrid, Spain, London, U.K.
[32] Cipollina, A., Brucato, A., Grisafi, F., Nicosia, S. 2005. Bench-scale investigation of inclined dense jets. J. Hydraul. Eng., 10.1061/(ASCE) 0733-9429(2005)131:11(1017), 1017–1022.
[33] Hanjalic, K. 1999. Second-moment turbulence closures for CFD: Needs and prospects. Int. J. Comput. Fluid Dynam., 12(1), 67–97.
[34] Sanz, W., Pecnik, R., Tratnig, A., Heitmeir, F. 2007. Application of Modern Turbulence Models to Steady and Unsteady Transitional Flow. European Conference on Turbomachinery, Athens, Greece, 4 Mar 2007-10 Mar 2007.

5 Vertical Dense Effluent Discharge Modelling in Shallow Waters[4]

Abstract: Vertical dense effluent discharges are popular in the design of outfall systems. Vertical jets provide the opportunity to be efficient for a range of ambient currents, where the jet will be pushed away not to fall on itself. This study focuses on the worst-case scenario in terms of mixing and dilution of such jets: vertical dense effluent discharges with no ambient current and in shallow water where jet impacts the surface. This scenario provides a conservative design criteria for such outfall systems. The numerical modelling of such jets has not been investigated before and this study provides novel insights in simulations of vertical dense effluent discharges in shallow waters. Turbulent vertical discharges with Froude numbers ranging from 9 to 24 were simulated using OpenFOAM. A Reynolds stress model (RSM) was applied to characterize the geometrical (i.e., maximum discharge rise Z_m and lateral spread R_{sp}) and dilution μ_{min} properties of such jets. Three flow regimes were reproduced numerically, based on the experimental data: deep, intermediate and impinging flow regimes.

Keywords: Vertical dense jet, Shallow water, Impingement, Surface dilution, Return point, Effluent discharge, OpenFOAM

---

4 This chapter of the study has been submitted as: Kheirkhah Gildeh, H., Mohammadian, A., Nistor, I. (2021). "Vertical Dense Effluent Discharge Modelling in Shallow Waters", Water and Environment Journal (Wiley).

5.1 Introduction

Dense effluents are residual flows resulted from physical and/or chemical processes. Brines from desalination plants, wastewaters from wastewater treatment plants and tailings effluents from mining plants are a few examples where the effluent has a higher density than that of the receiving water body. Receiving water body (often called ambient water) can be coastal or inland waters (i.e., lakes and rivers). Dense effluents are discharged back into the ambient waters through outfall systems. The main consideration in designing an efficient outfall is to achieve certain dilution in the initial mixing zone (IMZ) as regulated by environmental authorities. The dilution requirement within the IMZ is to preserve the natural habitats and ecosystems in the receiving water bodies.

Dense effluents are discharged at the water surface or close to the bed. It was shown that submerged outfalls have higher efficiencies due to better mixing and dilution achievement (Bleninger et al., 2009). Different discharge configurations are used in practice as schematically shown in Figure 5.1. Depending on the application, ambient condition, and bathymetry of the discharge location, any of these scenarios might be adopted for construction, assuming that they meet the regulatory criteria for excessive concentration and/or temperature. A deep ambient water condition case was considered in Figure 5.1 which represents an ideal case due to stronger currents and greater depth available for diluting the effluent (Purnama et al., 2003). This is the reason why the majority of previous experimental and numerical studies have focused on effluent discharges in deep waters. Although a higher dilution is achieved in deeper waters, construction and maintenance of such outfalls are relatively expensive due to the need of longer pipelines as, for many coasts, deeper coastal waters are farther offshore. It is therefore necessary to find an optimum location to meet both environmental and economic criteria for shallower water conditions.

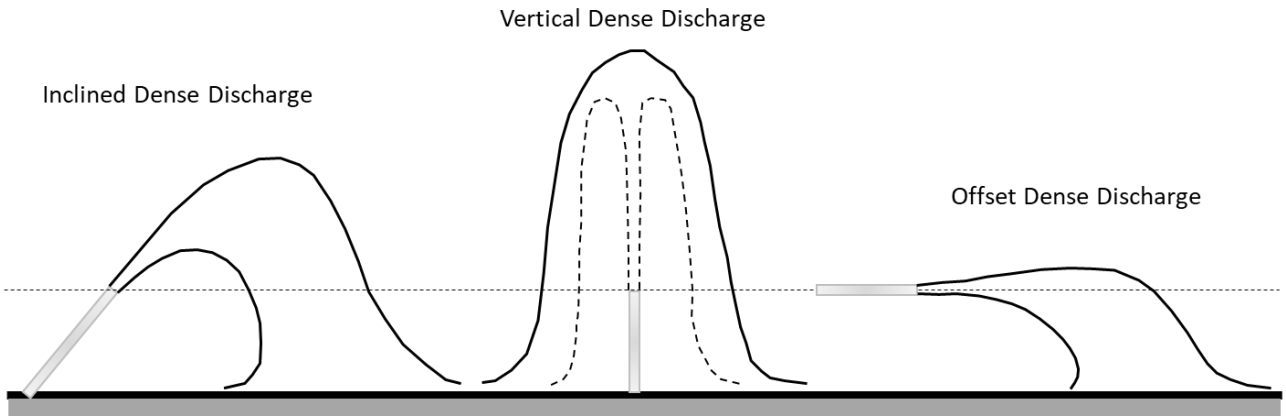

Figure 5.1: Dense effluent discharge configurations in deep waters.

Vertical dense discharges are common in practice as connections of nozzles to the diffuser pipe is easier to construct and maintain. Vertical jets may not be suitable for small ponds where the wind or wave driven currents are constrained, but they are ideal for rivers, large lakes and coastal ambient where ambient water currents exist. Ahmad and Baddour (2014) evaluated vertical dense jets experimentally and argued that the vertical discharges are preferred over the inclined discharges specially in the case of opposite direction of the inclined discharge relative to the direction of the ambient current.

The vertical discharges in deep waters have been investigated extensively in the past, both experimentally and numerically. Table 5.1 summarizes previous studies with a concise description of their respective findings.

Table 5.1: Previous studies of vertical dense discharges in deep waters

Study	Findings
Yannopoulos and Noutsopoulos (1990)	Studied the plane vertical turbulent buoyant jets analytically to find out the discharge flow spreading coefficients (*Kc* and *Kw* for velocity and concentration, respectively). They included a large range of discharge Froude numbers and showed that γ (spreading parameter) is constant (γ=0.6).
Zhang and Baddour (1998)	Investigated the maximum penetration of vertical round dense jets at small and large Froude numbers. They found out that Z_m/L_m reaches an asymptotic value for high Froude numbers (i.e., *Fr*>7) and argued that the mass flux at discharge point has a negligible effect on the maximum discharge penetration .

Baddour and Zhang (2009)	Performed an experimental study to find out the effect of density on round turbulent fountains. Their results indicated that the maximum penetration height of the fountain (Z_m/L_m) was a function of relative density difference (Δ_ρ/ρ_a). They concluded that the Z_m/L_m decreases from 3.06 at Δ_ρ/ρ_a=0.001 to 2.59 at Δ_ρ/ρ_a=0.1.
Elhaggag et al. (2011)	Studied the vertical dense discharges numerically using a computational fluid dynamics (CFD) model. They have used FLUENT to model the vertical jets, however, this study have not discussed the model verification against the experimental data.
Ahmad and Baddour (2012)	Performed an experimental study of dilution and penetration of vertical negatively buoyant thermo-saline jets. They quantified vertical and horizontal penetration of the jet using thermometers and compared to previous studies. They concluded that the vertical jet penetration matches those from previous studies but the horizontal spread is smaller with a value of $\delta_m=1.4r_0Fr$, where r_0 is nozzle radius and Fr is the discharge densimetric Froude number.
Yan and Mohammadian (2017)	Studied the vertical buoyant jets subjected to lateral confinement numerically using the OpenFOAM CFD model. They stated that buoyancy-modified k-ε turbulence model was able to produce reasonable results for such jets. They also varied Prandtl number Pr and turbulent Prandtl number Pr_t for various Froude numbers and claimed this affects the jet predictions.

Studies summarized in Table 5.1 are for vertical discharges in deep waters, without considering the jet impingement into the water surface. There are only limited experimental studies of vertical dense discharges in shallow waters impinging into the water surface, as schematically illustrated in Figure 5.2. Lemckert (2004) performed an experimental study to investigate the spreading radius of the vertical dense discharge in a homogenous calm ambient water with surface attachment. The study tried to quantify the spread radius of the discharge at the water surface before it plunges downstream due to negative buoyancy. It was found that the spreading radius is a function of nozzle size, discharge Froude number and the ambient water depth (i.e., from the nozzle exit to the water surface). Based on a series of experiments and dimensional analysis Lemckert (2004) suggested the following empirical equation (Eqn. 5.1) for

estimating the spreading radius (H: water depth, R_{sp}: spreading radius, r_0: nozzle radius, Fr: densimetric Froude number).

$$\frac{H+R_{sp}}{r_0} = 4.8Fr^{0.74} \quad (5.1)$$

The coefficient of 4.8 and the exponent of 0.75 of the discharge Froude number on the right-hand side of Eqn. 1 were derived experimentally. Lemckert (2004) discussed the upper limit of the proposed formula for the cases where the discharge momentum is large enough to break through the free surface and exit the ambient water.

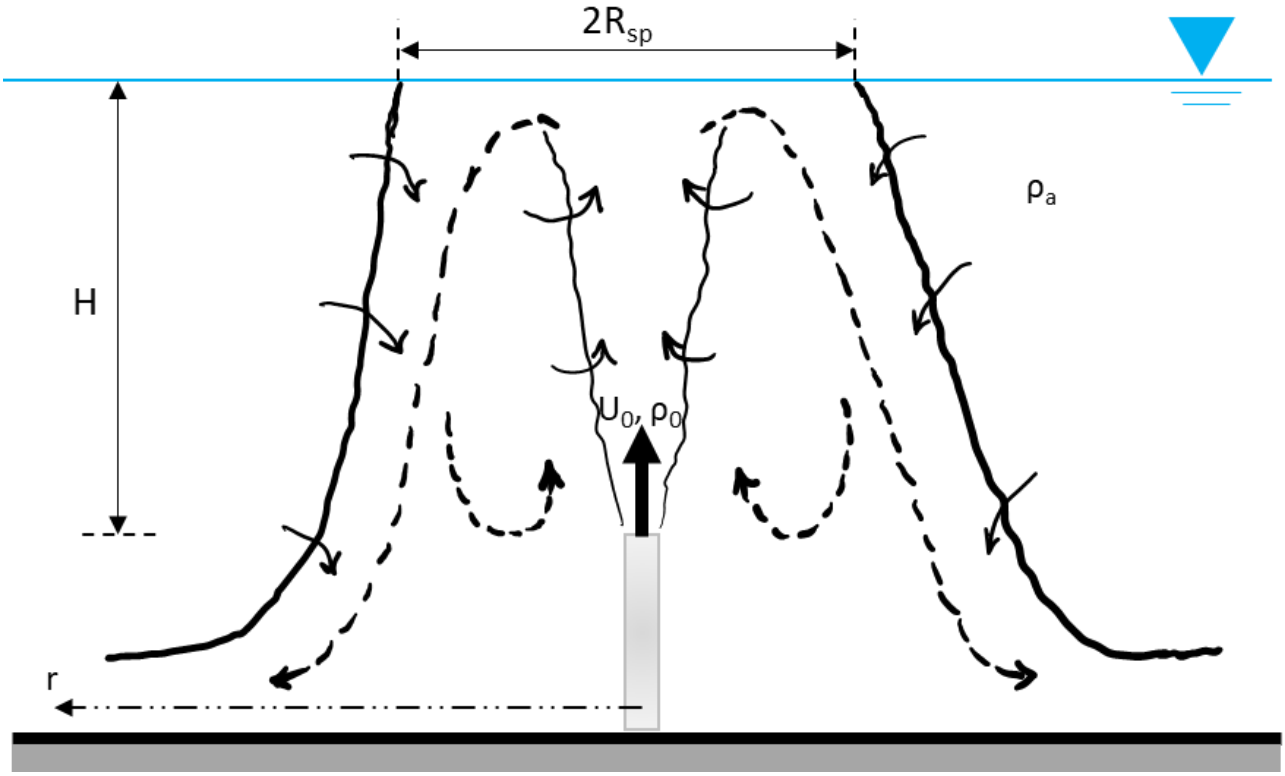

Figure 5.2: Schematic representation of dense effluent discharge with surface attachment

More recently, Ahmad and Suzuki (2016) conducted an experimental study to investigate the dilution, height and spread of vertical dense discharges in shallow waters. They included experimental data of deep waters for comparison purposes. A range of Froude number from 9 to 24 was examined in their study. They used a shadowgraph technique to identify the maximum discharge rise and its lateral spread. Three regimes were identified in their study: deep mixing regime (deep, hereafter), intermediate mixing regime (intermediate, hereafter) and impinging

mixing regime (impinging, hereafter). Return point dilution was measured and reported to be smallest in the impinging regime. Spreading radius of discharge was measured and compared to the empirical relationship from Lemckert (2004). They categorized the deep, intermediate and impinging regimes as summarized in Table 2 (H, r_0, Z_m are water depth, nozzle radius, and maximum rise height, respectively).

Table 5.2: Flow regime in shallow vertical dense jet discharges (Ahmad and Suzuki, 2016)

Deep	Intermediate	Impinging
$H/r_0>1.5\ Z_m/r_0$	$Z_m/r_0<H/r_0<1.5\ Z_m/r_0$	$H<Z_m$

The study from Ahmad and Suzuki (2016) was adopted in the current study to verify the CFD model with. The main objective of this study is to numerically investigate effluent discharges of vertical dense discharges in shallow waters, where the jet attaches to the surface, using OpenFOAM CFD model. To the best knowledge of author, this aspect was never investigated in past studies. This study attempts to fill this gap. A RANS turbulence model is used to predict the geometric and kinematic properties of jets by comparing the current study results against experimental data from Ahmad and Suzuki (2016).

The structure of this paper is as follows: Sections 5.2 discusses the dimensional analysis used for presenting the Z_m and μ_{min}. Section 5.3 describes the numerical details of the CFD model employed for this study. Section 5.4 presents the numerical model results and discussion around them. Finally, Conclusions and Recommendations from the current study are summarized in Section 5.5.

5.2 Dimensional Analysis

The schematic view of a vertical dense discharge in shallow waters was presented in Figure 5.2. The jet is discharged vertically through a nozzle with radius of r_0, jet velocity U_0, jet density ρ_0, and ambient water density ρ_a ($\rho_0 > \rho_a$). The discharge mixes with ambient water as it is discharged and reaches a maximum rise height (also called *terminal rise height*, Zm), and then falls because of negative buoyancy and spreads as a density current which further disperses horizontally. The concentration dispersion depends on both discharge and ambient water characteristics, such as jet discharge concentration, C_0, the initial density difference, $\Delta\rho_0 = \rho_0 - \rho_a$,

the jet velocity, U_0, the discharge nozzle, r_0, and the ambient water depth, H. One of the key parameters in vertical dense discharge analysis is the jet densimetric Froude number, which is the ratio of inertia to buoyancy forces and is calculated as follows:

$$Fr = \frac{U_0}{\sqrt{g_0' r_0}} \tag{5.2}$$

$$g_0' = \left(\frac{\Delta\rho_0}{\rho_a}\right) g \tag{5.3}$$

where g is the gravitational acceleration and g_0' is the reduced gravitational acceleration. The jet mixing characteristics of interest are Z_m and μ_{min}.

The vertical dense discharges are characterized by the jet discharge volume flux (Q_0), kinematic momentum flux (M_0), and the buoyancy flux (B_0) (Ahmad and Suzuki, 2016), which are provided by the following equations:

$$Q_0 = U_0 \pi \frac{D^2}{4} \tag{5.4}$$

$$M_0 = U_0^2 \pi \frac{D^2}{4} \tag{5.5}$$

$$B_0 = Q_0 g_0' \tag{5.6}$$

In dimensional analysis, it was shown (Ahmad and Suzuki, 2016) that a characteristic length (e.g., maximum discharge rise) for the jet may be written as:

$$Z_m = constant\ (L_M) \tag{5.7}$$

where L_M is the momentum length scale, and is calculated as:

$$L_M = \frac{M_0^{3/4}}{B_0^{1/2}} \tag{5.8}$$

By substituting for M_0 and B_0, the following length scale is suitable to nondimensionalize vertical penetration data (Zhang and Baddour, 1998).

$$L_s = r_0 Fr \tag{5.9}$$

For dilution, a simple definition is given by Ahmad and Suzuki (2016) as formulated below.

$$\mu_{min} = \frac{\Delta C_0}{\Delta C_1} \tag{5.10}$$

where $\Delta C_0 = C_0 - C_a$ and $\Delta C_1 = C_1 - C_a$. C_0, C_a and C_1 represent the discharge concentration at the nozzle, the ambient water concentration and the discharge concentration at return point, respectively.

Using a similar approach to that adopted to derive Eqn. (5.9), by substituting for M_0 and B_0, the following effective gravity scale to nondimensionalize jet buoyancy is derived:

$$g_s' = \frac{g_0'}{Fr} \tag{5.11}$$

The effective gravity scale is proportional to the concentration scale when the water equation of state is linear (Ahmad and Suzuki, 2016). Thus:

$$C_s = \frac{\Delta C_0}{g_0'} g_s' \tag{5.12}$$

Combining Eqns. (5.11) and (5.12) will result in:

$$C_s = \frac{\Delta C_0}{Fr} \tag{5.13}$$

Using Eqn. (5.10), the dilution scale for dense jet can be expressed as:

$$\mu_s = \frac{g_0'}{g_s'} = \frac{\Delta C_0}{C_s} \tag{5.14}$$

Substituting Eqn. (5.13) into Eqn. (5.14) results in the following non-dimensional dilution scale (Ahmad and Suzuki, 2016)

$$\mu_s = Fr \tag{5.15}$$

Finally, for the lateral spreading of the discharge, Cooper and Huant (2007) found that water depth over the nozzle, H, is a suitable scale for nondimensionalizing R_{sp}.

5.3 Numerical Details

A RANS turbulence model (Launder-Reece-Rodi, LRR) was adopted for this study. While LES models may improve the simulation of dense jet phenomena in quiescent ambientes, their benefits are incremental and they suffer due to large computational expenses (Baum and Gibbes, 2019).

5.3.1 Governing Equations

The governing equations for the vertical dense effluent discharges for incompressible fluids are based on the full Navier-Stokes equations. Using the same analogy described in Pope (2000) and Leschziner (2016) for the time-averaged Navier-Stokes equations for continuity, momentum and scalar transport, the deriving equations could be written as (Baum and Gibbes, 2019):

$$\frac{\partial \bar{\rho}}{\partial t} + \frac{\partial}{\partial x_i}(\bar{\rho}\overline{u_\iota}) = 0 \tag{5.16}$$

$$\frac{\partial (\bar{\rho}\overline{u_\iota})}{\partial t} + \frac{\partial}{\partial x_j}\left(\bar{\rho}\overline{u_\iota}\overline{u_j}\right) = \frac{\partial \bar{P}}{\partial x_i} + \bar{\rho} g_i + \frac{\partial}{\partial x_j}\left(\mu \frac{\partial \overline{u_\iota}}{\partial x_j}\right) - \frac{\partial \tau_{ij}}{\partial x_j} \tag{5.17}$$

$$\frac{\partial(\overline{\rho u_i})}{\partial t} + \frac{\partial}{\partial x_j}\left(\bar{\rho}\bar{c}\overline{u_j}\right) = \frac{\partial}{\partial x_j}\left(\Gamma \frac{\partial \bar{c}}{\partial x_j}\right) - \frac{\partial q_j}{\partial x_j} \quad (5.18)$$

where subscripts i, j and k denote the axis of system of coordinates; ρ is the fluid density; u is the fluid velocity; p is the pressure; g is the gravitational acceleration; μ is the fluid viscosity; Γ is the scalar diffusivity; c is the scalar concentration and the overbar denotes time-averaged variables. The Reynolds stresses, τ_{ij} and turbulent scalar flux q_j, which can be written as:

$$\tau_{ij} = \mu_t \left(\frac{\partial \overline{u_i}}{\partial x_j} + \frac{\partial \overline{u_j}}{\partial x_i}\right) - 2/3(\rho k + \mu_t \frac{\partial \overline{u_k}}{\partial x_k})\delta_{ij} \quad (5.19)$$

$$q_j = \Gamma_t \frac{\partial \bar{c}}{\partial x_j} \quad (5.20)$$

where μ_t is the turbulent eddy viscosity; k is the turbulent kinetic energy; δ_{ij} is the Kronecker delta and Γ_t is the turbulent dispersion. The Reynolds Stress Models (RSM) described below (Section 3.4.1) directly calculate the Reynolds stresses.

5.3.2 Numerical Solver and Schemes

A Finite Volume Method (FVM) was used to discretize the above-mentioned RANS equations. Simulations were conducted using an open-source CFD model, OpenFOAM version 4.1.0 (2017), using the twoLiquidMixingFoam solver.

The transient simulations in this study were run long enough to reach a steady state condition for the jet flows. A physical time step of 0.001 s and a time duration of 80 s were selected for the simulations.

5.3.3 Boundary Conditions

The model geometry is presented in Figure 5.3. The modelled tank dimensions were selected to be 1.15 m long, 1.15 m wide and a variable depth depending on the model scenario, based on physical model from Ahmad and Suzuki (2016). These dimensions ensure no recirculation caused by boundary walls. The effluent is discharged with a velocity of U_0 and density of ρ_0 through a nozzle with a diameter of D=9.45 mm. Density of the discharge (ρ_0) and ambient water density (ρ_a) ranged between 1,012.4 to 1,013.6 kg/m^3 and 993 to 994.7 kg/m^3, respectively. The density ratio Δ_ρ/ρ_a ranged from 0.015 to 0.019. The inlet values for k and ε were chosen based on Huai et al. (2010) as $k=0.06U_0^2$ and $\varepsilon=0.06U_0^3/D$. The ambient water body was still, with a homogeneous density. The nozzle was mounted 0.14 m above the bed to eliminate any boundary effects. The

outlet boundary was considered all around the tank (i.e., four side faces) with a zero gradient boundary condition positioned perpendicular to those planes. A symmetry boundary was modeled using zero-gradient conditions to represent the atmosphere. The symmetry plane condition specifies that flux and component of the gradient normal to the plane should be zero but free to slide in tangential directions. A Dirichlet condition was used on the bottom wall boundary to implement the zero-velocity condition. OpenFOAM standard wall functions (e.g. epsilonWallFunction, etc.) were implemented for the wall surface to model hydraulically smooth walls.

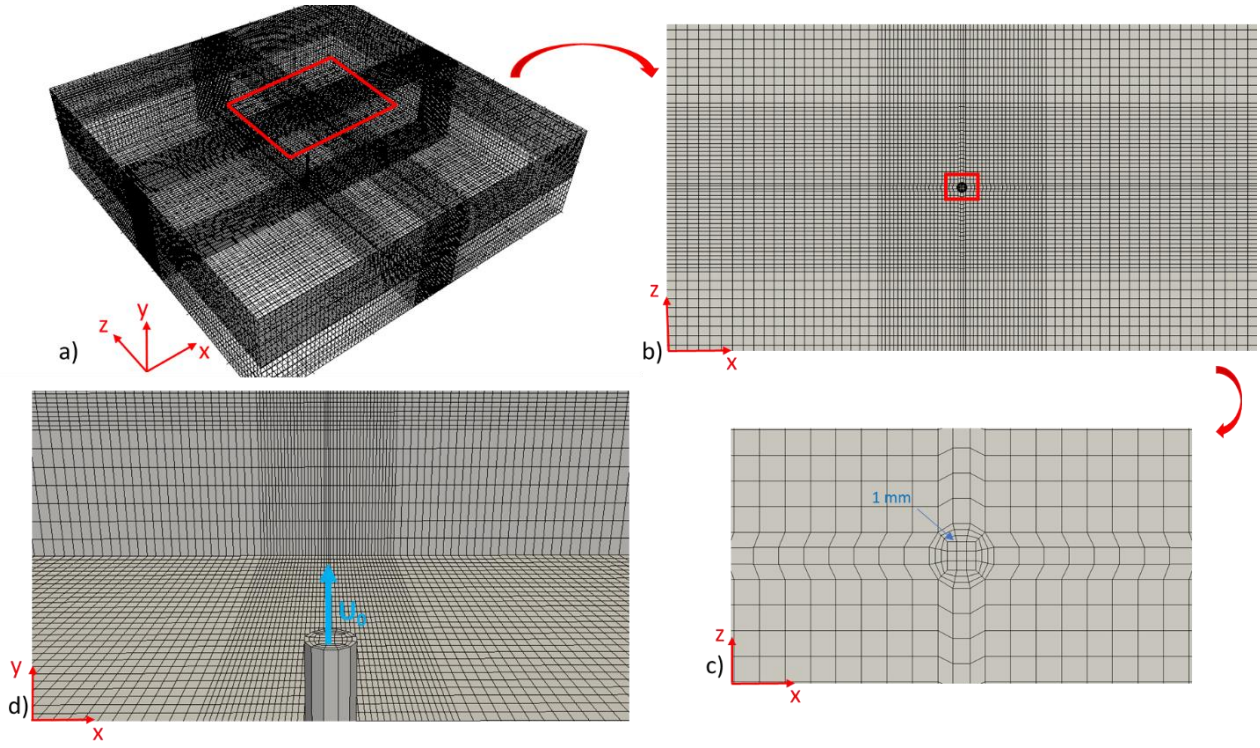

Figure 5.3: Model geometry and computational mesh

The model domain was spatially discretized using a hexahedral mesh with a minimum cell size of 0.001 m around the nozzle and maximum cell size of 0.020 m at the farthest end of tank. The mesh was refined with a higher resolution along the potential jet trajectory to better resolve the flow properties. As part of the mesh sensitivity analysis, several test runs were performed to ensure that the mesh was sufficiently refined to resolve the velocity and concentration gradients especially close to the nozzle. The grid refinement criterion was set to reach a difference of less than 2% between the predicted results when using the last two grids. When this criterion was

reached, it was assumed that a satisfactory mesh was established and no further refinement was needed. The final mesh configuration used in this study includes ~1.5 million cells.

For all the simulations performed in this study, a physical time step of 1×10^{-3} s was used, which leads to a Courant-Friedrichs-Lewy (CFL) number less than 0.5 for stability considerations. Smaller time steps were also tried but the results remained unchanged. The convergence criteria for each time step were set such that the residuals for the velocity components and pressure are 1×10^{-5} and 1×10^{-6}, respectively.

5.3.4 Turbulence Model

The LRR turbulence model was used in this study based on its proven performance (e.g., Gildeh at al., 2014, 2015, 2016, 2021; Mohammadian et al., 2020). This model was developed by Launder et al. (1975). For deriving equations of LRR model and its performance discussion for dense effluent discharges in shallow water reader can refer to Gildeh et al. (2021).

5.3.5 Numerical Cases

Numerical experiments were selected based on the experimental data in Ahmad and Suzuki (2016) as summarized in Table 5.3. As claimed in their study, the experiments were designed to achieve a set of specific objectives. Those objectives included the effect of varying water depths on dense jet heights, relationship between the minimum return dilution and discharge Froude number under varying water depths and impact of Froude number on the maximum discharge rise and discharge lateral spread. Basic goal was to cover deep, intermediate and impinging flow regimes in proposed experiments.

Table 5.3: Numerical experiment parameters

Experiment Series	**Experiment #**	**D ($2r_0$) (mm)**	**U_0 (m/s)**	**$\Delta\varrho/\varrho_a$**	**ϱ_0 (kg/m³)**	**Fr**	**H/r_0**	**$Fr/(H/r_0)$**
A (initial run)	1	9.45	0.54	0.018	1011.89	18.69	34.0	0.55
B (Fixed *H* and variable *Fr*)	2	9.45	0.28	0.019	1012.89	9.44	37.2	0.25
	3	9.45	0.54	0.019	1012.89	18.20	37.2	0.49
C	4	9.45	0.25	0.015	1008.91	9.48	25.4	0.37

(Fixed *Fr* and variable *H*)	5	9.45	0.25	0.015	1008.91	9.48	37.2	0.25
	6	9.45	0.25	0.015	1008.91	9.48	166.0	0.06
D (Variable *Fr* and variable *H*)	7	9.45	0.56	0.019	1012.89	18.87	37.2	0.51
	8	9.45	0.45	0.019	1012.89	15.16	44.4	0.34
	9	9.45	0.54	0.019	1012.89	18.20	52.8	0.34
E (Fixed *H* and variable *Fr*, intermediate *Fr* range)	10	9.45	0.32	0.019	1012.89	10.80	37.2	0.29
	11	9.45	0.36	0.019	1012.89	12.13	37.2	0.33
	12	9.45	0.42	0.019	1012.89	14.15	37.2	0.38
F (Fixed *H* and variable *Fr*, high *Fr* range)	13	9.45	0.43	0.019	1012.89	14.50	37.2	0.39
	14	9.45	0.60	0.019	1012.89	20.22	37.2	0.54
	15	9.45	0.72	0.019	1012.89	24.26	37.2	0.65

5.4 Results and Discussion

The LRR turbulence model used in the current study was successfully employed to simulate inclined dense effluent discharge modelling in shallow waters previously (Gildeh et al., 2021). This section summarizes the results of the current numerical simulations and their comparison to the experimental cases where applicable, both qualitatively and quantitatively. Overall discharge behavior of vertical jets in shallow waters is evaluated first. Discharge dilution rates at return point are characterized for the cases studied herein, followed by geometrical properties for such discharges. Finally, spreading radius of vertical dense discharges studied in this paper are evaluated.

5.4.1 Discharge Evolution

The general discharge behavior is the first investigation performed in this study. The objective was to observe the overall vertical discharge behavior in shallow waters. Figure 5.4 shows a vertical dense effluent discharge into shallow water with surface attachment, while the jet is developing laterally at the surface. The initial momentum of the jet at the discharge point

pushes the jet upward until the jet impinges the water surface. Vertical momentum forces then convert to lateral momentum forces and the jet develops in a symmetrical pattern (Figures 5.4b and 5.4c). At certain distance from the jet center, the horizontal momentum dissipates and buoyancy forces will dominate the flow and jet therefore sinks toward the bottom of the tank. The lateral expansion of vertical dense jets with surface attachment is larger than that of the jets without surface attachment, since the strong vertical momentum leads to the generation of horizontal forces due to jet attachment.

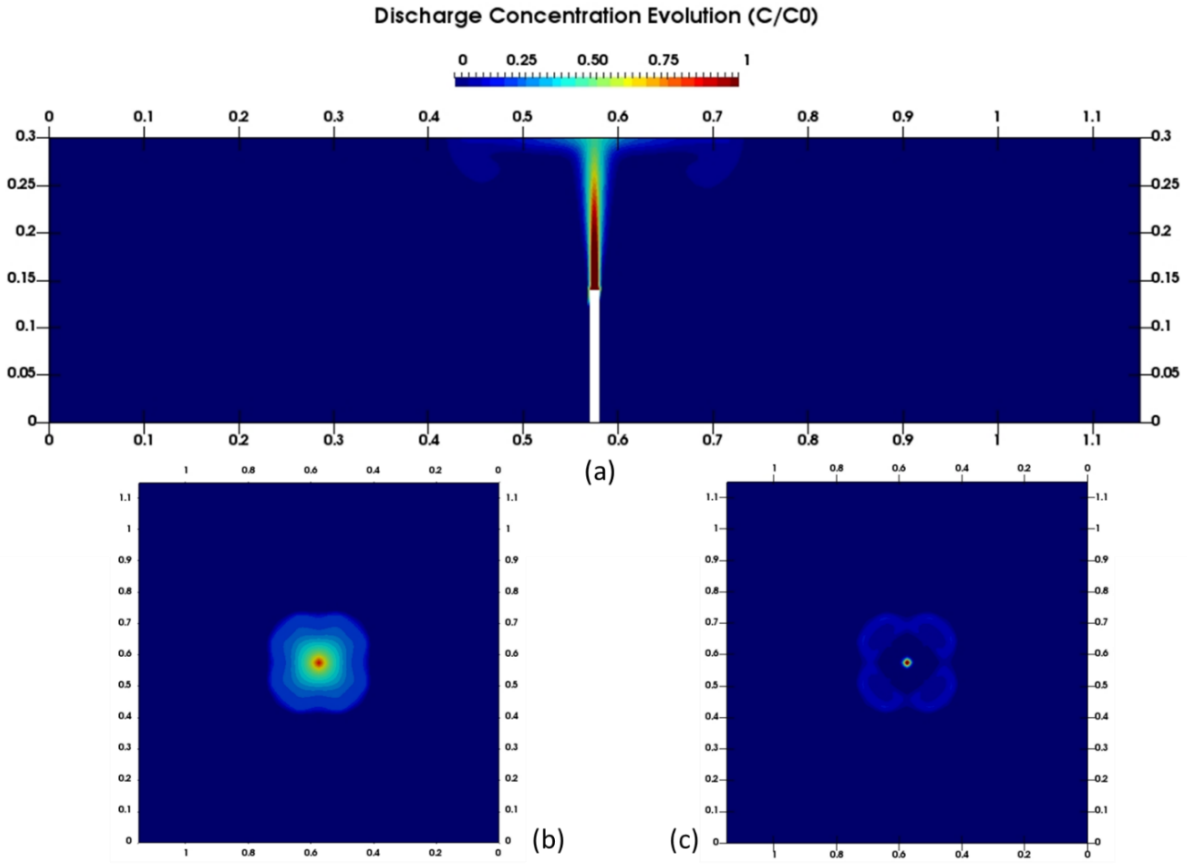

Figure 5.4: Vertical jet evolution in shallow water with surface interaction (C_0 is the discharge concentration and C is discharge computed at each cell). A) lateral cross section along the central plane, b) top view at the water surface at t=60 s, c) top view at the water surface at t=20 s

When an intermediate or impinging flow regime is compared to a deep flow regime (i.e., in the case of a same Froude number but variable *H*), the impact of the water shallowness on the jet height is obvious. The jet height is larger in the intermediate and impinging flow regimes which

is due to the stress conditions between two boundaries and viscous forces between two fluids with different densities. The other physical reason behind the difference of the discharge height is the smaller pressure field in the intermediate and impinging regimes when compared to that observed in the deep regime. In deep regime, the larger water column will increase the pressure on the jest which dissipates the vertical momentum forces faster.

Experimental modelling of vertical jets in shallow waters showed the water surface disturbance in case of intermediate and impinging regimes (Ahmad and Suzuki, 2016). Figure 5.5 (from experimental study of Ahmad and Suzuki, 2016) is comparable to the top views shown in Figure 5.4 (b) and (c).

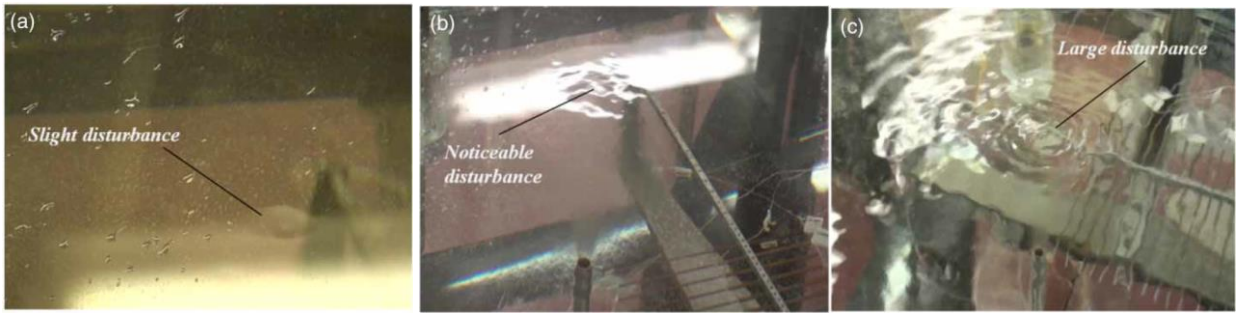

Figure 5.5: Top view of water surface disturbance observed in the experimental study for H/r_0=37.2 and a) Fr=10.9, b) Fr=18.2 and c) Fr=24.2 (Ahmad and Suzuki, 2016; With permission from Water Science & Technology).

5.4.2 Discharge Dilution

Figure 5.6 illustrates the mean nondimensionalized concentration (C/C_0) profiles against the nondimensionalized radial distance from the nozzle $(r-r_0)/r_0Fr$ at the horizontal plane at the nozzle level (z=0). The numerical cases from B series of experiments have been compared to those from Ahmad and Suzuki (2016). A concentration profile from a deep regime of the experimental study is shown in Figure 5.6 for reference. In the two numerical cases (from B series), the water depth to the nozzle radius ratio, H/r_0=37.2, is kept fixed and the jet exit velocity (i.e., Froude number) was increased from 9.44 to 18.20. As seen in Figure 5.6, the experimental results of the B series experiments are different than those of the deep case, with more spikes in the concentration profile which is due to the shallow water impact. In other words, when the jet Froude number increases and jet's front feels the water surface presence (in both intermediate and fully impingement scenarios), the concentration at the nozzle level will experience ups and downs due to jet pulses at the attachment level. However, the numerical results show a smooth decrease of

concentration as the distance from nozzle is increased with much smaller fluctuations. This could be due to the nature of RANS models and time-averaging of the results. It is expected that employing LES models may result in capturing the fluctuations in concentrations better at the nozzle level. It is understood that in the shallow water vertical discharges with fixed water depth the jet instabilities are increased with Froude number increase. Root mean square error (RMSE) of 0.02 and mean error (ME) of 0.00 were obtained for C/C_0 when numerical results were compared to experimental data. Table 5.2 in Section 5.4.5 provides a summary of error measures for quantitative comparison purposes.

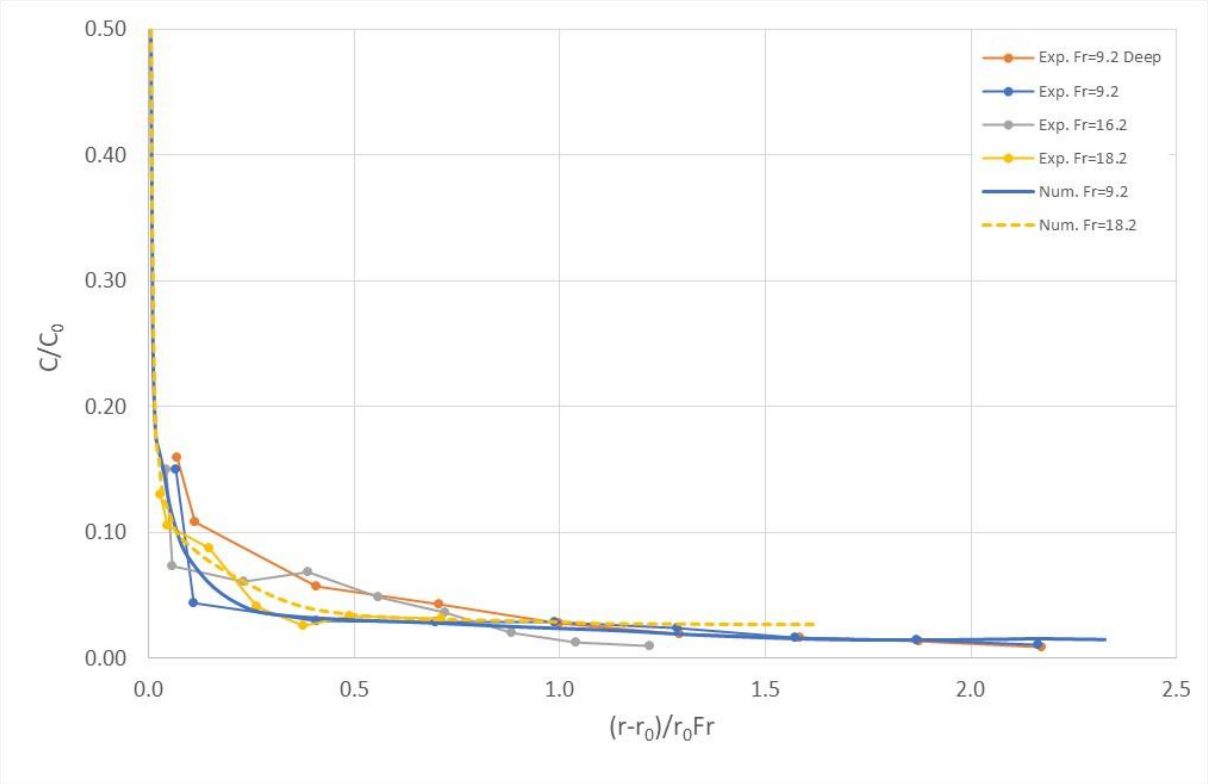

Figure 5.6: Concentration profiles at the nozzle level

Dilution rate is one of the key parameters in the design of outfalls in inland and coastal waters. An optimal design is the scenario that achieves the highest dilution rate. It is therefore important to understand the minimum dilution achieved at the return point (μ_{min}) in discharge of vertical dense jets. The minimum dilution at the return point increases with a reduction in water depth and when the flow regime changes from deep to intermediate (Figure 5.7). However, after impinging the discharge into the water surface, the return point dilution decreases. The numerical

results were able to capture same mechanism as that observed in the experimental tests. Even though the discharge impingement into water surface will result in jet expansion on the water surface (i.e., longer jet trajectory) and in a delay in the fallback of the jet to the return point, the dilution is reduced in the case of the impinging flow regime under steady-state condition. This suggests that surface attachment does not really contribute to the jet dilution as water entrainment is really limited (i.e., not much of water entrainment from bottom and top). It is also clear that an optimal design of vertical discharges in shallow water will be within the intermediate flow regime. Therefore, given the shallow bathymetry of a discharge location, the exit discharge should be designed such that the system reaches an intermediate flow regime. In the impinging regime, dilution decreases rapidly, which is a design point of concern. Fully impinging regimes can be recognized by monitoring the water surface disturbance visually and instrumentally. It is therefore advised to reduce the discharge flow rate (or velocity), when the surface disturbances are observed/monitored. RMSE of 0.01 and ME of 0.01 were obtained for μ_{min}/Fr when numerical results were compared to experimental data. Table 5.2 in Section 5.4.5 provides a summary of error measures for quantitative comparison purposes.

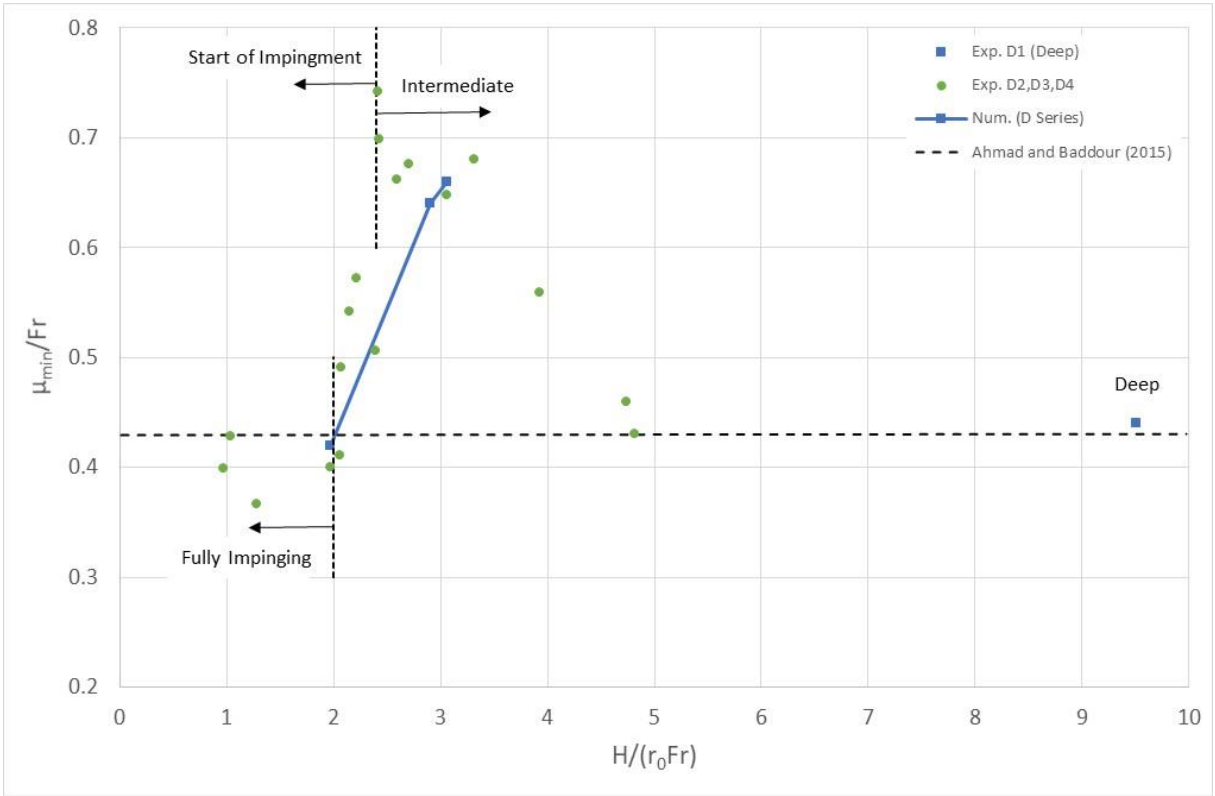

Figure 5.7: Minimum dilution at the return point of vertical dense discharges in shallow waters

5.4.3 Discharge Maximum Rise

To quantify and better understand the impact of the water depth on the discharge maximum rise, Z_m was nondimensionalized by the length scale r_0Fr (Eqn. 5.9) and was plotted against the nondimensionalized water depth (H/r_0Fr) in Figure 5.8. As shown in this plot, the Z_m/r_0Fr reaches an almost constant level for deep water conditions. Note that both numerical and experimental cases are for the C series experiments in which the Froude number was kept similar and only the water depth was changed to truly investigate the impact of the water depth on the discharge height. As the water depth decreases, the discharge height increases until the jet front starts impinging the water surface. As expected, beyond this point, the discharge height will descend with the water depth reduction. In the intermediate flow regime, the smaller water depth over the discharge generated a smaller pressure on the jet front and caused the jet to expand in height and laterally. When the water depth increased and was sufficiently high (i.e., $H/r_0>1.5Z_m/r_0$ based on Ahmad and Suzuki, 2016), the influence of the water column pressure on the discharge remains constant and the increase in water column pressure on the discharge becomes negligible. RMSE of 0.02 and ME of 0.01 were obtained for Z_m/r_0Fr when numerical results were compared to experimental data. Table 2 in Section 4.5 provides a summary of error measures for quantitative comparison purposes.

To analyze the impact of constant water depth and variable Froude number, results from B, E and F series experiments are shown in Figure 5.9 (Z_m/r_0 versus Fr). As expected, the discharge height increases with an increase in the Froude number until the jet's attachment to the water surface, where the discharge height reaches an asymptotic limit by further increasing the Froude number. Numerical results from this study are in good agreement with the experimental results of Ahmad and Suzuki (2016) for H/r_0=37.2. Among three cases modelled in the E series, the one with the lowest Fr is closest to the results of Baddour and Zhang (2009) which represents the deep flow regime. RMSE of 2.94 and ME of -2.00 were obtained for Z_m/r_0 when numerical results were compared to experimental data. Table 5.2 in Section 5.4.5 provides a summary of error measures for quantitative comparison purposes.

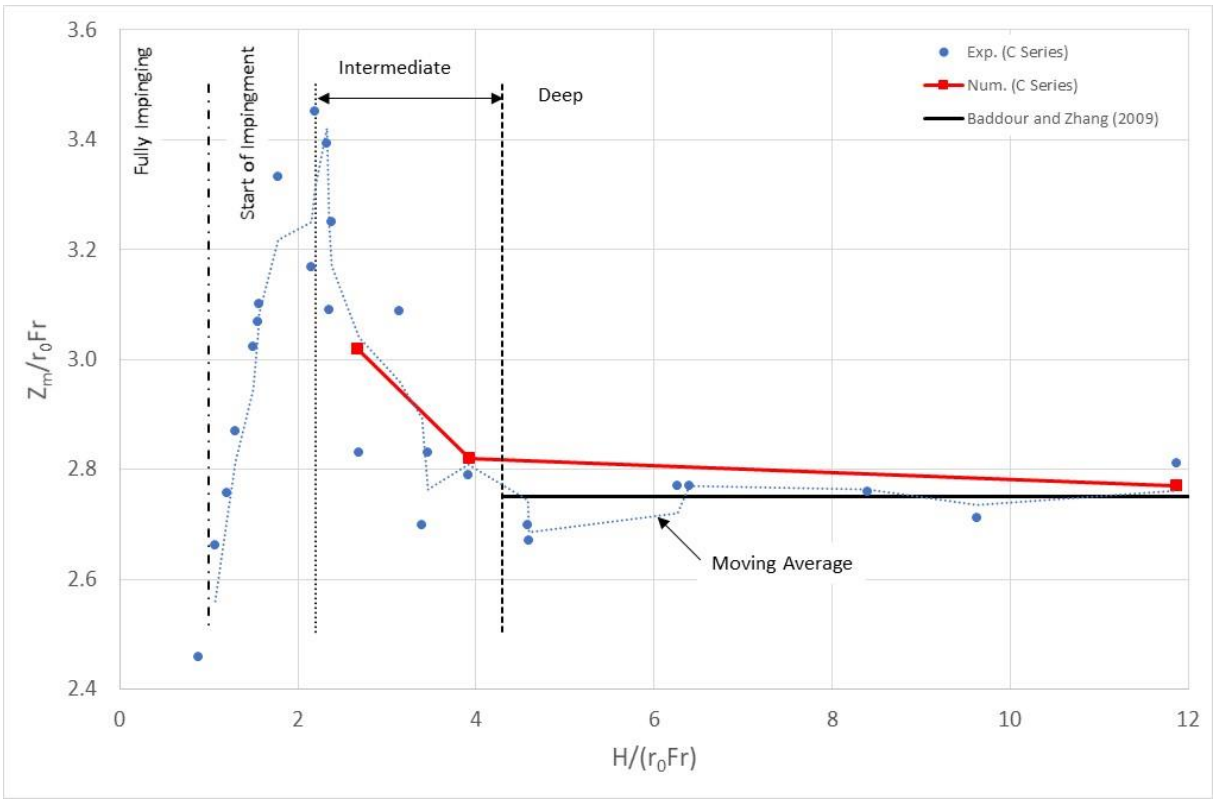

Figure 5.8: Discharge maximum rise under fixed Froude number and variable ambient water depths

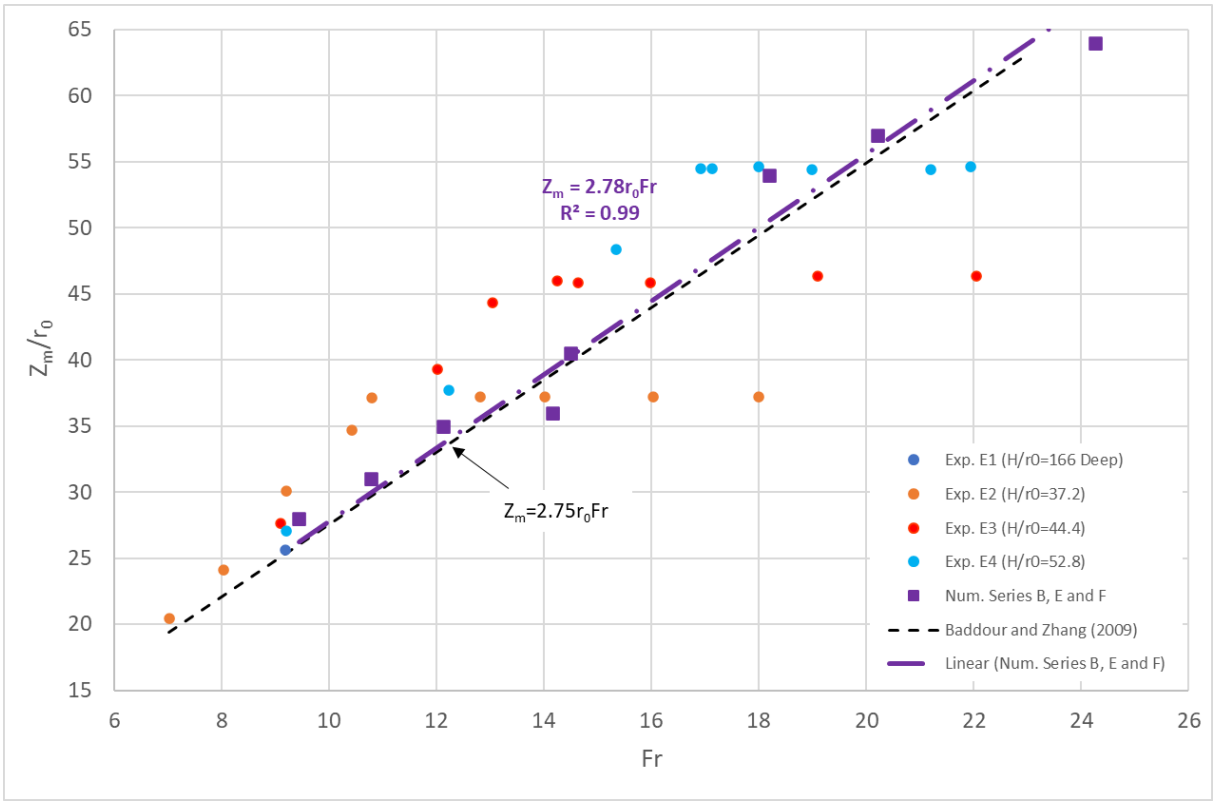

Figure 5.9: Discharge maximum rise under fixed ambient water depths and variable Froude number

5.4.4 Spreading Radius

There have been several studies on the lateral spread of impacting jets along a rigid and free surface (Holstein and Lemckert, 2001; Lemckert 2004; Cooper & Hunt 2007).

Cooper and Hunt (2007) focused on fluid mechanics and air dynamics applications such as air curtains, gas metal welding and aircraft vertical takeoff. They defined R_{sp} as a radial distance of the spread where lateral flow separates the rigid plate.

Holstein and Lemckert (2001) and Lemckert (2004) experimented saline jets impinging into rigid and free surfaces, respectively. Both of these studies were mostly intended to find a relationship between R_{sp}, discharge Fr number and water depth H. Holstein and Lemckert (2001) concluded that the total length travelled by the buoyant fluid prior to its separation from the plate (R_{sp}+H) is related to the discharge characteristics. Lemckert (2004) discussed that the jet in shallow ambient water travels a distance of (R_{sp}+H) in the same way as Z_m does in deep water with no surface attachment.

The surface attachment and size of the plume appearing on the surface are of particular regulatory concerns. Therefore, it is very important to understand the spreading radius of vertical dense jets impinging into the water surface. Figure 5.10 shows the numerical results of B, E and F series experiments compared to the experimental data of Ahmad and Suzuki (2016) and the powerline of Lemckert (2004). The numerical results are in good agreement with both past studies specially with the results from Lemckert (2004). The powerline from the numerical results suggest the following equation for the discharge spread at the surface in the impinging regime, which is very close to that of Lemckert (2004). It is noted that Froude numbers of the numerical study does not extend as large as those from Lemckert (2004).

$$\frac{H+R_{sp}}{r_0} = 5.04Fr^{0.73} \tag{5.22}$$

RMSE of 2.38 and ME of -0.03 were obtained for ($H+R_{sp}$)/r_0 when numerical results were compared to experimental data. Table 5.2 in Section 5.4.5 provides a summary of error measures for quantitative comparison purposes.

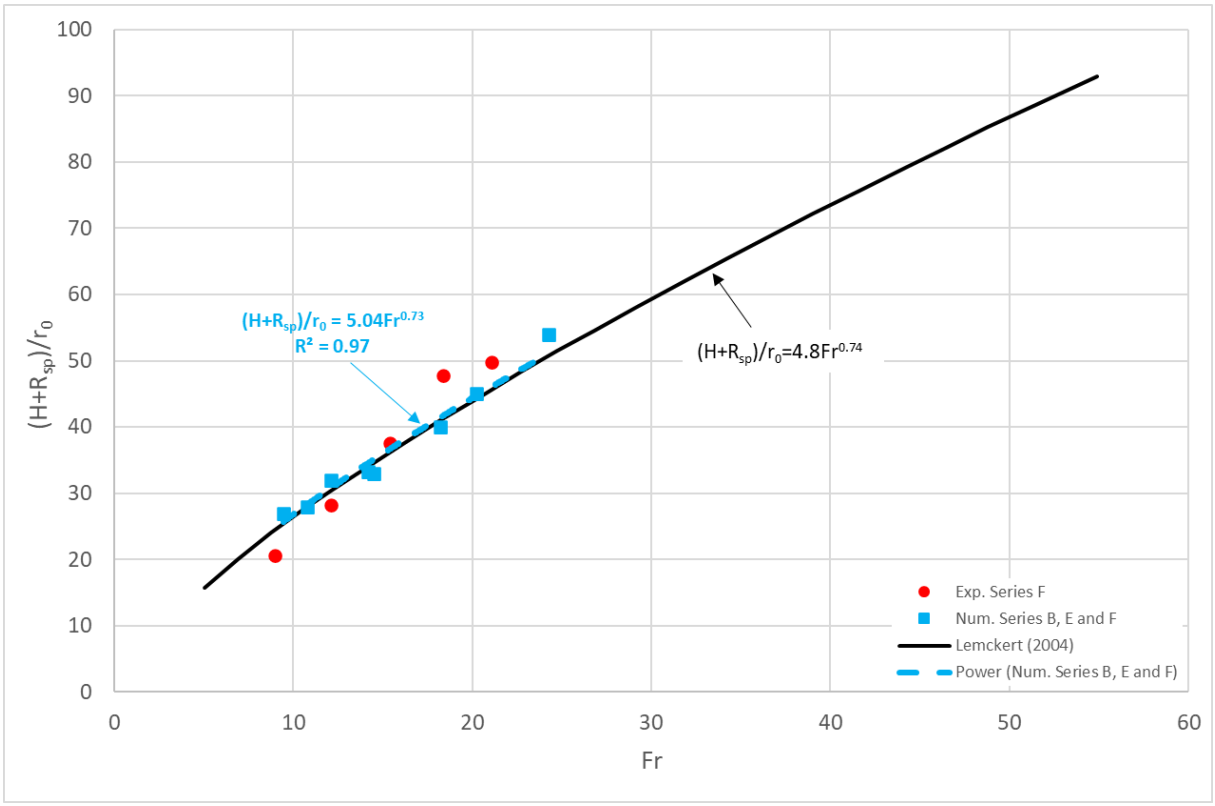

Figure 5.10: Lateral spread of the vertical dense discharges at the surface in the impinging flow regime

5.4.5 Quantitative Comparison

Previous sections presented the comparisons between the numerical and experimental data qualitatively in the graphs. Table 5.4 summarizes the root mean square error (RMSE) and mean error (ME) calculated for the parameters discussed earlier. As shown in Table 5.4 and Figure 5.11, the performance of the numerical model is promising for such applications (i.e., the vertical dense jet discharges in shallow water).

Table 5.4: Root mean square error (RMSE) and mean error (ME) for different parameters

Parameter/Error	C/C_0	Z_m/r_0Fr	Z_m/r_0	μ_{min}/Fr	$(H+R_{sp})/r_0$
RMSE	0.02	0.02	2.94	0.01	2.38
ME	0.00	0.01	-2.00	0.01	-0.03

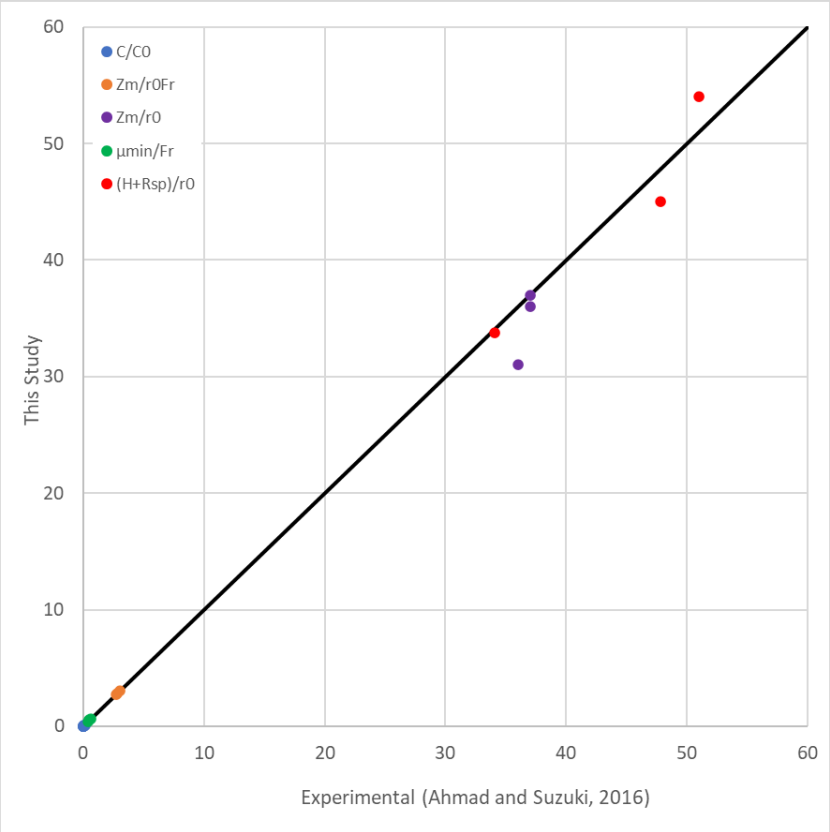

Figure 5.11: Numerical results (this study) against experimental data (Ahmad and Suzuki, 2016) for different parameters

5.5 Conclusions and Recommendations

In this study, for the first time, a comprehensive numerical modelling study is performed to investigate the vertical effluent discharges into shallow waters. The LRR turbulence model (known as Reynolds stress models - six equations to model anisotropic behavior) was used in this study based on previous studies (e.g., Gildeh et al., 2021). The following conclusions are drawn based on the results of this study:

- The vertical discharge under an intermediate regime results in higher discharge maximum rise compared to that observed in a deep regime. This is due to the smaller pressure of the water column above the discharge in the intermediate regime. Another contributing factor may be the stress conditions between two boundaries (i.e., discharge front boundary and water surface boundary) and viscous forces between two fluids with different densities.

- The minimum dilution at the return point is higher for the vertical jet in an intermediate regime when compared to the deep flow regime. Minimum dilution at the return point significantly reduces in the fully impinging regime. The surface attachment will make the overall trajectory of the jet longer, but the mixing reduces in the area of surface attachment due to the reduced water entrainment (e.g., from atmosphere).

The authors also recommend that:

- A control system (such as flange valves) for effluent discharge in the areas with shallow water or a large tidal range is recommended to reduce discharge, if the flow regime changes from intermediate to impinging. More detailed experimental and numerical studies will be needed to quantify the flow regime changes.
- For the next research steps, parameters such as ambient water stratification, current and wave will be added to the existing model to account for the environmental forcing. Turbulence and vorticity of the jet, especially in the attachment zone, will also be studied in more depth using LES turbulence models.
- Effect of nozzle geometry on the discharge maximum rise Z_m, will be investigated for optimizing the design to meet the depth criteria.

Notation

Following symbols are used in this study:

B_0 = buoyancy flux [m^4/s^3]
C = concentration at each cell [ppm/ppt]
C_0 = discharge concentration [ppm/ppt]
C_a = ambient concentration [ppm/ppt]
C_1 = return point concentration [ppm/ppt]
Fr = densimetric Froude number [-]
g = gravitational acceleration [m/s^2]
g_0' = reduced gravitational acceleration [m/s^2]
g_s' = effective gravity scale [m/s^2]
H = water depth above nozzle level [m]
k = turbulent kinetic energy [m^2/s^2]
L_s = length scale to normalize jet height [m]
M_0 = momentum flux [m^4/s^2]
Pr_t = turbulent Prandtl number [-]
Q_0 = discharge volume flux [m^3/s]
q_j = turbulent scalar flux [-]

r = radial distance [m]
r_0 = nozzle radius [m]
R_{sp} = jet lateral spread [m]
u = fluid velocity [m/s]
U_0 = discharge initial velocity [m/s]
Z_m = discharge maximum rise [m]
Γ = scalar diffusivity [kg/ms]
Γ_t = turbulent dispersity
δ_{ij} = Kronecker delta [-]
μ = fluid viscosity [Ns/m^2]
μ_{min} = minimum return point dilution [-]
μ_t = turbulent eddy viscosity [m^2/s]
ρ = fluid density at each cell [kg/m^3]
ρ_0 = discharge density [kg/m^3]
ρ_a = ambient density [kg/m^3]
τ_{ij} = Reynolds stresses [-]

References

1. Ahmad, N. & Baddour, R. E. 2012. Dilution and penetration of vertical negatively buoyant thermal jets. Journal of Hydraulic Engineering 138(10), 850–857.
2. Ahmad, N., Baddour, R.E. 2014. Minimum return dilution method to regulate the discharge of brine from desalination plants. Canadian Journal of Civil Engineering 41, 389–395.
3. Ahmad, N., Suzuki, T. 2016. Study of dilution, height, and lateral spread of vertical dense jets in marine shallow water. Water Science & Technology, doi: 10.2166/wst.2016.121.
4. Baddour, R.E., Zhang, H. 2009. Density effect on round turbulent hypersaline fountains. Journal of Hydraulic Engineering 135(1), 57–59.
5. Baum, M.J., Gibbes, B. 2019. Field-scale numerical modeling of dense multiport diffuser outfall in crossflow. Journal of Hydraulic Engineering. 146(1): 05019006.
6. Bleninger, T., Niepelt, A., Jirka, G.H. 2009. Desalination plant discharge calculator. Paper BD 180 for EDS Congress, Baden, Germany.
7. Cooper, P., Hunt, G. R. 2007. Impinging axisymmetric turbulent fountains. Physics of Fluids 19(11), 117101–117109.
8. Elhaggag, M.E., Elgamal, M., Farouk, M.I. 2011. Experimental and Numerical Investigation of Desalination Plant Outfalls in Limited Disposal Areas. J. Environ. Prot. 2, 828–839.
9. Gildeh, H.K., Mohammadian, A., Nistor, I., Qiblawey, H. 2014. Numerical Modeling of Turbulent Buoyant Wall Jets in Stationary Ambient Water. Journal of Hydraulic Engineering, 140(6), 04014012. https://doi.org/10.1061/(ASCE)HY.1943-7900.0000871.
10. Gildeh, H.K., Mohammadian, A., Nistor, I., Qiblawey, H. 2015. Numerical modeling of 30° and 45° inclined dense turbulent jets in stationary ambient. Environmental Fluid Mechanics, 15(3), 537–562. https://doi.org/10.1007/s10652-014-9372-1.
11. Gildeh, H.K., Mohammadian, A., Nistor, I., Qiblawey, H., Yan, X. 2016. CFD modeling and analysis of the behavior of 30° and 45° inclined dense jets – new numerical insights. Journal of Applied Water Engineering and Research, 4(2), 112–127. https://doi.org/10.1080/23249676.2015.1090351.

12. Gildeh, H.K., Mohammadian, A., and Nistor, I. 2021. Inclined Dense Effluent Discharge Modelling in Shallow Waters. Environ Fluid Mech 21, 955–987 (2021). https://doi.org/10.1007/s10652-021-09805-6.
13. Huai, W., Li, Z., Qian, Z. et al. 2010. Numerical simulation of horizontal buoyant wall jet. J Hydrody. 22(1):58-65.
14. Launder, B.E., Reece, G.J., W. Rodi. 1975. Progress in the Development of a Reynolds-Stress Turbulence Closure. Journal of Fluid Mechanics, 68:537–566.
15. Lemckert, C. J. 2004. Spreading radius of fountains after impinging a free surface. In: 15th Australian Fluid Mechanics Conference, December, Sydney University, Sydney, Australia.
16. Leschziner, M. 2016. Statistical turbulence modelling for fluid dynamics—demystified: An introductory text for graduate engineering students. London: Imperial College Press.
17. Mohammadian, A., Gildeh, H.K., and Nistor, I. 2020. CFD Modeling of Effluent Discharges: A Review of Past Numerical Studies", J. Water (MDPI), 12, 856.
18. OpenCFD Limited. (2017). OpenFOAM - User Guide, Version 4.1.0.
19. Pope, S. B. 2000. Turbulent flows. Cambridge, UK: Cambridge University Press.
20. Purnama, A., Al-Barwani, H.H., Al-Lawatia, M. 2003. Modeling dispersion of brine waste discharge from a coastal desalination plant. Desalination 155, 41–47.
21. Yan, X., Mohammadian, A. 2017. Numerical Modeling of Vertical Buoyant Jets Subjected to Lateral Confinement. J. Hydr. Eng. 04017016-1.
22. Yannopoulos, P., Noutsopoulos, G. 1990. The plane vertical turbulent buoyant jet. J Hydraulic Res. 28(5):565–580. doi: 10.1080/00221689009499046.
23. Zhang, H., Baddour, R.E. 1998. Maximum penetration of vertical round dense jets at small and large Froude numbers. Journal of Hydraulic Engineering 124(5), 550–553.

6 Concluding Remarks and Recommendations

6.1 Concluding Remarks

This study aimed to improve understanding of the mixing characteristics of effluent discharges in deep and shallow waters using CFD modelling. Due to previous work completed in this field, a comprehensive literature and critical review deemed necessary to identify the novel topics that have not been studied to details before. It was found that the discharge angles between 60° and 90° for deep waters were not studied before, numerically. For the shallow waters, there was no prior numerical modelling study, especially for the discharges that would impinge into the water surface. Below are the summaries of each section of the study.

Followings were found in the comprehensive literature review performed at the beginning of the study.

- Numerically, the most studied effluent discharge configuration has been in inclined dense jets, due to their applicability in industry. Most studies focused on lab-size experiments to calibrate their models. Details on jet trajectories and dilution and velocity characteristics have been investigated and compared to experimental data. RANS and LES turbulence models are popular for such studies.
- Vertical jets are also popular in CFD studies, and the new trend in studying these jets involves considering the ambient conditions that may affect these jets such as lateral confinement and water shallowness, where the jet is attached to the top boundary. Cross-flow in vertical jets could have a significant influence in terms of the trajectory and dilution, both of which are getting more attention from researchers using CFD models.
- Horizontal jets could be either positively buoyant or negatively buoyant with attachment to the bed (i.e., wall jets) or elevated (i.e., offset jets). Single jets have been studied experimentally and numerically during the past years, and more attention is now given to interactions of multiple horizontal jets when they merge after a certain distance from the discharge point.

Followings were found in the CFD study of the full submerged dense jet with inclination between 60° and 90°.

- Dimensionless initial and final terminal rise heights (Y_i/DF_0 and Y_f/DF_0) increase with discharge angle and become maximum for the 85° jets. This is in agreement with the most previous experimental studies except Papakonstantis et al. (2011a) which reported 80° discharge angle with the highest final terminal rise height;
- The ratio of Y_i/Y_f is about 1.05 for the four discharge angles simulated in this study, with the maximum of 1.10 for the 60° jets. This ratio seems to be independent of discharge angle;
- Dimensionless horizontal distance from the nozzle X_y/DF_0 at which the terminal rise height appears as well as the horizontal distance X_i/DF_0, where the outer jet boundary crosses the nozzle elevation, decreases as the discharge angle increases;
- Vertical distributions of dimensionless mean concentration at the location of the terminal rise height are asymmetric. It is approximately a Gaussian distribution and deviates from a Gaussian form in the falling limb due to the buoyancy induced instabilities in the jet farther from the discharge point; and
- The jet centreline dilutions at the terminal rise height and at the jet return elevation, normalized by the densimetric Froude number, suggest minimal changes for different discharge angles.

Followings were found in the CFD study of the shallow water with surface attachment of dense jet with inclination 30° and 45°.

- Axial velocities were extracted at different cross sections along the jet trajectory. They were then used to identify the jet centerline, as well as the different stages (i.e. initial, attachment, developed and two transitions between them for the PCR and CIR). For the PCR and CIR, the decay of the maximum axial velocity was affected by the surface attachment which results in farther propagation of the jet along the water surface.
- Minimum dilution at the surface and the return point were extracted in all numerical cases and were compared to those from the experimental work of Jiang et al. (2014). It was found

that, as the Froude number increased and the mixing regime changed from FSR to PCR and then CIR, the surface dilution (Ss) decreased until it reached an asymptotic limit, which is about *Ss/(H/D)* of 0.38 and 0.27 in the CIR for 30° and 45° discharges, respectively. The average differences between numerical results and experimental data of minimum surface dilution are +4% and -7% for the LRR and v2f turbulence models, respectively, for 45° discharges.

- The normalized *F/(H/D)* values for both 30° and 45° discharge angles in numerical cases (*F/(H/D)* value is the same for all turbulence models in each regime) are given in Table 4.3. The values are within the range proposed by Jiang et al. (2014) which confirms that the modelled jets fall within the correct classification for each *F/(H/D)*.
- Lower discharge angle (30°) reduces the probability of surface attachment for a given water depth when compared to the higher discharge angle (45°). However, if surface attachment occurs for both the 30° and 45° inclinations, the 45° discharges would be preferable since, for this case, the jet ensures a better return dilution. For instance, the average estimated return dilution *Sr* by LRR turbulence model in the PCR and CIR regimes for the 30° and 45° discharges are 18.75 and 25.05, respectively.
- The LRR RSM turbulence model was the most accurate among the five different turbulence models tested herein. The RSM models (and particularly the LRR model) reasonably captured secondary flows and buoyancy-induced forces since these models account for the effects of the stress anisotropy. Discrepancies between the numerical results and the experimental data exists, e.g. in the simulation of processes such as internal detrainment and therefore the velocity spread and dilution predictions. Moreover, the computational costs of the different turbulence models have to also be considered. RSMs are more computationally expensive than both two- and four-equation models (e.g. about 20 % more than realizable k-ε).
- The experimental data from Abessi and Roberts (2016) includes 60° inclined dense jets in shallow waters. Authors are currently performing analyses using the existing model for simulation of 60° inclined dense jets in shallow waters using the data from Abessi and Roberts (2016). The observations from Abessi and Roberts (2016) is close to that from Jiang et

al. (2014) and our numerical results are capable to reproduce those cases. Abessi and Roberts (2016) has suggested slightly different transition criteria.

Finally, followings were found in the CFD study of the shallow water with surface attachment of vertical dense jet.

- The vertical discharge under an intermediate regime results in higher discharge maximum rise compared to that in a deep regime. This is due to the smaller pressure forces of water column above the discharge in the intermediate regime. Another contributing factor may be the stress conditions between two boundaries (i.e., discharge front boundary and water surface boundary) and viscous forces between two fluids with different densities.
- The minimum dilution at the return point is higher for the vertical jet in an intermediate regime compared to the deep flow regime. Minimum dilution at the return point significantly reduces in the fully impinging regime. The surface attachment will make the overall trajectory of the jet longer, but the mixing reduces in the area of surface attachment due to the reduced water entrainment (e.g., from atmosphere).
- A control system (such as flange valves) for effluent discharge in the areas with shallow water or a large tidal range is recommended to be able to reduce discharge, if the flow regime changes from intermediate to impinging. More detailed experimental and numerical studies will be needed to quantify the flow regime changes.

6.2 Limitations of the Current Study

Following is a list of key limitations of the current study:

- The solver (twoLiquidMixingFoam) used in the dense effluent discharge modelling in shallow waters is a multiphase solver that uses the method of fluid volume for tracking the interaction of multiple fluid phases. Using a symmetry boundary condition on top surface is a reasonable and accepted method of estimating the atmosphere boundary for jet impingement, however, it does not capture the wave dynamics generated from the surface impingement. A volume of fluid (VOF) solver in OpenFOAM such as interFoam or interMixingFoam might be able to capture wave hydraulics on the surface better.

- Computational cost of the 3D models examined in this study is relatively high even using RANS turbulence models. It is specially expensive for surface impingement scenarios due to higher number of iterations needed in the model to reach a stable solution. For instance, each final simulation in Chapter 4 using a LRR turbulence model takes about 5 days (120 hours) on a Toshiba CORE-i7 with 8 processors. Therefore, the number of numerical experiments were selected carefully to reach a balance between the scope of work and computational resources.
- There is a shortage in experimental data available for dense effluent discharges in deep and shallow waters with more realistic ambient water conditions such as currents, density stratification, etc. The current study did not include the laboratory experiments of such conditions.
- Modification of turbulence models can improve their estimation of the mixing characteristics of dense effluent discharges. The current study used the turbulence models as defaulted in the OpenFOAM model as the main objective of Chapter 4 was to evaluate the performance of multiple turbulence models and identifying the best performing one.

6.3 Recommendations for Future Work

The following recommendations are proposed for numerical modeling of submerged jets in further studies:

- Structured refined mesh systems are used for the cases studied here. However, the OpenFOAM has the capability to apply FVM on the unstructured grids. The non-conformal mesh grid is also available in the model which can be studied in details later.
- A wide range of numerical models have been applied for the cases considered here. OpenFOAM, usually contains the latest version of the turbulence models. However, it is useful if one investigates new changes that might have happened lately in turbulence modelling and implement those changes to the available models.
- Buoyancy effect on the turbulence model was investigated by modifying the standard k-ε model using the SGDH and GGDH approaches for fully submerged discharges (Gildeh et

al., 2016). It is found that when the density-induced term is included in the turbulence model, the dense jet spreads more widely on the inner section, which is more realistic comparing to the experiment. It is recommended that the same modifications to be applied for shallow water discharges studied herein (both inclined and vertical). In-depth analysis is required to quantify the effect of coefficients in the buoyancy term and density difference between the jet and ambient water on the dense jet characteristics when utilizing SGDH and GGDH.

- Surface discharges have not been studied yet using a CFD approach, even though they are used in the industry and experimental data are available on such jets. This literature gap also exists for more complex jet configurations such as multiport and rosette diffusers.
- Previous studies have mainly focused on the stagnant ambient water due to the simplicity of internal and boundary conditions. However, to replicate real-life conditions more precisely, there is a need to move toward more complex ambient conditions to study the effects of wave, wind, co-flow and crossflow, density stratification, etc. on jet mixing and dispersion in CFD models.
- A wide range of turbulence models are available and have already been implemented in different CFD platforms that could be used for discharge mixing studies. Modifications of turbulence models, such as implementing the buoyancy terms, has been shown to be effective in improving the prediction of jet characteristics.
- Effect of nozzle geometry on the discharge maximum rise Z_m, could be investigated for optimizing the design of vertical dense discharges to meet the depth criteria.